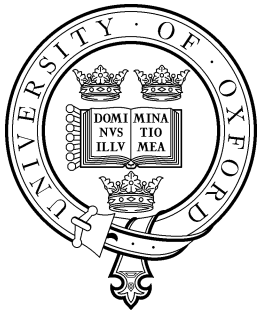
Knotted Polymers and Filaments



Richard James Matthews

Hertford College

University of Oxford

A thesis submitted for the degree of

Doctor of Philosophy

Trinity 2010

To my parents

Acknowledgements

I would like to thank my supervisors, Julia Yeomans and Ard Louis, firstly for accepting me as a student but more importantly for all the help and guidance they have offered me during my time in Oxford. I would also like to acknowledge all the members of their research groups.

I am grateful to all the people with whom I have had helpful and interesting discussions during the course of my work, particularly Olivier Pierre-Louis and Issam Ali.

I would like to thank the people who have made my time in Oxford enjoyable: firstly, Leisha for a wonderful past few months; all the members of the Oxford University Korfball Club, particularly Rosie for being a great captain; all the members of the Hertford-Merton MCR football team, particularly Tanmay for convincing me to join; everyone else I met and shared good experiences with here; my various housemates, especially Matthew, Elizabeth and Jeremy; all my officemates, particularly Iain and Tom; Andy, Joe and Olly for entertaining visits.

Abstract

Knotted Polymers and Filaments
Richard James Matthews, Hertford College
A thesis submitted for the degree of *Doctor of Philosophy*, Trinity 2010

The behaviour of knotted polymers and non-Brownian knotted filaments is investigated using bead-spring models, simulated using three different dynamical methods. We focus on knotted polymers under confinement, and on the dynamics of knotted polymers and filaments.

Langevin Dynamics is applied to study polymers confined in a slit. We find that, for relatively wide slits, knots decrease the force exerted by the polymer on the walls, whilst for narrower slits, they increase it. We interpret the results in terms of the effect of knots on the ability of polymers to spread out as the width is decreased.

We simulate knotted polymers migrating through a designed channel with sections of two different depths under an electric field. Trends in the mobility as a function of knot type depend on the depth of the narrower section. We discuss possible links to experimentally important knot electrophoresis.

We employ a Stochastic Rotation Dynamics algorithm to investigate knots diffusing in polymers under tension. We focus on two knot groups to demonstrate the effect of topology on effective friction coefficients and length relaxation. The latter is controlled by a breathing mode.

We use the Rotne-Prager tensor in simulations of knotted filaments under shear in the non-Brownian regime. We discover rich dynamical modes, which we classify into families. The modes show regular and chaotic motion with migration in the vorticity direction. We propose that, as filament deformability is varied, the onset of knot-tightening is determined by a dimensionless knot deformation number.

We study the effect of knotting on the ejection of flexible and semi-flexible polymers from a spherical, virus-like capsid. The polymer ejection rate is primarily controlled by the knot, which moves to the hole in the capsid and then acts as a ratchet. More complex knots lead to slower ejection.

Finally, we show preliminary results that indicate an interesting interplay between persistence length and tension in determining the location of a knot in a polymer of non-uniform flexibility. For lower tensions, the knot may be more likely to be found in a stiffer part of the polymer.

Publications

Some of the work of Chapters 4, 6, 7 and 8 is contained in the following publications.

1. R. Matthews, A.A. Louis and J.M. Yeomans. Confinement of knotted polymers in a slit. *Submitted for publication in Molecular Physics.*
2. R. Matthews, A.A. Louis and J.M. Yeomans. Complex dynamics of knotted filaments in shear flow. *EPL,* **92**:34003, 2010.
3. R. Matthews, A.A. Louis and J.M. Yeomans. Effect of topology on dynamics of knots in polymers under tension. *EPL,* **89**:20001, 2010.
4. R. Matthews, A.A. Louis and J.M. Yeomans. Knot-Controlled Ejection of a Polymer from a Virus Capsid. *Physical Review Letters,* **102**:088101, 2009.

Work in Chapter 5 is in preparation for publication and work in Chapter 9 may be prepared for publication in the future.

Contents

1 Introduction **1**
- 1.1 Polymers and Filaments . . . 2
- 1.2 Knots . . . 4
- 1.3 Overview of Thesis . . . 6

2 Background – Knots **9**
- 2.1 General . . . 9
  - 2.1.1 Knot Diagrams and Reidemeister Moves . . . 9
  - 2.1.2 Knot Types . . . 10
  - 2.1.3 Knot Chirality . . . 12
  - 2.1.4 Knot Invariants . . . 13
  - 2.1.5 Ideal Knots . . . 16
- 2.2 Knots in Biology . . . 17
  - 2.2.1 Action of Enzymes on DNA . . . 17
  - 2.2.2 Topoisomerases . . . 17
  - 2.2.3 Steady-State Level of Knotting . . . 18
  - 2.2.4 Knotted Proteins . . . 19
  - 2.2.5 Electrophoretic Separation of Knotted DNA . . . 19
- 2.3 Properties of Knotted Filaments . . . 20
- 2.4 Properties of Knotted Polymers . . . 21
  - 2.4.1 Probability of Knotting . . . 21
  - 2.4.2 Relaxation of Knotted Polymers . . . 22
  - 2.4.3 The Size of a Knot in a Polymer . . . 22

3 Models and Methods **24**
- 3.1 Polymer Models . . . 24
  - 3.1.1 Bead-Spring Models . . . 26
- 3.2 Dynamical Methods . . . 28
  - 3.2.1 Langevin Dynamics . . . 30
  - 3.2.2 Rotne-Prager Tensor . . . 31
  - 3.2.3 Stochastic Rotation Dynamics . . . 32
- 3.3 Summary . . . 38

4 Knotted Polymers under Compression **39**
4.1 Introduction . . . 39
4.1.1 Summary and Overview . . . 41
4.2 Asphericity of Knotted Polymers . . . 42
4.3 Model . . . 44
4.4 Results . . . 46
4.4.1 Comparison to a Scaling Prediction for Linear Polymers . . . 46
4.4.2 Knotted and Unknotted Ring Polymers Compared to Linear Polymers . . . 49
4.4.2.1 Monomer Density . . . 52
4.4.3 Summary and Discussion . . . 55

5 Knotted Polymers in Designed Channels **57**
5.1 Introduction . . . 57
5.1.1 Background . . . 57
5.1.2 Aims and Overview . . . 61
5.2 Model . . . 62
5.3 Results . . . 64
5.3.1 Mobility of Unknotted Polymers . . . 64
5.3.2 Mobility of Knotted Polymers . . . 66
5.3.3 Attempt Frequency and Transition Probability . . . 69
5.3.4 Free Energy Barrier . . . 73
5.4 Summary and Discussion . . . 75

6 Knotted Polymers under Tension **77**
6.1 Introduction . . . 77
6.2 Model . . . 78
6.3 Results . . . 80
6.3.1 Diffusive Motion . . . 82
6.3.2 Knot Length Relaxation . . . 86
6.3.3 Summary . . . 91
6.4 Further Work . . . 91

7 Knotted Filaments in Shear **93**
7.1 Introduction . . . 93
7.1.1 Knot Deformation Number . . . 94
7.1.2 Summary and Overview . . . 95
7.2 Model . . . 95
7.3 Results . . . 97
7.3.1 Mode Families . . . 97
7.3.2 Identification of Mode Families . . . 98
7.3.3 Regular and Chaotic Motion . . . 100
7.3.4 Average Migration Velocities and Periods of Rotation . . . 102
7.3.5 Other Parameter Choices . . . 103
7.3.6 Summary of Main Results and Overview . . . 105

7.4 Attractors . . . 106
7.5 Extensions to Model . . . 108
7.6 Bead Rotation Model . . . 109
7.6.1 Finite Thickness . . . 109
7.6.2 Torsion . . . 111
7.6.3 Dynamical Method . . . 112
7.6.4 Linking Number . . . 112
7.7 Results for Bead Rotation Model: Linear Filaments . . . 113
7.7.1 In Shear Plane Motion . . . 115
7.7.2 Out of Shear Plane Motion . . . 116
7.7.3 Summary and Discussion . . . 118
7.8 Results for Bead Rotation Model: Knotted Ring Filaments . . . 119
7.9 Summary and Further Work . . . 120

8 Ejection of Knotted Polymers from a Capsid 123
8.1 Introduction . . . 123
8.2 Method . . . 126
8.3 Results . . . 128
8.3.1 Changing Knot Position . . . 129
8.3.2 Ejection Rates . . . 130
8.3.3 Multiple Knots . . . 132
8.4 Summary and Discussion . . . 133

9 Knots in Polymers of Non-Uniform Flexibility 135
9.1 Introduction . . . 135
9.2 Model and Methods . . . 137
9.3 Results . . . 140
9.3.1 Varying Tension . . . 140
9.3.2 Varying Flexibility . . . 142
9.3.3 Varying Section Length . . . 143
9.3.4 Summary . . . 143
9.3.5 Discussion . . . 144
9.4 Further Work . . . 147

10 Summary 149

Bibliography 152

A Background – Polymers and Filaments 163
A.1 Statics . . . 163
A.1.1 Polymer Size . . . 164
A.1.2 Polymer Shape . . . 165
A.1.3 Persistence Length . . . 167
A.1.4 Linking Number . . . 168
A.1.5 Blob Picture . . . 169

A.2 Dynamics 170
A.2.1 Rouse Model 171
A.2.2 Hydrodynamic Interactions 171
A.2.3 Zimm Model 174
A.2.4 Reptation 175

B Knot Methods **177**
B.1 Checking Knot Type 178
B.2 Diagram Simplification 179
B.3 Knot Locating 181
B.4 Creation of Knot Configurations 183

Chapter 1

Introduction

Knots, at least in a loosely-defined sense, are familiar from everyday life. They are important in activities as diverse as sailing and climbing. After a moment's thought, it is clear that a knot could be made in any string-like object and so it is perhaps not surprising that they turn out to play a role on much smaller scales too, particularly in polymers. Knotted polymers have proven to be a rich topic for investigation with fascinating connections to biology. Here we build on previous work, choosing to focus primarily on problems related to the confinement and dynamics of knotted polymers, as well as larger knotted objects. Our results uncover interesting effects such as the rich dynamics of knots in shear flow; suggest how knots could affect processes such as the ejection of DNA from a bacteriophage; and highlight new aspects of older problems such as knot diffusion.

The remaining three sections of this chapter introduce the knot-forming objects, introduce knots themselves in a little more detail, and summarise the problems we consider.

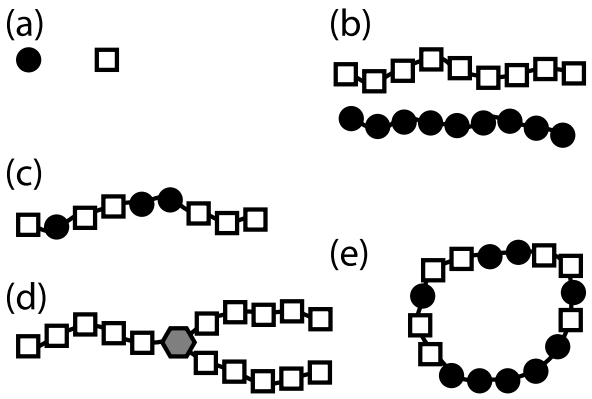


Figure 1.1: Polymers are formed in reactions that link monomers into chains. (a) Different monomers are represented by the two shapes. (b) Polymers may be formed of only one type of monomer. (c) They may also contain more than one. (d) Branched structures may arise through incorporation of additional chemical species [1]. (e) Chains may be closed to form rings. Note that the chains shown are much shorter than typical polymers.

1.1 Polymers and Filaments

As discussed, this thesis is about knots, which may be formed from extended string-like objects. Physical examples of these are polymers and filaments. Here we use the term 'polymer' to refer to the Brownian case, where thermal fluctuations are important, and 'filament' to refer to the non-Brownian case, where they can be ignored. It should be noted that, whilst this usage of the word polymer is standard, in the literature, filament may also refer to Brownian objects.

Chemically, polymers are formed through polymerisation reactions in which individual monomers are joined to form long chains [1]. In some polymers, all the monomeric units are identical but this is not always the case. Polymers may be branched or form closed rings. These different possibilities are shown in Fig. 1.1.

Most of the experiments relating to the work we describe here are concerned with DNA (deoxyribonucleic acid). DNA is made up of four monomers [2] that differ according to which of four bases – adenine (A), cytosine (C), guanine (G) or thymine (T) – they contain. It is usually found in a double-stranded form: bases from two

chains of monomers form hydrogen bonds with each other, binding the two polymers together, generally in a double-helical structure. It is energetically favourable for A to bind to T, and G to C, so the two strands typically have complementary bases. The biological function of DNA is to carry genetic information, which is encoded by the base sequence.

Double-stranded DNA is a semi-flexible polymer and in physiological conditions typically has a persistence length of about $50nm$ [3] and a diameter of about $2nm$. As discussed in ref. [3], DNA persistence length does depend on ionic conditions in the solution. It may also be affected by the specific base sequence (see section 9.1).

When DNA is closed into a ring it has a conserved linking number [4], see Appendix A.1.4. In some experiments, for example electrophoresis [5], a break in one of the strands may be introduced so this is no longer the case. If un-nicked DNA is closed such that it is under torsional tension, so that the number of base-pairs per turn of the double-helix is different to its preferred value, it may adopt compact, super-coiled configurations to relax [2]. In super-coiling the double-helix is wrapped around itself: the DNA exchanges twist for writhe. Super-coiling may be positive, if the the number of base-pairs per turn is less than the preferred value, or negative.

Examples of physical experiments using DNA include: measurements of force-extension curves [6]; investigation of the dynamics of single polymers in shear flow [7]; translocation through a nanopore [8]; measurement of diffusion coefficients [9]; and electrophoretic separation by length in an array of obstacles [10].

While DNA has been extensively studied, experiments on non-Brownian filaments are rather more limited; they generally use manufactured objects. We give a few examples. In refs. [11] and [12] the dynamics of long, flexible filaments – with typical diameters $\sim \mu m$ and lengths $\sim mm$ – in shear in a viscous fluid were considered. Different dynamical regimes were identified, including rotations in the shear plane and coiled motion extending out of it. In ref. [13], the transport of similar filaments

through a rough channel was investigated. Filaments were found to show large deformations and entanglement during events where they became pinned at the walls. In ref. [14], filaments were created by joining paramagnetic particles and the shapes they formed under rotating fields were studied. Ref. [15] looks at the sedimentation of dilute suspensions of rigid filaments, finding that they clump together to form packets that settle faster than individual filaments.

Some general background information about polymers and filaments is given in Appendix A.

1.2 Knots

Early work on knots in the 19^{th} century was motivated by the suggestion that atoms are vortex rings [16]. These rings were supposed to exist in a perfect liquid (with zero viscosity) and derive their different characters from their topology, so that knowledge of the different types of knots was of crucial importance. The task of deducing different knot types was first undertaken by P.G. Tait, who compiled tables listing all possibilities up to a given complexity [17].

Although the vortex picture of atoms has long since been rejected, knots have again become relevant to physics: on the one hand connections to quantum field theory have been realised [18] but also, more relevantly to this thesis, the occurrence of knots in polymers [19] has stimulated efforts to understand their physical effects.

Whilst knots are general and any polymer of sufficient length in solution is very likely to be knotted [20], they have proven to have particular relevance in biological systems. The DNA contained in the cells of living organisms is typically very long and confined: the genome of *E. coli*, a well studied bacterium [2], is about 3×10^4 persistence lengths [2] ($\sim 1.5mm$) and is contained in a cell with a typical volume $\sim \mu m^3$ [21]. Although the DNA is organised using supercoiling and proteins [22],

confinement makes entanglements likely [23], particularly during processes such as replication [24].

There is a family of enzymes, topoisomerases [25], one of whose functions is to control knotting. Knots in DNA can prevent transcription [26], a process necessary for the production of proteins, and topoisomerases have been found to be crucial for life [25]. Beyond topoisomerases, analysis of knotting may be used to understand how other enzymes function [27]. Evidence of knotting of DNA has also been found in bacteriophages [28], viruses that infect bacteria. Biological experiments on knotting rely on the identification of the different types of knots in DNA molecules. One widely used method for achieving this is gel electrophoresis [5].

Given the ubiquity of knots and their relevance to biology, it is important to understand their properties and their effect on the properties of polymers. Some previous work has focussed on general issues such as how knots affect the relaxation of polymers [29]; the probability that knots are formed in polymers [30]; whether knots in polymers are localised [31]; and the diffusion of knots in polymers under tension [32]. Other work has been motivated more directly by biology. For example, there have been attempts to understand how topoisomerases maintain a 'low' level of knotting [33]. More detailed information about previous work on knots is given in Chapter 2.

In comparison to linear polymers, previous work on knotted polymers under confinement, and on their dynamics, is limited. Confined polymers are common in biology, as discussed above, and an understanding of dynamics is clearly necessary for a full picture of knotting. These two areas require more investigation and are the main focusses of this thesis.

1.3 Overview of Thesis

We summarise the main results of the thesis. After Chapters 2 and 3, which give background and introductory information on knots and simulation techniques respectively, each chapter considers a different problem, although there are links between them. We briefly describe each in turn, indicating how they relate to our main themes of confinement and dynamics.

Chapter 4 looks at knotted polymers confined in a slit, a problem clearly linked strongly with our first theme. We find that, in relatively wide slits, knots decrease the force exerted on the walls, whilst for narrower slits, they increase it. The reasons for these findings are investigated.

Chapter 5 presents results for simulations of knotted polymers migrating through a designed channel with sections of two different widths under an electric field. As found in Chapter 4, the way in which mobility changes with knot complexity is different depending on the width. Generally, bigger differences in mobility are seen for lower fields, although they must be sufficiently high that all knots migrate. The trends seen show qualitative similarities to experimental gel-electrophoresis results, which are discussed. We find evidence that the changes in mobility are due to the effect of the knot on the transition probability for a polymer to move into a narrower section. The transition probability is determined by an entropic barrier which arises due to the confinement of the polymers in the narrower section, relating to our first theme. The results suggest that such channels may be used as a method for the separation of DNA according to knot type.

Chapter 6 builds on previous simulation work relating to an experiment on the diffusion of knots in DNA held under tension, a problem that falls under our second topic of dynamics. We employ a new method for putting polymers under tension and focus on how topology affects the behaviour by considering two knot groups. Evidence to support a reptation picture is found. We find effective friction coefficients

that show a clear difference between the groups. This may be explained in terms of topological features. The relaxation of the knots is investigated and we compare the dependence of the time-scales on knot complexity to previous work on polymers without tension. We identify modes of knot deformation, one of which determines the relaxation. Again, differences between the groups are rationalised in terms of topological features.

Chapter 7 investigates knotted filaments in simple shear, a problem that comes under our second theme of dynamics, proposing them as an interesting new example of deformable objects for study in such flows. Initially, simulations using a relatively simple model are performed. We find rich behaviour, with the filaments of a particular flexibility displaying various different modes of motion. The modes show migration in the vorticity direction. We propose a dimensionless parameter to determine when the knot will be tightened by the flow as the filament is made more deformable. In later sections, issues with the model are discussed and a more sophisticated approach is introduced. Results for the new model are found to be qualitatively similar. We also simulate linear filaments, finding reasonable qualitative agreement with experiment.

Chapter 8 asks how knots in the DNA in a bacteriophage capsid might affect its ejection. Motivated by experiments that found high probabilities of knotting for DNA confined within virus capsids, we consider ejection of flexible and semi-flexible knotted polymers from a spherical, virus-like capsid. The dynamics are driven by the confinement, connecting the work to both of our main themes. The polymer ejection rate is found to be primarily controlled by the knot, which moves to the hole in the capsid and then acts as a ratchet. Polymers with more complex knots eject more slowly and, for large knots, the knot type, and not the flexibility of the polymer, determines the rate of ejection.

Chapter 9 addresses the question of how changing the flexibility of different sections of a polymer, as well as the tension it is subjected to, affects the location of

a knot. The work is prompted by the propensity of topoisomerase II, an enzyme associated with knotting, to act near flexible regions of DNA. It does not, however, aim to model this particular system, but rather attempts to look for generic effects. We find results that indicate that, depending on persistence lengths and tension, a knot may be found with higher probability in either a more flexible or a stiffer region. We propose that the results may be explained using a blob-type picture and that the behaviour is determined by the relative sizes of three key length-scales.

Finally, Chapter 10 summarises the results of the previous six chapters.

Chapter 2

Background – Knots

In this chapter, we bring together various background information about knots. This is to introduce concepts that are used in later chapters and to highlight interesting previous work. In section 2.1, we discuss concepts, largely mathematical, that apply to knots generally, without reference to what is knotted. In section 2.2, we consider knotting in biology. In section 2.3, we look at the properties of knots in filaments. Finally, in section 2.4, we look at their properties in polymers.

Sections 2.1.1 to 2.1.4 are largely based on material from books by Livingston [34] and Kauffman [35].

2.1 General

2.1.1 Knot Diagrams and Reidemeister Moves

A *knot* is a closed curve in three-dimensional space that does not intersect itself. If one knot may be transformed into another, using only smooth deformations, then the two are equivalent and have the same *knot type*. In this thesis we will often simply use 'knot' for 'knot type'. This definition includes curves that may be deformed into a simple loop, often called the *unknot*. Links are unions of disjoint knots which may

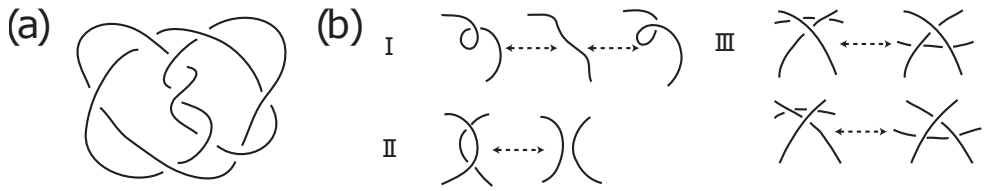


Figure 2.1: (a) An example of a knot diagram, (b) The three Reidemeister moves: type I, type II and type III.

be entangled with each other.

A *knot diagram* is a projection of a knot onto a plane, such that no three points on the curve project to the same place. In general, there are a number of pairs of points that project to the same place; these correspond to crossings. An example of a knot diagram is shown in Fig 2.1(a). For a given knot type, there is a minimum number of crossings – the *essential crossings* or *crossing number* – possible for any diagram. Projections with this number of crossings are minimal. We also use the informal term *knot complexity*: more complex knots have higher crossing number. For calculations with knot diagrams, it is often necessary to assign an orientation by choosing one of the two directions in which the curve may be traversed. When this is done, the diagram is *directed*.

It may be proven that, if two knots are equivalent, then the knot diagram of one may be transformed into the diagram of the other by a series of *Reidemeister moves*. These are local changes to the diagram that only modify one part. The three different types of Reidemeister moves are depicted in Fig 2.1(b).

2.1.2 Knot Types

A general knot may be decomposed into different sections by considering spheres that intersect the curve at only two points. These sections may be closed – with additional sections that do not pass inside/outside the sphere respectively – to form new knots. If there is no decomposition of a curve, or any topologically equivalent curve, such

that both parts are non-trivial knots, that is to say they are not simple loops, then the original knot is *prime*.

A notation for different prime knot types was introduced by Alexander and Briggs [36]. A knot is denoted C_k, where C is the crossing number and k distinguishes different knots with the same value of C. In ref. [36], all knots with up to and including 9 essential crossings were tabulated. Using the same notation, Rolfsen [37] extended this up to 10 essential crossings. We use the notation for a few knots with over 10 essential crossings, by continuing patterns up to 11 and 12: specifically, we use 11_1 and 12_1 to denote knots of 11 and 12 essential crossings with similar topology to the other C_1 knots. The notation does not distinguish between enantiomers. Non-prime knots are often denoted $K_1\#K_2\#...\#K_n$, where K_p are the notations for their prime components. The unknot is denoted 0_1. In 1998, Hoste, Thistlethwaite and Weeks published a paper [38] describing the tabulation of all prime knots with up to 16 essential crossings, over 1.7×10^6 knots, vastly extending the work of ref. [37] (though not employing its notation).

Some knots may be assigned to families. One example is the torus knots, which may be drawn to lie on the surface of a torus with a line that does not cross itself. Torus knots may be denoted by (p, q), where p is the number of times that the contour passes through the hole of the torus and q is the number of rotations round it. For torus knots, p and q are coprime. The knots with Alexander-Briggs notation C_1, with C odd, are torus knots of the form (C,2). $(4, 3)$, the first torus knot not of this form, has Alexander-Briggs notation 8_{19}.

Knots with the Alexander-Briggs notation C_1, with C even, are known as even-twist knots. In much of this thesis, particularly Chapters 5, 6 and 8, we focus on torus knots of the type C_1 (C odd) and even-twist knots. These knots are commonly found in biological systems, see, for example, refs. [39], [28] and [24].

2.1.3 Knot Chirality

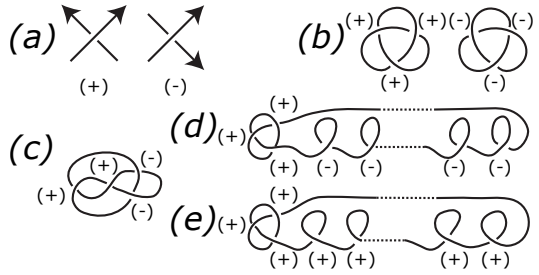


Figure 2.2: (a) All crossings in a projection of a certain knot configuration are either right-handed, (+), or left-handed, (−). (b) A minimal projection of a right-handed trefoil, $3_1(+)$, has three (+) essential crossings and its mirror image, $3_1(-)$, has three (−) essential crossings. (c) 4_1 has two (+) and two (−) and is achiral (d) A left-handed configuration for $3_1(+)$: if a configurational chirality measure is calculated for a given representation of a knot it can have either sign regardless of the topological chirality of the knot. The 'tail' part is twisted so that it is left-handed – if it is long enough, the chirality measure will indicate a left-handed configuration, although, topologically, the knot is right-handed. (e) The 'tail' part has right-handed twists.

If a knot is topologically chiral, then there is no way its mirror image may be deformed into the original without cutting. In a (directed) projection of a knot, crossings may be identified as either right- or left-handed, as shown in Fig. 2.2(a). The simplest knot, 3_1, is chiral. If minimal projections are chosen, the right-handed trefoil, $3_1(+)$, has three right-handed essential crossings and the left-handed trefoil, $3_1(-)$, has three left-handed. 4_1, which is achiral, has two right-handed and two left-handed. These knots are all illustrated in Fig. 2.2.

There also exist measures that may be used to assign a numerical value to a certain representation of a knot (or any other object) that will indicate a 'configurational' chirality. Roughly, these give an idea of how closely the mirror image of the configuration may be superposed on the original, *without* any deformation [40]. For example, Solymosi *et al.* [40] considered a chiral index for molecules that sums a quantity calculated from the inter-atomic vectors over all sets of four atoms. As shown in Fig. 2.2(d), the 'configurational' chirality of a particular representation of a

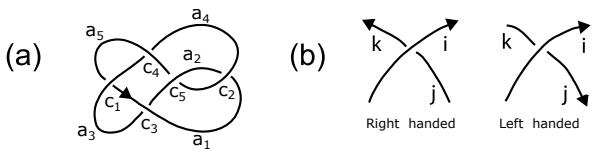


Figure 2.3: (a) An orientated diagram of the 5_2 knot, whose arcs and crossing have been labelled: a_n for arcs and c_n for crossings. When calculating the Alexander polynomial as described in the text, labelling of the arcs and crossings may be done independently of each other. (b) The arc labels needed for right handed and left handed crossings when constructing the matrix used to calculate the Alexander polynomial.

knot may take any value.

2.1.4 Knot Invariants

A central concern of mathematical knot theory is determining whether two knot diagrams in fact represent the same knot. *Knot invariants* – quantities that are invariant under deformations of the knot, or equivalently Reidemeister moves – can be helpful in approaching this problem. *Knot polynomials* are one type of invariant. The earliest of these, the *Alexander polynomial*, was proposed by Alexander [41].

The Alexander polynomial, $A_K(w)$, of a knot may be calculated by the following procedure: given an oriented diagram of the knot, the arcs are labelled using 1 to N, N being the number of crossings in the diagram. Then, the crossings are separately labelled. An example, using the 5_2 knot, is shown in Fig. 2.3(a).

The calculation starts with an $N \times N$ matrix, with all entries zero. For the l^{th} crossing, i, j and k are identified depending on handedness, as shown in Fig. 2.3(b). To row l, the following values are added: $1 - w$ to column i; -1 to column j; $-w$ to column k. For example, from the labelled diagram shown in Fig. 2.3(a), this matrix

is obtained:

$$\begin{pmatrix} -1 & 0 & 1-w & 0 & w \\ w & -1 & 0 & 1-w & 0 \\ 1-w & w & -1 & 0 & 0 \\ 0 & 0 & w & -1 & 1-w \\ 0 & 1-w & 0 & w & -1 \end{pmatrix}. \tag{2.1}$$

Removing the last row and the last column of the matrix, the determinant of what remains gives the Alexander polynomial of the knot. The example above gives:

$$\begin{vmatrix} -1 & 0 & 1-w & 0 \\ t & -1 & 0 & 1-w \\ 1-w & w & -1 & 0 \\ 0 & 0 & w & -1 \end{vmatrix} = 2w^3 - 3w^2 + 2w. \tag{2.2}$$

However, for different diagrams and labellings, the results will change by a factor of $\pm w^m$, where m is an integer. The Alexander polynomial is only defined up to factors of $\pm w^m$ but it has the property that it may be symmetrised such that $A_K(w) = A_K(w^{-1})$. For example, dividing the polynomial in Eq. (2.2) for 5_2 by w^2 gives $A_{5_2} = 2w - 3 + 2w^{-1}$.

Conway showed that the Alexander polynomial may be calculated using *skein relations* [34]. Specifically the relations,

$$\begin{aligned} &\text{(i) } \nabla_K(z) = \nabla_{K'}(z) \text{ if } K \text{ and } K' \text{ are equivalent} \\ &\text{(ii) } \nabla_{unknot} = 1 \\ &\text{(iii) } \nabla_{K_+} - \nabla_{K_-} = z\nabla_{K_0}, \end{aligned} \tag{2.3}$$

define the Conway polynomial, $\nabla(z)$, which is related to the normalised Alexander polynomial by $\nabla_K(w^{\frac{1}{2}} - w^{-\frac{1}{2}}) = A_K(w)$. The labels K_+, K_- and K_0 in Eq. (2.3)(iii),

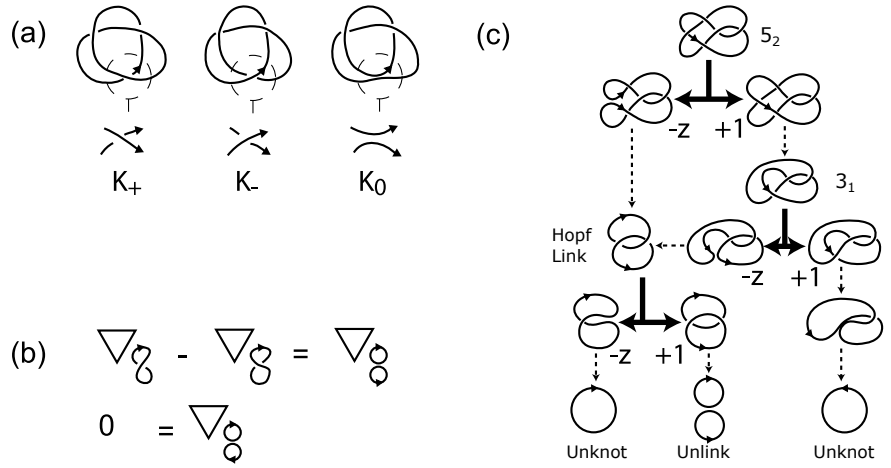


Figure 2.4: (a) Three knot diagrams which differ at only one crossing. The notation corresponds to that used in Eq. (2.3)(iii). (b) Using Eq. (2.3)(iii) and considering an unknotted ring that is twisted once it may be seen that the Conway polynomial of two unlinked rings is 0. (c) Decomposition of a knot diagram for 5_2 using Eq. (2.3)(iii) The solid arrows indicate alterations to the diagram at one crossing, producing two new diagrams according to Eq. (2.3)(iii). The dashed arrows indicate simplifications of the diagrams using Reidemeister moves. To calculate the Conway polynomial for 5_2 a sum of the branches must be made, multiplying each branch by the values indicated at the split.

the exchange relation, refer to knot diagrams which are identical except at one crossing: in the K_+ diagram the crossing is right-handed; for K_- it is left-handed; for K_0 the strands have been spliced to remove it. Three diagrams related in this way are shown in Fig. 2.4(a). Using Eq. (2.3)(iii), a knot diagram may be reduced to a series of unknots and unlinks, allowing the Conway polynomial to be determined. The polynomial for the unknot is defined to be 1. The polynomial for two unlinked unknots may be deduced to be 0, see Fig. 2.4(b).

An example of how skein relations may be used to calculate the Conway polynomial, for 5_2, is shown in Fig. 2.4(c). It may be seen that $\nabla_{5_2}(z) = -z(-z + 1(0)) + 1(-z(-z) + 1(1)) = 2z^2 + 1$. Substituting $z = w^{\frac{1}{2}} - w^{-\frac{1}{2}}$, gives the same normalised Alexander polynomial as calculated from Eq. (2.2).

There exist various other knot polynomials, which may also be defined using skein relations. For example, for the Jones polynomial, the exchange relation is

$w^{-1}V_{K_+} - wV_{K_-} = (w^{\frac{1}{2}} - w^{-\frac{1}{2}})V_{K_0}$. The HOMFLY polynomial, in two variables, which was proposed independently by multiple different authors, generalises the Conway and the Jones polynomials, its exchange relation is $\alpha P_{K_+} - \alpha^{-1} P_{K_-} = z P_{K_0}$.

The Jones polynomial and the HOMFLY are able in some, though not all, cases to distinguish enantiomers, something which the Coway polynomial can never do. It should be noted that none of the knot polynomials proposed so far can distinguish all knots. The mapping from knots to polynomials is many-to-one such that multiple, in fact infinite numbers of, knots share the same polynomial.

2.1.5 Ideal Knots

Consider forming a knot from a cylindrical tube of uniform radius that may not overlap itself. The *ideal* form is the configuration which maximises the diameter to length ratio of the tube, whilst keeping the correct topology [42].

In practice, ideal knots have been found by numerical minimisation [42]. Such approaches may find only local minima, and so the results do not necessarily represent the true solutions. The results do suggest that, for a given knot type, there is a unique solution.

The *average crossing number* of a particular knotted configuration is the number of crossings in a certain projection, averaged over all directions. This quantity is not generally a topological invariant. If calculated for an ideal knot, however, it does provide such an invariant, assuming unique ideal representations do exist. The average crossing numbers of ideal knots may be useful for distinguishing different knot types [42].

2.2 Knots in Biology

2.2.1 Action of Enzymes on DNA

The family of enzymes most often associated with knotting are *topoisomerases* [2]. There are, however, other enzymes, for example recombinases [2], that can form knots or links. Indeed, analysis of the knots they form can be a useful tool for understanding how they operate [43]. Crisona *et al.* [39] studied bacteriophage λ integrase, which plays a role in the integration of the viral DNA into that of its bacterial host. By inspecting the knots formed when the enzymes acted on DNA substrates they were able to use the mathematical concept of *tangles* to make deductions about the enzyme action. In ref. [27], tangles, and their application in the analysis of enzymes, are discussed.

2.2.2 Topoisomerases

Topoisomerases are a family of enzymes that catalyse shifts between topological isomers of DNA [25]. They are subdivided into two types, both of which introduce temporary breaks in DNA. Type I cleave only one strand whilst type II cleave both strands of the duplex. They are necessary in cells to resolve entanglements that occur during various processes, such as replication and transcription, and to maintain an optimal level of super-coiling [44]. The tasks done by topoisomerases are vital to the viability of all organisms, both eukaryotic and prokaryotic [25]. Topoisomerases have been identified as the target of many anticancer drugs, as well as some antibiotics [45].

Type I topoisomerases are further divided into two subfamilies: type IA and type IB. Type IA partially relax negative super-coiling and may also knot, unknot, catenate and decatenate single-stranded DNA or nicked double-stranded DNA. All these actions are achieved by passing a second strand through the temporarily open one. Type IB relax positive and negative super-coiling. It is thought that they achieve

this by cleaving one strand and then allowing the duplex to rotate to relax torsional stress before it is closed [44].

Type II topoisomerases are also divided into subfamilies but they all operate by the transport of one strand through another [44]. They may change the level of DNA super-coiling (not just relax it), knot and unknot single DNA molecules or catenate and decatenate multiple DNA molecules. The catalytic cycle of type II topoisomerases requires the hydrolysis of ATP [25]: it is an active process and ATP is the 'fuel'. Type II topoisomerases do not have an equal propensity to cleave all DNA sequences. For example, using an *in vitro* technique, Burden and Osheroff [46] evolved a sequence that was scissioned at much higher rate than a random sequence by a certain organism's type II topoisomerase. Further, this lab-evolved sequence was found to be highly represented in the genome of the organism.

There exist some situations where type II topoisomerase may tend to knot DNA. For example, during replication, unwinding of the DNA tends to create super-coiling ahead of the replication fork. This super-coiling may be transferred to the region of the DNA already replicated, the replication bubble, causing it to intertwine with itself. The action of a type II topoisomerase may then knot the bubble [24, 47, 48].

2.2.3 Steady-State Level of Knotting

Rybenkov *et al.* [49] found that, if the reaction catalysed by type II topoisomerases on a substrate of DNA molecules (with ATP) is allowed to reach steady-state, then the fraction of DNA molecules that are knotted and catenated is much lower than that which is found at thermal equilibrium. The value at thermal equilibrium was determined by randomly closing DNA molecules. This is perhaps surprising, given that type II topoisomerase acts locally, whereas topology is a global property.

A model suggested by Vologodskii *et al.* [33] proposes that type II topoisomerase induces a sharp bend in DNA with a specific orientation with respect to the en-

zyme. If strand passage only occurs from the inside of the bend to the outside, then simulations [33] show that the steady-state probability of knotting is reduced by a factor of 14. In experiments on different type II topoisomerases reported in the same work, factors of between 5 and 90 were observed. A later study of the structure of a particular type II topoisomerase bound to DNA observed a $\sim 150^\circ$ bend [50].

There have been various other models proposed to explain the low steady-state level of knotting. They are briefly reviewed in ref. [51], where the possibility that super-coiling may also reduce the level of knotting is discussed.

2.2.4 Knotted Proteins

DNA is not the only biological molecule that may be knotted – knots may also be identified in some proteins. Proteins are open chains and so knotting in them is not unambiguous. Nonetheless the structures of some do conform to a 'common-sense' idea of a knot. In ref [52], for example, a 4_1 knot was identified in a plant protein and a folding pathway to form it was proposed. In ref. [53], it was suggested that the emergence of a knot in the evolution of a protein may serve to change its function.

2.2.5 Electrophoretic Separation of Knotted DNA

In experiments considering the knotting of DNA, it is crucial to be able to identify the types of knots that are formed. It is well established that DNA rings may be separated by electrophoresis on the basis of their topology, although, for example, molecules with different knots with the same number of essential crossings may not be separable. In such experiments, DNA is usually nicked using an enzyme to relax any torsional tension and avoid super-coiling. Stasiak *et al.* [5] showed that, under certain conditions, there is an approximately linear relationship between the speed of migration of a DNA knot and the average crossing number of its ideal form, with more complex knots migrating faster. Vologodskii *et al.* [54] showed that similar results

are found by applying the Kirwood-Riseman approximation to thermally agitated knotted configurations to calculate sedimentation coefficients. The suggestion is thus that hydrodynamic interactions account for the observed behaviour, although it has been argued that these are screened under typical electrophoresis conditions [55], calling this interpretation into question.

2.3 Properties of Knotted Filaments

This section presents previous work on the properties of knotted filaments. Compared to polymers, which are considered in section 2.4, this work is limited.

In ref. [56], the effect of the flexibility, f, of a tube on the length needed to form a knot is investigated. Physically, these results could relate to filaments. Moving away from the ideal knot limit of complete flexibility, one can ask how the minimum *ropelength* – the length-to-radius ratio – achievable for a particular knot depends on f. In ref. [56], f is defined as the ropelength required to form a circle (divided by 2π). It is found that, for each knot investigated, there is a phase change at $f \leq 0.5$, above which the minimum ropelength changes very slowly.

Gallotti and Pierre-Louis [57] considered the properties of stiff knotted filaments. They investigated filaments with ropelengths much larger than those of ideal knots, applying analytical approaches, Monte Carlo simulations and simple experiments to investigate the configurations adopted.

Inspired by electrophoresis results (see section 2.2.5), there has been some work looking at the sedimentation of rigid knotted filaments [58, 59]. In both these works zero Reynolds number simulations were employed and, in ref. [59], experiments using knots made of plastic of typical size $\sim 0.1m$ were also performed. The contours of the rigid filaments were those of ideal knots but the ropelengths were significantly larger. An approximate linear dependence of the sedimentation velocities on average

crossing number was observed.

2.4 Properties of Knotted Polymers

If one wants to consider knots in polymers, then the probability of them occurring is a question of fundamental importance. It was correspondingly one of the first to be addressed. Another issue to receive early attention was the effect of knots on polymer relaxation. A more difficult problem, and one that was not considered until later, is determining how much of the polymer is involved in the knot. This is crucial in understanding how knots will affect 'long' polymers. In this section, previous work on each of these questions is discussed.

2.4.1 Probability of Knotting

There has been a variety of work, analytical, numerical and experimental, on the probability that a polymer is knotted, P_{knot}. Sumners and Whittington [20] showed, using an appropriate definition of knotting for open chains, that, for both self-avoiding random walks (open) and polygons (a simple model for closed polymer rings) on a lattice, P_{knot} tends to one for sufficiently high N.

Experimentally, Shaw and Wang [60] looked at random closure of DNA molecules of two different lengths at varying ion concentrations. They observed higher P_{knot} for the longer chains and for higher ion concentrations. In ref. [30], similar results were combined with Monte Carlo simulations to deduce the effective diameter of DNA as a function of ion concentration.

There have also been various studies considering the probability of knotting for polymers in confined geometries. In ref. [61], lattice polygons in good and bad solvents in slabs (one-dimensional confinement) and prisms (two-dimensional confinement) were considered. Numerical results showed that for a given N, P_{knot} is a non-

monotonic function of D, the size of the confinement, first increasing to a maximum and then decaying.

Three-dimensional confinement has also been considered, for example in ref. [23], in which simulations of a polymer confined within a sphere of radius R show that P_{knot} increases with N and $1/R$. A similar situation has been investigated experimentally by looking at the DNA within a bacteriophage capsid [28, 62].

Experimentally, knots may also be introduced artificially into polymers. Arai *et al.* [63] used optical tweezers to tie knots in actin and DNA. Bao *et al.* [32] used a similar technique to create knots in DNA and study their diffusion.

2.4.2 Relaxation of Knotted Polymers

Knotting in a ring polymer introduces a long topological time-scale not predicted by the Rouse model. This was first observed by Quake [29], who looked at the relaxation of the radius of gyration. Quake also showed that for the polymer lengths he studied, the radius of gyration of a polymer decreases with increasing crossing number of its knot. It was later found that the topological time-scale decreases with increasing knot complexity [64]. In ref. [65], the same time-scale was observed in the knot-length autocorrelation function.

In refs. [66] and [67], simulations of knotted polymers that are cut, and then allowed to relax, were considered. In contrast to the equilibrium case, the relaxation time-scale was seen to increase with knot complexity.

2.4.3 The Size of a Knot in a Polymer

An interesting, though difficult question is how the number of monomers that form a knot, l_k, scales with the total number comprising the ring polymer in which the knot exists, N. One might claim that the answer is trivial: the topology is a global property and so the knot will always be the whole polymer. However, from everyday

experience, with string for example, it is clear that knots may be tightened. This suggests that the knot size, l_k, should be a meaningful quantity.

The scaling of l_k with N determines the degree of knot localisation:

$$l_k \sim N^{\beta} \begin{cases} \beta = 0 & \text{strongly localised,} \\ 0 < \beta < 1 & \text{weakly localised,} \\ \beta = 1 & \text{delocalised.} \end{cases} \tag{2.4}$$

The situation is simplified considerably, if *flat knots* are considered. These are two-dimensional configurations of the knotted polymer, in which the number of crossings is equal to the essential crossings, n, [68], so that the configuration is always composed of $2n$ arcs. They correspond experimentally to polymers absorbed on a surface. The size of the knot may be simply defined as the $N - l_n$, where l_n is the number of monomers in the longest arc. In the good solvent regime, simulations show that flat knots are strongly localised [31]. There is some experimental evidence to support this [69].

For three-dimensional polymers, various approaches have found that, in a good solvent, knots are weakly localised. In ref. [70], the authors used scaling arguments based on the blob picture, combined with simulations of knotted polymers under tension, to estimate $\beta = 0.4 \pm 0.1$. In ref. [71], two methods were employed. Both gave an estimate of $\beta \approx 0.75$.

In a bad solvent, for both two dimensional and three dimensional polymers, knots are delocalised [31].

Chapter 3

Models and Methods

This chapter introduces the simulation models, in section 3.1, and methods, in section 3.2, that we later apply to study various problems. Both sections follow the same basic structure: we begin with a general overview, including a wider range of approaches, before discussing our particular choices in more detail. The methods we use for checking knot type, locating knots and initialising knotted configurations are described in Appendix B.

In this thesis, we are interested in behaviour that arises from the generic properties of polymers and filaments, for example their extended, chain-like nature, their bending stiffness or the hydrodynamic coupling between spatially separated segments. We are not concerned with effects that depend on particular properties such as chemical details. For this reason, and also for computational efficiency, coarse-grained approaches are appropriate. The essence of such approaches is that many degrees of freedom in the experimental system are represented by one in the model.

3.1 Polymer Models

Simulation models of polymers cover a vast range in terms of the amount of detail included, from polygons [72], where ring polymers are represented as a closed path

on a lattice that may not visit the same vertex twice, to atomistic approaches [73].

Due to the typically large number of particles needed, the computational effort required for atomistic approaches is very high and the time-scales that may be accessed are restricted [74]. If chemical effects are under consideration, however, they may be necessary. In ref. [75], for example, the folding of a protein under confinement was investigated and an effect arising from the hydrogen bonding of water was found. As well as the polymer, an atomistic representation of the water was also included. More efficient approaches can include some solvent effects, such as hydrodynamic interactions, through the simulation method, without the full resolution of molecular detail. These will be discussed in section 3.2.

We focus on coarse-grained models. The simplest are those in which the polymer is confined to a lattice. Along with polygons, another possibility is the Bond Fluctuation model [76] in which each monomer occupies one unit cell of a d-dimensional lattice, 2^d lattice sites in all. Each site may only be occupied by one monomer and a maximum bond length is set such that bonds may never cross. In the Domb-Joyce model, again on a lattice, there is an interaction parameter that may be varied. If a critical value is chosen, then finite-size corrections are minimised, which may be useful for investigating scaling behaviour [77].

We wish to investigate dynamics. For this purpose lattice and atomistic models are both restrictive, the former in terms of the types of motions performable and the latter in terms of time-scales accessible. We choose instead to use bead-spring polymer models. Here the polymer is represented by a series of spherical beads, each typically representing many chemical monomers of an experimental system, joined by springs to model the polymer's connectedness. The beads move freely in space and the simplicity of the interactions allows efficient simulation. In the following subsection, we discuss the particular potentials for bead-spring polymers that we use.

3.1.1 Bead-Spring Models

For generic properties, the exact forms of the interactions are not crucial. A simple approach is to join the beads with harmonic springs using the potential

$$V_{harmonic} = k_{harmonic} x^2, \tag{3.1}$$

where x is the distance between the two beads that are bonded by the spring and $\kappa_{harmonic}$ is a spring constant. Another, widely used, possibility is the finitely extensible nonlinear elastic (FENE) spring potential. It was first suggested by Warner [78]. It was chosen largely for mathematical expediency. For small extensions, the force is Hookean, as for Eq. (3.1), but the parameter R_0 sets a maximum extension

$$V_{FENE} = -\frac{kR_0^2}{2} \ln \left[1 - \left(\frac{x}{R_0} \right)^2 \right]. \tag{3.2}$$

Grest and Kremer [79] suggested a polymer model where FENE springs to model bonds are combined with a truncated Lennard-Jones potential to include excluded volume:

$$\begin{aligned} V_{EV-trunc} &= 4\epsilon \left[\left(\tfrac{\sigma}{x}\right)^{12} - \left(\tfrac{\sigma}{x}\right)^{6} + \tfrac{1}{4} \right] \quad x \leq 2^{1/6}\sigma \\ V_{EV-trunc} &= 0 \qquad\qquad\qquad\qquad\qquad\quad x > 2^{1/6}\sigma, \end{aligned} \tag{3.3}$$

where ϵ is an energy scale. The excluded volume interactions are purely repulsive and the same between pairs of bonded and non-bonded beads. We make a standard choice of parameter values [79] to prevent chain crossings: $k = 30\epsilon/\sigma^2$ and $R_0 = 1.5\sigma$. For simulating knotted polymers, where chain crossing could lead to unwanted changes in topology, this is a useful property. We also combine Eq. (3.3) with harmonic springs, Eq. (3.1). In this case, we follow ref. [80] and choose $k_{harmonic} = 100\epsilon/\sigma^2$, which is sufficient to prevent chain crossings.

In Chapters 6 and 8, we also use a slight modification to Eq. (3.3), which does

not make a qualitative difference to results. Instead of truncating at $2^{1/6}\sigma$, only the x^{-12} term is used in the excluded volume interaction and it is truncated at 2.5σ:

$$\begin{aligned} V_{EV} &= 4\epsilon\left[\left(\tfrac{\sigma}{r}\right)^{12} - \left(\tfrac{2}{5}\right)^{12}\right] \quad x \leq 2.5\sigma \\ V_{EV} &= 0 \qquad\qquad\qquad\qquad\quad x > 2.5\sigma. \end{aligned} \tag{3.4}$$

Semi-flexible or stiff polymers may be simulated by including a bending potential:

$$V_{bend} = \kappa \hat{\mathbf{x}}_i \cdot \hat{\mathbf{x}}_{i+1}, \tag{3.5}$$

where $\hat{\mathbf{x}}_i$ is the unit vector in the direction of the bond from bead $i-1$ to bead i. The potential is applied for all pairs of consecutive bonds. For sufficiently high κ the persistence length, in number of beads, is κ/k_BT, where k_BT is the temperature at which the system is simulated.

Our model does not include the twist of the polymer around its contour or torsional stiffness. One approach for including torsional stiffness is to consider the dihedral angle, which is defined for groups of three consecutive bonds. However, when consecutive bonds are aligned, the dihedral angle becomes undefined [81]. Since it does not include twist either, such an approach does not give rise to a conserved linking number for closed rings. To simulate rings with a particular linking number, it is necessary to include additional orientational vectors for the beads [82], which may be used to define twist. The majority of problems we consider correspond experimentally to linear polymers or to rings that are not torsionally closed, such that the twisting of the polymer may easily relax. It is expected that twist will relax much more quickly than bending [83]. So unless there is a specific feature of the system that makes twist important, it may generally be neglected. On the other hand, if rings that are torsionally closed are considered, it may dramatically change polymer configurations because of the possibility of supercoiling. Including twist and torsion

could be an interesting extension to some of the work described in Chapters 4 to 9. In section 7.6, we do consider a filament model that introduces new degrees of freedom to include twist and torsion.

3.2 Dynamical Methods

Simulations of polymers may be performed using Monte Carlo or Molecular Dynamics type techniques [74]. In the latter, equations of motion are solved using discrete integration, often with a stochastic term to model thermal noise. In this way, realistic dynamical behaviour may be produced. In the former, in contrast, changes to the system may not correspond to physical dynamics, instead they are chosen so that different equilibrium states are sampled with a correct weighting.

The strength of Monte Carlo methods lies in their efficient determination of equilibrium properties and they are often applied to lattice models of polymers. The BFACF algorithm [72], in which updates are made either by the flipping of corners of, or the creation of handles in, the polymer, is an example of a method which may be used to sample such models. Due to the handle creation moves, it allows the total polymer contour length to vary. Other Monte Carlo methods are reviewed in ref. [84]. Since we are interested in dynamics, Monte Carlo models, in which position updates are not driven directly by forces, are less appropriate and we exclusively use Molecular Dynamics type methods.

Molecular Dynamics type simulations may be used for Brownian or non-Brownian systems. For the former, whilst hydrodynamics often play a role, perhaps the most important requirement of a method is that it produces thermal motion. This may be achieved by applying random, uncorrelated forces to beads at each time step as in Langevin dynamics, which neglects hydrodynamic interactions. Langevin dynamics is an efficient method that we apply to various problems. It is discussed in more

detail in section 3.2.1.

There are many different simulation methods that combine thermal fluctuations and hydrodynamics interactions. For systems composed of spherical particles in viscous flows, like bead-spring polymers, they may be included using mobility tensors that relate the velocities of the particles to the forces applied to them. Commonly used mobility tensors are the Oseen tensor [1] and the Rotne-Prager tensor [85], which are both comprised of truncated forms of analytic two-body solutions [86]. A more sophisticated method, introduced by Durlofsky, Brady and Bossis [87], uses mobility tensors constructed to include multi-body interactions by infinite reflections, achieved through matrix inversion. Lubrication, interactions between very close spheres, is also included [86]. As discussed in section 3.2.2, combining mobility tensor hydrodynamics with fluctuations is computationally expensive and we do not use such methods for polymers. In the non-Brownian regime, such methods are more efficient. For computational tractability, we apply the Rotne-Prager tensor in our non-Brownian simulations. It is discussed in more detail in section 3.2.2.

There are many other simulation methods that combine thermal fluctuations and hydrodynamics interactions. We describe three more schemes that have been previously used in simulations of polymers. One possibility is to couple a polymer model to a fluid simulated using the Lattice Bolzmann method [88, 89]. In Lattice Boltzmann, the fluid is represented on a grid, with a velocity distribution function at each vertex. The distributions evolve by exchange with neighbours and collisions at the nodes. The basic method does not include thermal fluctuations, so it is also applicable to the non-Brownian regime, although these may be added [88]. A second method is Dissipative Particle Dynamics [74], which represents the fluid as soft particles moving continuously in space. Three types of forces on particles are included: random and dissipative forces to maintain a finite temperature, and conservative forces to represent interparticle interactions.

The method that we choose to apply is Stochastic Rotation Dynamics [90], which is described in detail in section 3.2.3. The solvent is represented by relatively few particles and interactions between them are included in a computationally inexpensive manner. Unlike Lattice Boltzmann, thermal fluctuations are intrinsic to the method and coupling between solvent and polymer may be achieved in a very simple and efficient way.

In the following three subsections, we discuss in more detail the particular methods that we have chosen to apply. In thermal simulations we use a temperature of $k_BT = \epsilon$, where ϵ is the energy scale in our polymer excluded volume interaction, Eq. (3.3).

3.2.1 Langevin Dynamics

Langevin Dynamics is the numerical solution of the Langevin equation [91]:

$$m\ddot{\mathbf{x}}_\mathbf{i} = \mathbf{f}_\mathbf{i} - \zeta\dot{\mathbf{x}}_\mathbf{i} + \sqrt{2\zeta k_BT}\mathbf{r}_\mathbf{i}(t), \tag{3.6}$$

where $\mathbf{x}_\mathbf{i}$ is the position of the i^{th} bead, $\mathbf{f}_\mathbf{i}$ is the total force acting on it, m is the mass of the bead, ζ is a friction constant and k_BT is the temperature. $\mathbf{r}_\mathbf{i}(t)$ are random vectors that satisfy

$$\begin{aligned} \langle \mathbf{r}_\mathbf{i}(t) \rangle &= 0, \\ \langle \mathbf{r}_\mathbf{i}(t)\mathbf{r}_\mathbf{j}(t') \rangle &= \delta_{ij}\delta(t-t')\mathcal{I}, \end{aligned} \tag{3.7}$$

where $\mathcal{I}$ is the identity matrix. The second and third terms in Eq. (3.6) represent the drag due to the solvent and thermal 'kicks' received from it. According to the fluctuation dissipation theorem, the relative size of the coefficients of these terms is set by the temperature. The equation is an expression of Newton's law, relating the rate of change of momentum to the forces. The parameters may be combined to give

a convenient unit of simulation time, $t_0 = \sqrt{(\sigma^2 m/\epsilon)}$, where σ and ϵ are parameters from the excluded volume potential in the polymer model, given in Eq. (3.3).

We solve using a velocity Verlet algorithm [74]. The position and velocity, $\mathbf{v_i}$, of the i^{th} bead at time $t + \Delta t$ are obtained from those at time t according to

$$\begin{aligned} \mathbf{x_i}(t + \Delta t) &= \mathbf{x_i}(t) + \mathbf{v_i}(t)\Delta t + \frac{\mathbf{f_i}(t)}{2m}\Delta t^2, \\ \mathbf{v_i}(t + \Delta t) &= \mathbf{v_i}(t) + \frac{\mathbf{f_i}(t + \Delta t) + \mathbf{f_i}(t)}{2m}\Delta t. \end{aligned} \tag{3.8}$$

Eq. (3.8) may be derived by truncating a Taylor expansion for $\mathbf{r_i}(t + \Delta t)$ at Δt^2 and using an approximate expression for the velocity in terms of the positions at the previous and subsequent steps [74].

Polymers undergoing thermal motion are typically in the Stokes regime, where the effect of inertia is negligible. It is thus common to set m in Eq. (3.6) to zero. Simulations of this type [92] are often known as Brownian Dynamics. In the current model (with $m \neq 0$) inertia does play a role at short times but for sufficiently long time-scales the same diffusive behaviour is seen. Using $m \neq 0$ has the advantage that larger integration steps may be used.

3.2.2 Rotne-Prager Tensor

As discussed in section A.2.2, the Rotne-Prager tensor [85] is a mobility tensor which relates the velocities of a collection of spheres in creeping flow to the forces applied to them. It approximates the interactions as a sum of two-body terms and truncates

the full expression at the $\sim x^{-3}$ level. Explicitly, the Rotne-Prager tensor is

$$\begin{aligned}
\mathcal{H}_{ii} &= \frac{1}{6\pi\eta a}\mathcal{I}, \\
\mathcal{H}_{ij} &= \frac{1}{8\pi\eta x_{ij}}\left[\left(1+\frac{2a^2}{3x_{ij}^2}\right)\mathcal{I}+\left(1-\frac{2a^2}{x_{ij}^2}\right)\frac{\mathbf{x}_{ij}\mathbf{x}_{ij}}{x_{ij}^2}\right] \\
&\quad \text{if } i \neq j \text{ and } x_{ij} \geq 2a, \\
\mathcal{H}_{ij} &= \frac{1}{6\pi\eta a}\left[\left(1-\frac{9x_{ij}}{32a}\right)\mathcal{I}+\frac{3}{32}\frac{\mathbf{x}_{ij}\mathbf{x}_{ij}}{ax_{ij}}\right] \\
&\quad \text{if } i \neq j \text{ and } x_{ij} < 2a,
\end{aligned} \tag{3.9}$$

where $\mathbf{x}_{ij}$ is the vector from the i^{th} to the j^{th} bead, $\mathcal{I}$ is the identity matrix, η is the solvent viscosity and we will take the hydrodynamic radius, a, of a bead as $a = \sigma/2$ (see Eq. (3.3)). Our approach to integrating the motion is described in Chapter 7, where this method is applied.

The Rotne-Prager tensor can be used for simulations in the non-Brownian regime [93, 58]. For thermal simulations, Ermak and McCammon [94] introduced a technique which combines Brownian dynamics with hydrodynamic interactions via the Rotne-Prager tensor. To satisfy the fluctuation-dissipation theorem, there should be correlations between the thermal 'kicks' applied to different beads. To achieve this, a matrix, $\mathbf{B}$, that satisfies $\mathcal{H} = \mathbf{B}\mathbf{B}^T$ must be found. This may be done by performing a Cholesky decomposition [95] of $\mathcal{H}$ but the time required $\sim N^3$, making simulations of large systems computationally expensive. More efficient, approximate methods do exist [95].

3.2.3 Stochastic Rotation Dynamics

Stochastic Rotation Dynamics is a coarse-grained method for including hydrodynamics in simulations. It was first proposed by Malevanets and Kapral [90]. It has been used to simulate systems such as polymers [96], membranes [97] and microscopic swimmers [98]. Stochastic Rotation Dynamics simulates hydrodynamic interactions

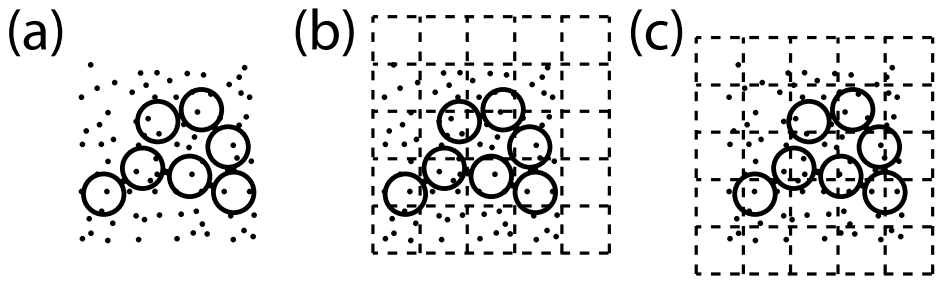


Figure 3.1: Stochastic Rotation Dynamics. (a) The polymer, represented by the chain of open circles, is embedded in a fluid of solvent particles, shown by the dots. Solvent particles may move freely throughout the system, including through positions in which they overlap with the polymer. (b) At each collision step, the system is divided into a regular grid of cells. (c) Before the collision occurs, the grid is randomly displaced to preserve Galilean invariance. In the collision, momentum is transferred between all particles within a cell, as well as any beads whose centre of mass is there. The length of one cell of the grid in (b) and (c) is a_0.

and thermal fluctuations in such a way that the first may not be included without the second. Temperature is set by the initial distribution of velocities chosen for the fluid particles. Whilst, in principle, momentum from an externally applied force would still be transferred by an initially stationary collection of particles, the stochastic nature of the interactions are incompatible with simulations without fluctuations. So the method is not suitable for situations in which thermal fluctuations are negligible such as with filaments. First, the simulation of a pure solvent is described, before we consider coupling it to a polymer.

The solvent is modelled by particles of mass m_f, whose positions and velocities at a given time are recorded. The dynamics is split into two distinct parts: each step of time t_c is composed of streaming and collision. In the streaming the particles move ballistically:

$$\mathbf{x_i^{n+1}} = \mathbf{x_i^n} + \mathbf{v_i^n} t_c, \tag{3.10}$$

where $\mathbf{x_i^n}$ is the position of the ith particle after the nth step and $\mathbf{v_i^n}$ is its velocity. In the collision step the system is divided into a regular grid of cubic cells of length a_0, as shown in Fig. 3.1(b). To preserve Galilean invariance [99], the grid is shifted by

a vector whose components are drawn from a uniform distribution over the interval $[0, a_0]$, as in Fig. 3.1(c). The velocity of particle i is then updated according to

$$\mathbf{v_i^{n+1}} = \mathbf{v_{cell}} + \mathbf{R_{cell}} \left(\mathbf{v_i^n} - \mathbf{v_{cell}} \right), \tag{3.11}$$

where $\mathbf{v_{cell}}$ is the centre of mass velocity in particle i's cell and $\mathbf{R_{cell}}$ is a rotation matrix assigned to that cell. $\mathbf{R_{cell}}$, which varies between cells and steps, performs a rotation about a random direction, picked from an isotropic distribution, by an angle α. α is a parameter of the simulation.

This procedure conserves mass, momentum and energy. Malevanets and Kapral showed that the Navier-Stokes equations may be derived from Eqs. (3.10) and (3.11). They also showed that the velocity distribution will relax to a Maxwellian form. If external forces are applied to the system, then it may be necessary to apply a thermostat. This may be done by considering a temperature defined in terms of velocities relative to cell centre of mass velocities and rescaling these – in this way the effect on the dynamics is minimised [100].

The parameters m_f, t_c, a_0 and α, along with the temperature, k_BT, and the number of particles per cell, ρ, determine the properties of the simulated solvent such as its viscosity [101].

It is possible to couple a solute to a Stochastic Rotation Dynamics solvent though a potential [100]. With such an approach, the fluid particles must be updated at every Molecular Dynamics step. For a bead-spring model of a polymer an alternative, more efficient approach, which we apply here, is to include the polymer beads in the collision step [102]. Such a scheme is depicted in Fig. 3.1(a). The motion of the polymer is integrated using the velocity Verlet algorithm [74], given in Eq. (3.8), and only interacts with the fluid at the collisions. The mass of a polymer bead, M_b, an additional simulation parameter, determines the coupling of the beads to the solvent.

Simulations without hydrodynamic interactions may be easily performed by randomly exchanging fluid particle velocities at each step, so that local velocity correlations are lost.

Here the parameters are chosen as $a_0 = \sigma$, $t_c = t_0 = \sigma/2\sqrt{m_f/k_BT}$, $m_f = 4$, $k_BT = \epsilon$, $M_b = 16$, $\rho = 5$ and $\alpha = 3\pi/4$. σ and ϵ are the length and energy scales, respectively, in the excluded volume potential of the chain, Eq. (3.3). This gives a relatively high mean-free path for fluid particles of $\lambda = 0.5a_0$: as we show later, this choice is sufficiently short to produce hydrodynamic interactions between monomers and choosing a higher value improves computational efficiency.

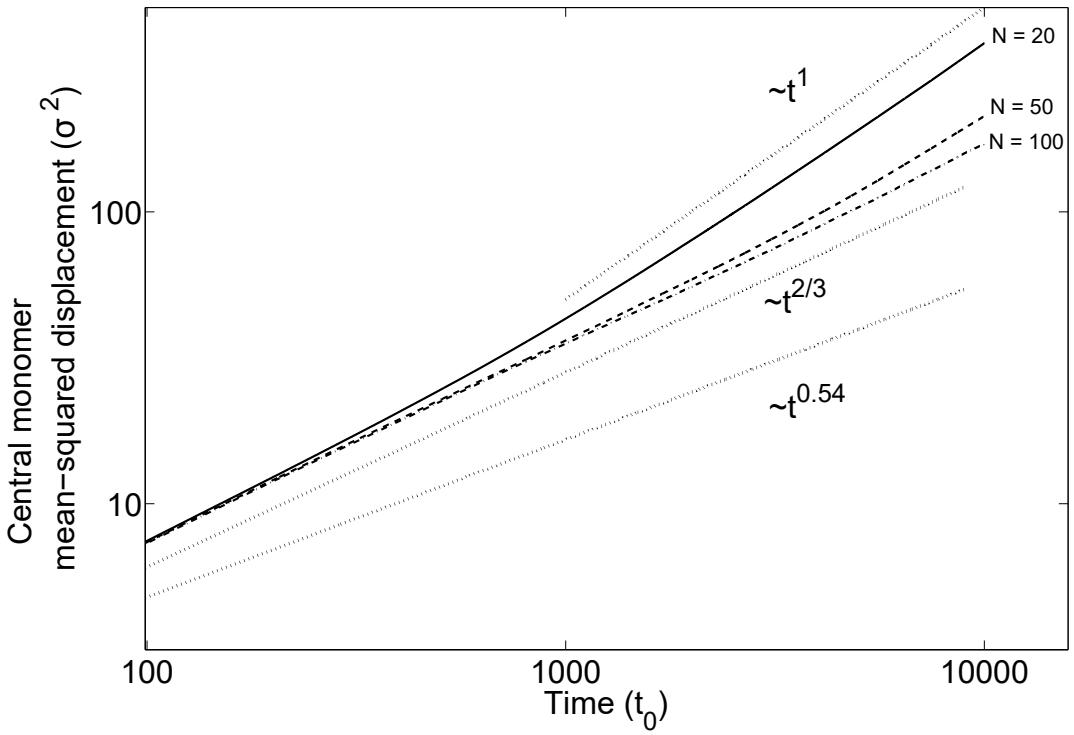


Figure 3.2: The mean-squared displacement of a monomer of a chain of length, $N = 20$ (solid line), $N = 50$ (dashed line) and $N = 100$ (dot-dash line) in an Stochastic Rotation Dynamics solvent. The dotted lines have slopes of 1, 2/3 and 0.54 as labelled. The Zimm model predicts $\sim t^{2/3}$ behaviour before diffusive behaviour ($\sim t$) sets in [88]. The Rouse model, on the other hand predicts $\sim t^{0.54}$ [88]. The central monomers only are considered, to avoid end effects.

A demonstration of the simulation of polymers using Stochastic Rotation Dynamics, with the parameter values specified, is given in Fig. 3.2. Simulations of a freely diffusing polymer were performed using the model with FENE springs, see Eq. (3.2). The Zimm model, which describes polymers with hydrodynamic interactions between monomers, predicts that in the sub-diffusive regime below the Zimm time, the mean-squared displacement of a single monomer will increase with time $\sim t^{2/3}$ [88]. The Rouse model, which does not include hydrodynamics, predicts $\sim t^{0.54}$. Brief descriptions of the properties of the Rouse and Zimm models are given in Appendix A. Plotting the monomer mean-squared displacement in Fig. 3.2 shows Zimm rather than Rouse behaviour.

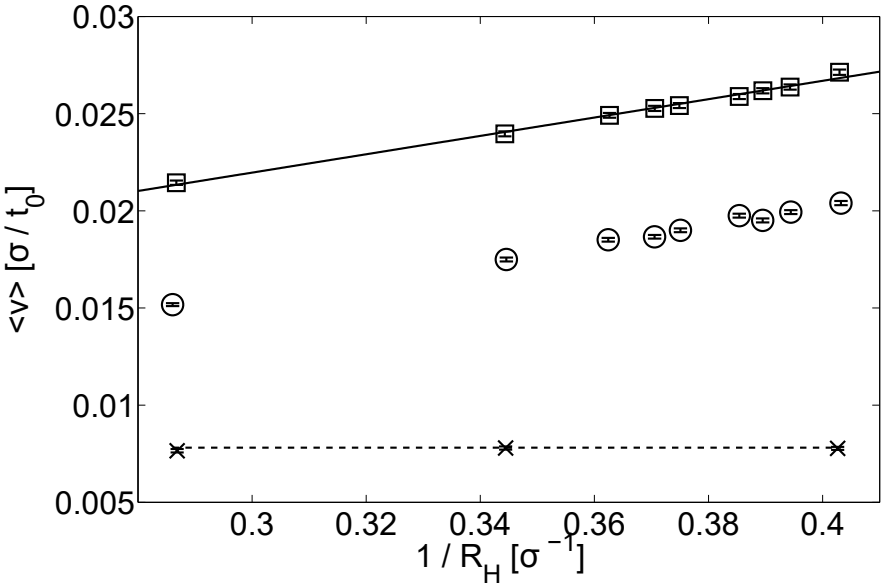


Figure 3.3: Sedimentation velocities, $\langle v \rangle$, for ring polymers of $N = 50$ beads with different knot types subject to a force of $f_{sed} = 0.1 k_B T/\sigma$ per bead. Results are presented for simulations without hydrodynamics ($\times$) and with hydrodynamics for system sizes of 16σ ($\bigcirc$) and 64σ ($\square$). The dashed line is at $\langle v \rangle = f_{sed}/\zeta_0$, where ζ_0 is the friction coefficient for a single bead. The solid line is a fit to the results for the larger system. It has a slope of $0.047\sigma^2/t_0$ (calculated with an error of $0.002\sigma^2/t_0$).

As a second demonstration of Stochastic Rotation Dynamics, the sedimentation of knotted polymers is briefly considered. Knotted ring polymers of N = 50 beads

were simulated, again using the model with FENE springs, Eq. (3.2). Knot types 0_1, 3_1, 4_1, 5_1, 5_2, 6_1, 7_1, 7_2 and 8_1 were considered.

Simulations were performed in a cubic simulation box with periodic boundaries in all directions. A force, $f_{sed} = 0.1k_BT/\sigma$, was applied to each bead. At every step the average momentum in the force direction was subtracted from each fluid particle. The average sedimentation velocity in the direction of the force, $\langle v \rangle$, was measured together with the hydrodynamic radius, defined as $1/R_H = 1/N^2 \left\langle \sum_i \sum_j \frac{1}{|\mathbf{x}_i - \mathbf{x}_j|} \right\rangle$ [102], where $\mathbf{x}_i$ are the positions of the individual beads. We checked that the Reynolds number, calculated as $R_H \langle v \rangle / \nu$, where ν is the kinematic viscosity, η/ρ, where ρ is the density, of the solvent, was less than 0.1 for all simulations.

In Fig. 3.3, we plot results for simulation boxes of length 16σ and 64σ and compare results from simulations without hydrodynamic interactions. In the latter case, the polymers sediment with a velocity f_{sed}/ζ_0, where ζ_0 is the friction coefficient of a single bead (measured from simulation), as expected for Rouse polymers [1]. When hydrodynamics are introduced, the sedimentation velocity increases significantly. A linear dependence on $1/R_H$ is seen, again as expected [102]. Comparing the results for the two system sizes shows that there are relatively strong finite-size effects, which is typical for systems with hydrodynamics. Due to interactions with periodic images, simulations with periodic boundaries are equivalent to finite concentrations: a smaller system size corresponds to a higher concentration, leading to lower sedimentation coefficients [103]. The Kirkwood formula [102], a simple approximation calculated using Oseen tensor hydrodynamics, which is outlined in section A.2.2, predicts the hydrodynamic contribution to the sedimentation velocity to be $Nf_{sed}/6\pi\eta R_H$, which gives $0.055\sigma^2/t_0 \times 1/R_H$ for our parameters. The non-hydrodynamic contribution is equal for all knot types since N is the same. Making a linear fit to the results for the larger system gives a slope of $0.047 \pm 0.002\sigma^2/t_0$. The value may be lower partly due to finite size effects but, as discussed in ref. [102], the Kirkwood formula is also

generally found to produce overestimates.

We do not pursue these issues further as we have already achieved our purpose: the results clearly show that the Stochastic Rotation Dynamics solvent produces hydrodynamic interactions between monomers.

3.3 Summary

This chapter has described the models and methods that we now go on to apply to specific problems, put in a broader context of others available in the literature. In terms of simulation methods, we use Langevin dynamics for problems where we are interested in statics, such as Chapters 4 and 9, or where hydrodynamics are screened, as in Chapter 5. For the remaining problems, where we are primarily interested in dynamics, we use either a method based on the Rotne-Prager tensor or Stochastic Rotation Dynamics. The methods we use for checking knot type, locating knots and initialising knotted configurations are described in Appendix B.

Chapter 4

Knotted Polymers under Compression

4.1 Introduction

In this chapter, we investigate the effect of knot type on the properties of a ring polymer in a slit. As discussed in section 2.2.2, in biology, knots commonly form in DNA confined in cells. So the interplay of knotting and confinement is interesting and important to understand. We also look briefly at the effect of knotting on the shape of unconfined ring polymers. This is not directly related to our main topic but highlights an important point to bear in mind when considering it: the behaviour of knotted polymers may be strongly dependent on the total chain length.

The confinement of linear polymers in a slit, between two infinite, parallel walls has been well studied. The simplest model is to consider a single polymer with walls that provide only geometric constraints. For $D > R$, where D and R are slit and polymer size respectively, the chain will maintain a shape similar to that seen without confinement. For $D < R$, however, significant deformation of the chain occurs. As well as predictions for its size, a scaling form for the free energy of such a chain

for $D < R$ was given in ref. [104], using the blob picture, which is discussed in section A.1.5,

$$\frac{F_{conf}}{k_B T} \approxeq N \left(\frac{a}{D}\right)^{1/\nu}, \tag{4.1}$$

where N is the number of monomers in the chain, a is monomer size and ν is a three dimensional exponent $\approx 3/5$. Some of these predictions were verified in ref. [105]. Later it was predicted that the ratio between the monomer density by the wall and the force exerted on the wall is universal, independent of microscopic details [106]. Again, attempts have been made to verify this prediction by simulation, see ref. [77] and references therein. Whilst the majority of simulation work has used Monte Carlo methods, a recent study has also compared the results of Molecular Dynamics simulations to scaling predictions [107]. Other work has considered issues such as attractive walls [108].

By comparison to the case of linear polymers, there has been little work on knotted ring polymers in slits and basic issues remain open. We next briefly summarise the three main previous works on this problem.

Tesi *et al.* [61] looked at the probability that a knot will be found in a polymer if it is confined to a slit. It was found that, for relatively wide slits,the probability increased as the slit width decreased. However, for narrower slits, the probability peaked and eventually became less than the value for wide slits. Polygons were employed as the polymer model.

As well as analytical calculations, Janse van Rensburg [109] applied the BFACF algorithm described in section 3.1 to confined knotted polymers. This algorithm allows the number total of polymer segments to change and its variation with slit width was investigated. Knotted polymers were found to expand as the width increased. This was in contrast to unknotted polymers, whose size showed a plateau after a certain width was reached.

Finally, in ref. [70], the ends of knotted and unknotted polymers were attached

to parallel plates, separated so as to *stretch* the chains. It was found that the forces exerted on knotted polymers deviated from scaling predictions. The results were used to deduce an estimate of how the knot size scales with polymer length.

4.1.1 Summary and Overview

Motivated by the common occurrence of confined knotted polymers in biology, we work towards the important goal of understanding such systems by using a coarse-grained model to gain insight into the behaviour of knotted ring polymers in a slit. Unlike for linear polymers, previous work with knots in confinement has not looked at basic quantities such as the force exerted on the walls. After checking our approach by considering linear polymers, we begin by looking at the force. We then go on to look at other quantities, such as the radius of gyration and the monomer density distribution, that help us to interpret the trends seen in the force results.

We find that the effect of knotting is strikingly different depending on how confined the polymer is. We find that for 'narrow' slits, more complex knots exert higher forces on the walls, whereas for relatively 'wide' slits, the opposite is true. As expected, the forces are related to the monomer densities near the walls and this leads us to an interpretation of the force results in terms of the effect of knots on the ability of the polymer to spread out in the slit.

Before presenting the confinement results, we first take a brief detour and look, in section 4.2, at the asphericity of unconfined knotted polymers. The results emphasise the importance of total polymer length in knot problems, which is relevant when considering our main direction.

4.2 Asphericity of Knotted Polymers

We begin by briefly presenting a few pertinent results on the asphericity of knotted polymers in a good solvent. This problem has been previously investigated [110, 111]: considering polymers with a few different knot types, the asymptotic values of a shape measure designed to indicate the degree of asphericity were estimated. The results suggested that all knot types tend to the same shape in the large N limit. Given the evidence that knots in a good solvent are weakly localised [71], this makes sense. At a fixed polymer length, it was found that polymers with more complex knots tend to be more spherical.

In the previous work [110, 111], the focus was on a small number of knots. Here we look at many more different knots for two, relatively small, values of N. We employ the asphericity measure, Δ_0, discussed in section A.1.2. Briefly, $0 \leq \Delta_0 \leq 1$, with $\Delta_0 = 0$ indicating spherical symmetry and $\Delta_0 = 1$ indicating a highly aspherical shape, such as a rod or a flat disc. These results are not directly related to the main problem considered in this chapter but are an interesting and important demonstration of the importance of total polymer length in knot problems. So, being insufficient to warrant an individual chapter for themselves, they are included here.

We present results for polymers of $N = 100$ and 500 beads obtained using the Langevin dynamics method described in section 3.2.1 and the polymer model with harmonic springs, defined by Eq. (3.1). Errors were estimated by comparing the relaxation times, estimated from auto-correlation functions for Δ_0, to the total simulation time to determine the number of independent data points. As discussed in section 2.4.2, knots introduce a new time scale into the relaxation of polymers. For $N = 100$, the relaxation time is typically on the order $10^2 t_0$. After initialisation, averages are taken over $10^6 t_0$. For $N = 500$, polymers relaxation is on the order of $10^3 t_0$ and averages are taken over $10^7 t_0$.

Fig. 4.1 plots the asphericity, $\langle \Delta_0 \rangle$, for $N = 100$ polymers for all prime knot types

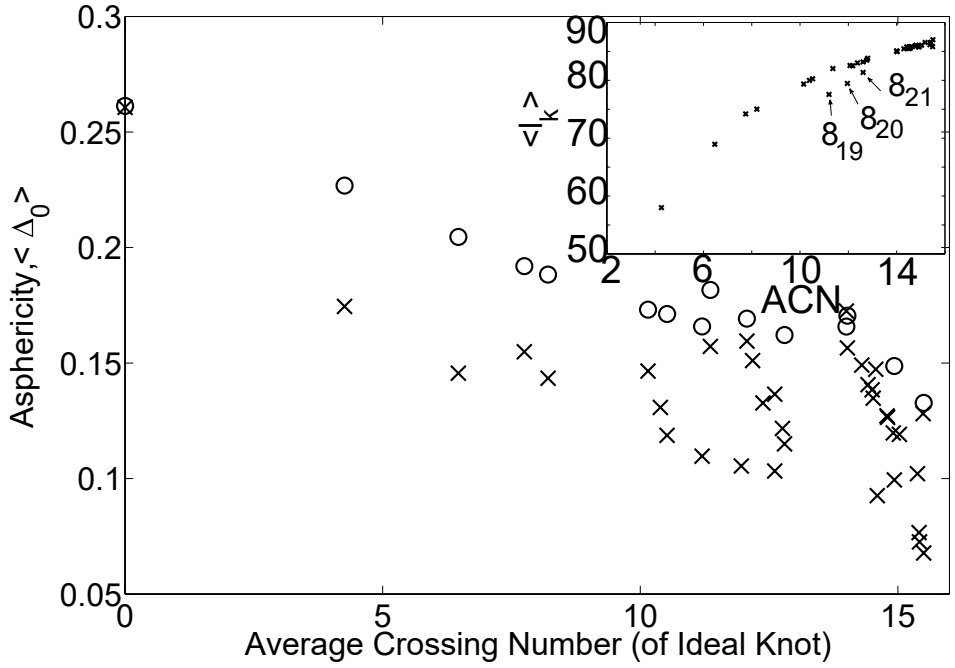


Figure 4.1: The asphericity, $\langle \Delta_0 \rangle$, as a function of average crossing number of the ideal form of the knot type (from ref. [42]) for polymers of $N = 100$ ($\times$) and $N = 500$ ($\bigcirc$) beads. For $N = 100$ all prime knots with up to 8 essential crossings are plotted. For $N = 500$ a smaller selection of knots, which span the range of $\langle \Delta_0 \rangle$ seen for $N = 100$, are chosen. The inset plots the average knot length as a percentage of the total polymer length as a function of average crossing number for N = 100. Three knots that do not fit the general trend are labelled. Error bars are smaller than the size of the data points.

with up to and including 8 essential crossings. In order to separate the data points on the x-axis, we plot $\langle \Delta_0 \rangle$ as a function of average crossing number of the ideal form of the knot from ref. [42]. In agreement with previous results [110, 111], it is seen that initially the polymers become more spherical as the knot complexity is increased. At higher complexities, however, the spread of the results increases greatly and no obvious trend is apparent. This is because more complex knots typically take up more of the polymer. When the knot is relatively small compared to the total length, it has a generic effect not dependent on its type but, as it gets larger, the whole polymer is forced to take on a shape determined by the particular knot topology.

Results for $N = 500$ are also plotted in Fig. 4.1. A smaller number of knots were chosen. We ensured that knots that lie at the extremes of the spread for $N = 100$ were included. We note that the values for the unknot, plotted at 0 on the x-axis, for both N are very similar. Comparing the results for non-trivial knots shows that the spread at higher complexities increases as N is decreased. Due to the weak knot localisation discussed in section 2.4.3, the size of the knot relative to the whole polymer is smaller for larger chains. So, for $N = 500$, even the most complex knots remain relatively small and the effect of their particular topology is less evident.

In the inset in Fig. 4.1, the average knot length for $N = 100$, measured using the algorithm described in section B.3, is plotted. Finding knots in chains of length $N = 500$ became impracticably slow. The rate of configurations for which the knot position could not be determined was never more than 0.002%. We found that, for the more complex knots, the knot length does approach the polymer length. Interestingly, the inset in Fig. 4.1 shows that three knots – 8_{19}, 8_{20} and 8_{21} – appear to deviate significantly from the trend followed by all the others. The reason for this difference would perhaps be interesting to investigate further.

The results shown emphasise the point that since knots in polymers in a good solvent are weakly localised, the behaviour of knotted polymers may be strongly dependent on the total chain length and more interesting effects may be seen when the polymer is relatively short.

4.3 Model

We now turn our attentions to the main topic of the chapter, the confinement of knotted polymers in a slit. We use the polymer model with FENE springs, Eq. (3.2), simulated using the Langevin Dynamics method described in section 3.2.1. In addition, the walls are included by the same excluded volume potential as in the bead-bead

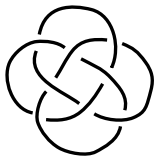


Figure 4.2: Knot topology for 8_{18}, based on a diagram from ref. [34].

interactions, Eq. (3.3). The surfaces of the walls are taken as lying at the point at which the potential is truncated. We consider slit widths from $D = 4\sigma$ to $D = 18\sigma$. This range was chosen, through initial exploratory simulations, to show the crossover between the regime where more complex knots are harder to confine and that where they are easier to confine. The simulations resemble those of Dimitrov *et al.* [107], who applied them to linear polymers in confinement.

We consider linear and unknotted ring polymers and also polymers with five different knot types: 3_1, 6_1, 8_{18}, 9_1 and 12_1. The 8_{18} knot is chosen because, in the results on the asphericity of knotted polymers described in section 4.2, it was found to lie at the extremity of the range, showing the most spherical shape of all the knots investigated. In Fig. 4.2, we show a knot diagram for 8_{18}.

We choose a polymer length, $N = 300$, which is sufficiently short that the knots will significantly affect the polymer properties. It should be borne in mind that, since knots in polymers in a good solvent are localised [65], different results would be obtained for other values of N. The results do, however, give a qualitative picture of how a knot, *which is of significant length compared to* N, will affect a polymer in a slit. The radius of gyration of the unconfined linear polymer, $R_g(\text{linear}) = 14.2 \pm 0.1\sigma$. For the ring polymers with different knots, $R_g(0_1) = 10.65 \pm 0.03\sigma$, $R_g(3_1) = 9.01 \pm 0.02\sigma$, $R_g(6_1) = 7.78 \pm 0.01\sigma$, $R_g(8_{18}) = 6.86 \pm 0.01\sigma$, $R_g(9_1) = 7.28 \pm 0.01\sigma$ and $R_g(12_1) = 6.90 \pm 0.01\sigma$.

The starting configurations for the polymers were created by performing runs in which D was reduced at a rate of $10^{-4}\sigma/t_0$ from a wide slit, $D = 25\sigma$, to the

narrowest slit we considered, $D = 4\sigma$. The final configuration was then taken as the starting configuration for all the simulations at different D for the particular knot type. By performing extra compression runs, it was checked that the configurations used were not 'unusual': all those seen at end of the additional compression runs were qualitatively similar. When viewed from the direction across the slit, they showed a number of chain crossings that was typically equal to, or only slightly larger than, the essential crossings of the knot.

Simulations for each D were performed separately. Starting from a polymer in the configuration obtained from the compression run, an initialisation of period of $10^5 t_0$ was allowed before results were recorded over $10^7 t_0$. Slower relaxation was seen in the two free directions than the confined direction and relaxation also depended on knot type and D. The relaxation time in the free directions, taken as the time for the auto-correlation function of the relevant component of the radius of gyration to decay to $1/e$, was typically on the order of $10^2 t_0$ for the knotted polymers and even for the slowest case ($D = 4\sigma$, linear polymer) was clearly less than $10^4 t_0$.

4.4 Results

4.4.1 Comparison to a Scaling Prediction for Linear Polymers

Taking linear polymers first, we start by considering how our results fit with a scaling prediction. From our simulations we determine a, the monomer-monomer spacing along the chain, as 0.971σ. For slit width, D, comparable to a, it is known that a correction, δ, is needed to achieve good agreement [107]. We fit our data for linear chains to the scaling formula [107]

$$fa = B\nu^{-1}N(D/a + \delta)^{-1-1/\nu}, \tag{4.2}$$

where f is the force on the walls of the slit and B is the confinement free energy per blob. Eq. (4.2) is essentially Eq. (4.1) differentiated, with the correction, δ, included.

Dimitrov *et al.* [107] found excellent agreement with Eq. (4.2) using a value for the scaling exponent, $\nu = 0.588$, valid in the large-N limit. It is, however, known that many polymer models approach this limit rather slowly [77] and the results of Dimitrov *et al.* are surprising. We investigate this issue by taking ν, as well as δ, as a fitting parameter.

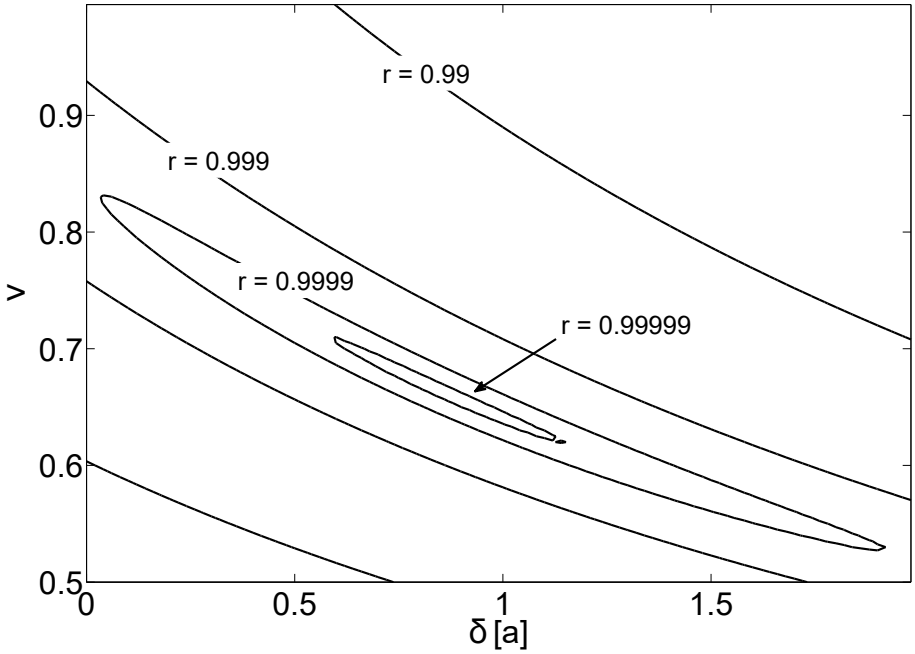


Figure 4.3: Contour plot of the correlation coefficient, r, as a function of ν, the scaling exponent and δ, the finite-size correction. Values of r closer to 1 indicate a better fit. The best fit is found for $\nu = 0.66$ and $\delta = 0.88$.

We find that there are a broad range of values for ν and δ, for which good fits to the data may be obtained. We illustrate this in Fig. 4.3: r is the correlation coefficient, defined as $(\sigma^2_{xy})^2/\sigma^2_x\sigma^2_y$, where x and y represent the quantities on the right and left sides of Eq. (4.2) respectively, σ^2_{xy} is the covariance of the data for them and $\sigma^2_{x/y}$ the variance of each individually. r indicates how good a fit to the data may be obtained

using different values; it approaches 1 as the fit improves. We find the best fit, with $r = 1 - 4 \times 10^{-7}$, for $\delta = 0.88$ and $\nu = 0.66$. However, Fig. 4.3 clearly shows there are many other values of ν and δ that would give almost as good fits. If $\nu = 0.588$ is assumed, then $\delta = 1.38$ gives the best fit.

The value of ν for our best fit differs significantly from the value for large N, in contrast to the findings of Dimitrov *et al.*. The number of blobs may be calculated as $N(D/a + \delta)^{1/\nu}$. Given that for $D = 18\sigma$ the number of blobs ≈ 2 , it is unsurprising that results that deviate from the asymptotic predictions are found.

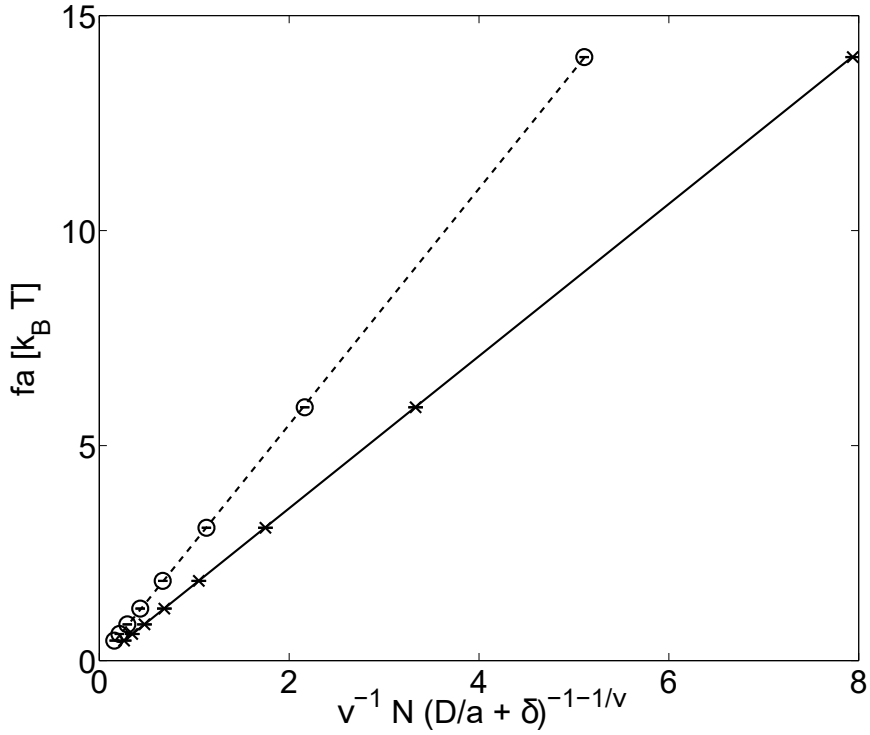


Figure 4.4: The force on the walls of the slit due to a confined linear polymer, as a function of a dimensionless combination of parameters (see Eq. (4.2)). For ($\times$) the values of ν and δ are taken as those found to give the best fit of the results to Eq. (4.2) (see Fig. 4.3), the solid line has a slope of $B = 1.77 k_B T$. For ($\bigcirc$) the value of ν is 0.588, for which the best fit to the data is obtained with $\delta = 1.38$. The dashed line has a slope of $B = 2.78 k_B T$.

Fig. 4.4 shows how the average force on the confining walls varies with confinement,

plotted using the optimal values for δ and ν given above and also using the value of δ found when ν is fixed at 0.588. As may be seen, the linearity of the fit is very good in both cases. This may explain why Dimitrov *et al.* obtained such good results for $\nu = 0.588$: multiple fits that show good linearity are possible. However, the large difference in the slope, which determines the free energy per blob, B (see Eq. (4.2)), shows that a reliable value for this quantity may not be obtained.

Errors in Fig. 4.4 and subsequent figures were estimated from the variance of the relevant quantities, initially assuming that all data points were independent. During the simulations data was recorded every $100t_0$. If the estimate of the relevant correlation time, t_C, was seen to be significantly greater than $100t_0$ then the estimated error was increased by a factor of $\sqrt{2t_C/100t_0}$ [74].

4.4.2 Knotted and Unknotted Ring Polymers Compared to Linear Polymers

We next consider the force exerted on the confining walls by the polymer as function of D for different knot types. The average force is plotted as a ratio to the value for a linear chain in Fig. 4.5. We note that, for some of the more complex knots, an increase in the internal energy of the chain larger than the standard error is observed: for narrow slits and complex knots, the probability of collision increases and so the amount of overlap between monomers is higher, leading to an internal energy increase due to the excluded volume interaction. The largest such increase, $\Delta U = 0.56 \pm 0.06 k_B T$, is seen for 12_1 between $D = 8\sigma$ and $D = 4\sigma$. In the middle of this range, the force on the confining walls is $7.734 \pm 0.003 k_B T/\sigma$. This suggests that the internal energy increase accounts for $\lesssim 1\%$ of the free energy increase of the chains, with the rest being due to entropy. We are thus confident that this effect, which depends on the specific potential chosen, does not affect our conclusions, which are qualitative.

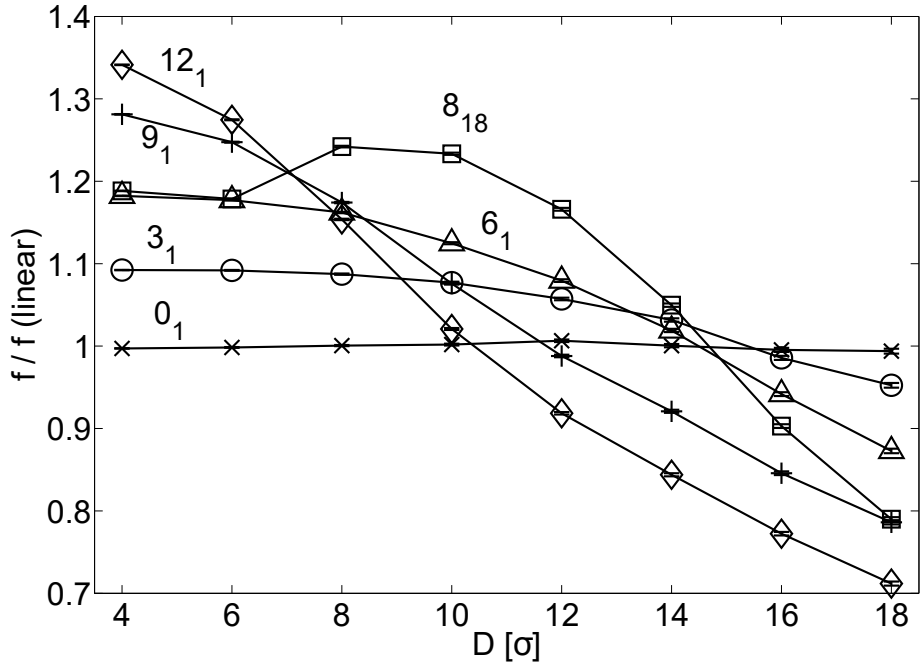


Figure 4.5: The average force exerted on the walls of a confining slit by polymers with different knot types – 0_1 ($\times$), 3_1 ($\bigcirc$), 6_1 ($\triangle$), 8_{18} ($\square$), 9_1 ($+$) and 12_1 ($\Diamond$) - as a function of slit width, D, divided by the values for a linear chain. 0_1 denotes an unknotted ring.

Interestingly, Fig. 4.5 shows that, although differences greater than the standard errors are seen, the forces exerted by linear polymers and unknotted ring polymers are very similar over the range of slit widths investigated. Since linear polymers have a larger radius of gyration, it would be expected that for wide enough slits the values for the unknot would decrease below those for linear polymers. Although it is not clearly visible in Fig. 4.5 this trend is indeed seen by checking for values of D up to $D = 30\sigma$, at which the unknot value is 0.886 ± 0.006 of the linear polymer value. At $D = 30\sigma$, the component of the radius of gyration in the direction of confinement is $5.24 \pm 0.01\sigma$ for a linear polymer, compared to $5.14 \pm 0.01\sigma$ for an unknotted ring. For 'small' slit widths, however, both linear and ring polymers should form the same number of blobs since this is determined by D and N.

The scaling picture of a confined polymer is based on it forming a series of separate

blobs. The topological constraints of a knot that is relatively large compared to the polymer prevent it from doing this. So it may be expected that results for knotted rings will deviate from those for linear and unknotted polymers. Fig. 4.5 shows this. For 'narrow' slits, the polymers with more complex knots exert a higher force whilst for 'wide' slits the opposite is true. The crossover from exerting a greater force than the unknot, to exerting a lesser, occurs at smaller slit widths for more complex knots – the onset of the 'strong' confinement regime depends on the size of the polymer compared to the slit and more complex knots are more compact [29]. The results for 8_{18}, picked because it showed interesting behaviour in section 4.2, show, uniquely amongst the knots studied, non-monotonic behaviour for the force as a ratio to the linear polymer. We do not currently understand the reasons for this but it would be interesting to investigate further.

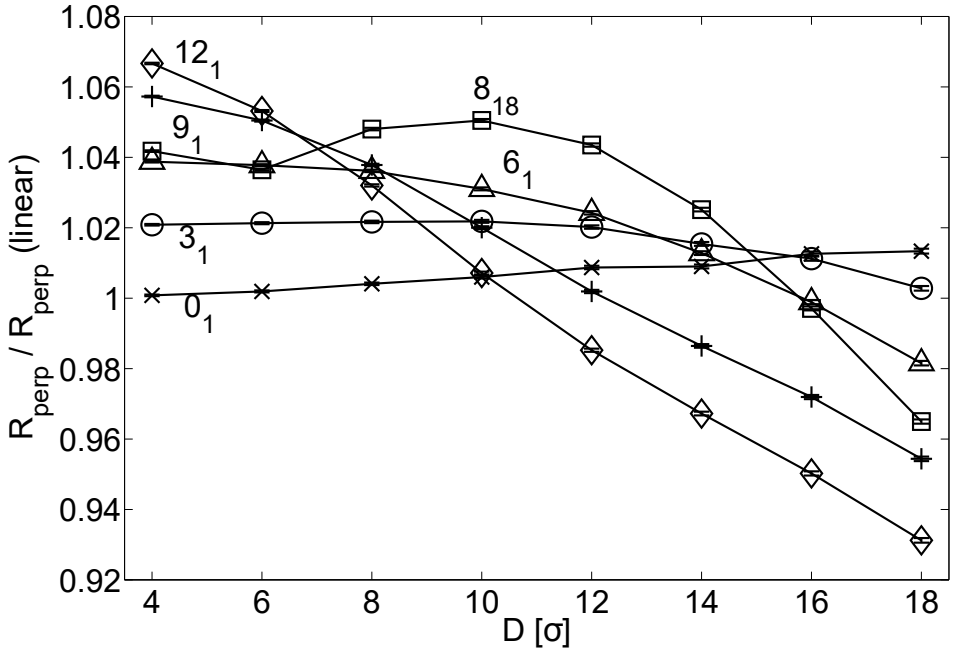


Figure 4.6: The radius of gyration, in the direction across the slit, of confined polymers with different knot types – 0_1 (×), 3_1 (◯), 6_1 (△), 8_{18} (□), 9_1 (+) and 12_1 (◇) – as a function of slit width, D, divided by the values for a linear chain.

We next consider the radius of gyration of the polymers, focussing on the com-

ponent in the confined direction, R_{perp}. In Fig. 4.6, results are plotted as ratios to the values for a linear polymer. The results for R_{perp} show very similar trends to those seen for the forces: as may be appreciated by comparing Figs. 4.6 and 4.5, the ordering of the different knot types is almost identical for all D.

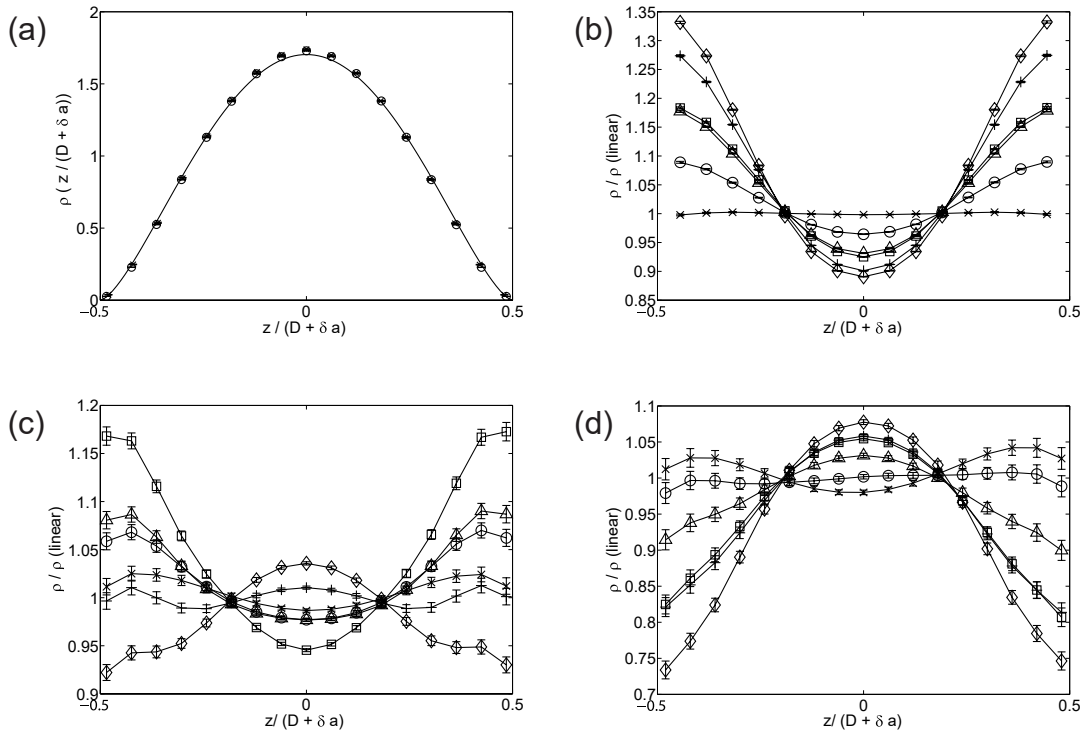


Figure 4.7: (a) Monomer density across the slit for $D = 12\sigma$ (◯) and $D = 18\sigma$ (×) for linear polymers. The solid line is the predicted scaling formula [77, 107]. The values of δ and ν (used in the scaling formula) are those found to give the best fit of results for forces to Eq. (4.2), see Fig. 4.3. The distribution for $D = 4\sigma$ is similar but shows larger deviations from the scaling formula. (b)-(d) Comparing monomer density as function of the position across the slit for various knot types: 0_1 (×), 3_1 (◯), 6_1 (△), 8_{18} (□), 9_1 (+) and 12_1 (◊). Results are plotted as ratios to the values for linear polymers. Results for $D = 4\sigma$ (b), $D = 12\sigma$ (c) and $D = 18\sigma$ (d) are shown. The slit was split into 17 bins.

4.4.2.1 Monomer Density

To help understand the results seen for f and R_{perp} shown in Figs. 4.5 and 4.6, we look at the monomer density as a function of position across the slit for various D.

The results are shown in Fig. 4.7.

Firstly, in Fig. 4.7(a), we compare the results for linear polymers to the following scaling formula for monomer density [77, 107]:

$$\rho(\zeta) = \frac{\Gamma(2+2/\nu)}{(\Gamma(1+1/\nu))^2}(1/4-\zeta^2)^{1/\nu}, \tag{4.3}$$

where ζ is the position across the slit divided by $D+\delta a$. We use the optimal values of δ and ν, determined earlier by fitting results for forces to Eq. (4.2). As for the forces in Fig. 4.4, other values of δ and ν also give comparably good fits to the data. Results for $D = 12\sigma$ and $D = 18\sigma$ show reasonable agreement with the scaling formula, though clear differences are seen, particularly near the centre of the slit. Results for $D = 4\sigma$, which are not plotted, show more noticeable deviations although the same qualitative form is seen.

In Fig. 4.7(b)-(d), we compare results for different knot types for $D = 4\sigma$, 12σ and 18σ by plotting results as ratios to those for linear polymers. The same trends in the ratios between different knot types and linear polymers as in Figs. 4.5 and 4.6 are seen for the monomer densities near the edges. Indeed, if the ratios of the monomer densities in the last bin before the walls are compared to the ratios for the forces, then almost semi-quantitative agreement is seen. As discussed in ref. [77], it is intuitively clear that the force on the wall should be proportional to the monomer density by it. If there are high monomer densities near the walls, then R_{perp} will also be higher. The agreement is imperfect partly because of the finite bin width used; there will be contributions to the edge bins from positions not quite at the walls. Our interactions are also to some extent soft, meaning that the wall position is not well defined.

Fig. 4.7 shows that knots change how the polymer is distributed across the slit. This in turn changes the force it exerts on the walls. For 'wide' slits, $D \gtrsim 14\sigma$, the constraints of more complex knots make the polymer more compact [29], leading to

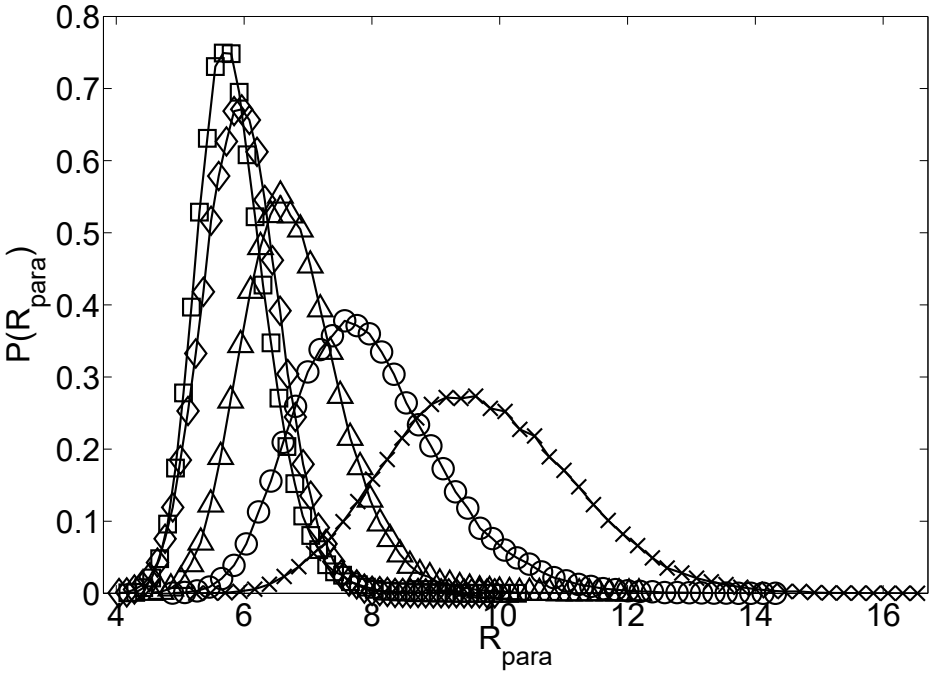


Figure 4.8: The distribution of the (instantaneous) radius of gyration in the two free directions, R_{para}, for ring polymers in a slit of $D = 18\sigma$ with different knots: 0_1 ($\times$), 3_1 ($\bigcirc$), 6_1 ($\triangle$), 8_{18} ($\square$) and 12_1 ($\Diamond$). Results for 9_1 are omitted to improve the clarity of the plot but are seen to fit with the general trend.

a lower monomer-density at the walls. For 'narrower' slits, $D \lesssim 8\sigma$, more complex knots cause the wall density to increase. A clue as to why may be found by looking at the distribution of (instantaneous) R_{para}, the radius of gyration in the two unconfined directions, for a 'wide' slit, $D = 18\sigma$. As shown in Fig. 4.8, for more complex knots the distribution is narrower and has a maximum at lower R_{para}: the more complex knots prevent the polymer from exploring configurations with large R_{para}. So when the slit becomes 'narrow' and significantly distorts the polymer, the polymer cannot distribute its monomers further out in the free directions and instead their density near the wall increases. As shown in the Fig. 4.9, the increase in R_{para} from $D = 18\sigma$ to $D = 4\sigma$ is less for more complex knots.

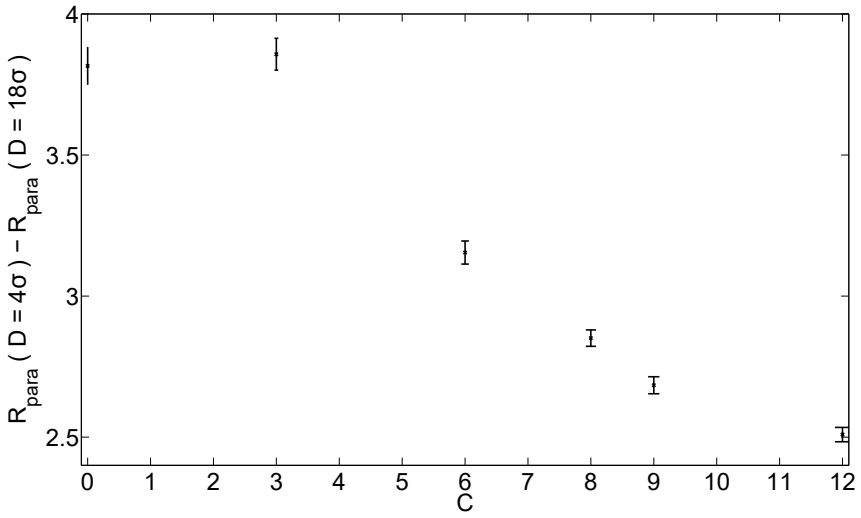


Figure 4.9: The change in the radius of gyration in the two free directions, R_{para}, between slits of width $D = 18\sigma$ and $D = 4\sigma$ for different knot types. Knot type is indicated on the horizontal axis by C, the essential crossings.

4.4.3 Summary and Discussion

To summarise, we have investigated the effect of knot type on the properties of a ring polymer confined in a slit of width D. We have found that more complex knots exert lower forces than a linear polymer on 'wide' slits but higher forces on 'narrow' slits. Due to the effect of knot type on the size of the polymer, the crossover occurs at different slit widths for different knots, leading to non-monotonic behaviour as a function of knot complexity at intermediate D. The example of 8_{18} shows that the particular topology of the knot may also play a role. 8_{18} may be different because polymers with this knot have an unusual, more spherical shape (determined using the simulations described in section 4.2), which alters their response to confinement. As expected, the forces are seen to correspond to the monomer densities near the walls. It is suggested that the increases in monomer density for lower D are related to the effect of the knot on how the polymer may extend in the free directions.

Although we exclusively consider one polymer length, the effects we have un-

covered should be generic: except in the large-N limit, knots make polymers more compact and will decrease their ability to spread out as they are confined. We expect that there is a wide range of polymer lengths for which similar qualitative trends will be observed. The results could act as a guide for further work looking at polymers with other N. Another interesting issue to be explored in the future is the crossover from weak to strong knot localisation as the polymer is confined: as discussed in section 2.4.3, polymers in a good solvent in three-dimensions are weakly localised, whilst those in two-dimensions are strongly localised. Finally, it would also be useful to also look at the crossover from the type of behaviour we observe to the large-N limit, where, due to localisation, knot type will not affect properties.

Chapter 5

Knotted Polymers in Designed Channels

5.1 Introduction

The simulations in this chapter are motivated by the gel electrophoresis of knotted DNA. We do not, however, consider this system directly but instead look at designed channels, which were introduced to model gel electrophoresis in a particular regime. In subsection 5.1.1, we review previous work on both electrophoresis and designed channels. In subsection 5.1.2, we explain our aims and give an overview of the rest of the chapter.

5.1.1 Background

As already discussed in this thesis, there are a variety of experiments in which the knotting of ring DNA is considered. Examples of the topics of such experiments include analysis of the action of particular enzymes [39], the probability of forming knots after random closure [60] and the steady-state level of knotting in reactions [49]. However the knots may be formed, it is crucial that their type may be identified. One

possibility is to use electron microscopy [24] but this requires the individual examination of each molecule. A much more efficient approach is to use gel electrophoresis [55].

In electrophoresis, (poly-)electrolytes in solution migrate under an external electric field [55]. When electrophoresis is performed in a gel, typically agarose or polyacrylamide, steric interactions allow polyelectrolytes to be separated by properties such as size or rigidity. In particular, linear DNA molecules may be separated by length because chains with different lengths migrate at different average velocities.

There is a regime in which the length-dependence of the migration rate arises from entropic trapping [112]. The gel structure is inhomogenous and has some regions where the molecule is more strongly confined. Therefore, the entropy of the chain depends on its position in the gel. There are barriers for the polymer to move from a position with high entropy to somewhere with low entropy and it may become trapped.

It is well established that DNA rings may be separated by electrophoresis on the basis of their knot type. Sogo *et al.* [24], and then Trigueros *et al.* [113], performed electrophoresis of knotted DNA at two field strengths. At 'weak' fields they found an increase in migration distance with knot complexity. At 'strong' fields Sogo *et al.* found the inverse behaviour, more complex knots migrated more slowly. Trigueros *et al.*, on the other hand, saw non-monotonic behaviour: for knots up to about 5 essential crossings, there was a decrease in migration distance, followed by an increase above 6 essential crossings. The underlying physical mechanisms are not well understood.

An attempt to model the experiments of Sogo *et al.* [24] was made using Monte Carlo simulations [114] with the BFCAF algorithm, which is briefly described in section 3.1. The gel was modelled as a regular array of parallel posts. Since only local moves were applied, chain tension, which may be important in the electrophoresis of DNA rings [115], was neglected. Through a scaling of simulation time based on diffusion coefficients, the weak field behaviour was essentially imposed. It has also been

suggested that some of the behaviour may be due to hydrodynamic interactions [54] but it has been argued that electrophoresis experiments are performed in a regime where these are screened [55].

We do not attempt to model electrophoresis gels directly because their structures are complicated and not well known [55]. Instead, we simulate a simpler experimental system [116, 117] that was designed to mimic the behaviour of gels in the entropic trapping regime. Before describing our motivation, aims and approach in more detail, we first review previous work on this system. To aid visualisation, we depict our simulation model in Fig. 5.1.

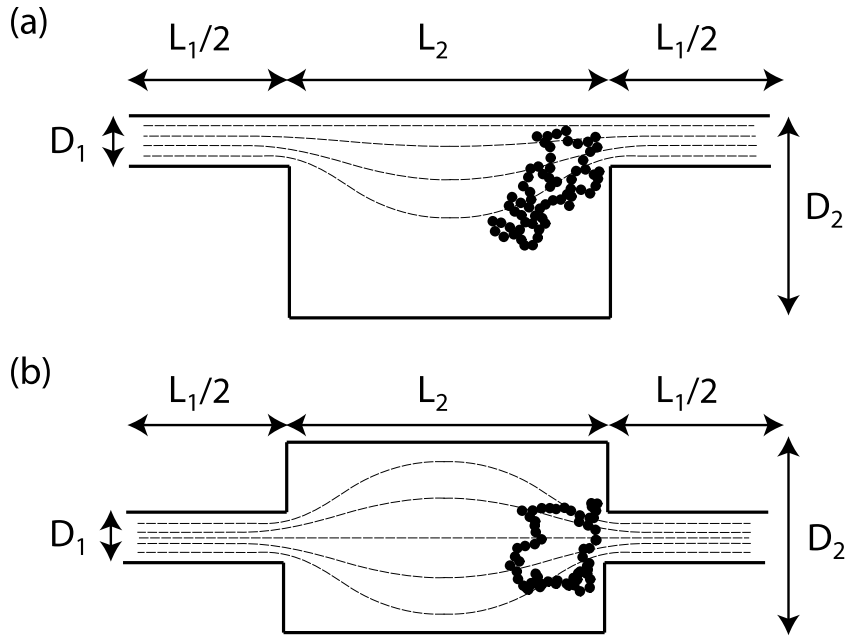


Figure 5.1: The set-up used in the simulations. Dashed lines show electric field lines (illustrative only, not accurate representation of actual fields). Periodic boundaries are applied in the direction of the field and also in the direction out of the page. $L_1 = L_2 = 48\sigma$, $D_2 = 24\sigma$ and for D_1 values in the range $4 - 12\sigma$ are used. (a) The type of channel used experimentally. (b) The channel mainly used in our simulations.

The experiments of Han *et al*. [116, 117] considered linear DNA in periodic microfabricated channels as a simple model for gel electrophoresis in the entropic trapping regime. In each channel repeat there were two regions of different depths. If the

depth of the shallower part is comparable to, or less than, the size of the polymer, then entropic trapping occurs. In the regime where trapping was evident, it was found that longer molecules migrated faster: the barrier may be crossed by a local deformation of the molecule into the shallower region and longer molecules present more potential sites for such deformations. The possibility of such channels being used as efficient devices for the separation of linear DNA by length has also been suggested [117].

Linear DNA in designed channels of the type studied by Han *et al.* [116, 117] was considered theoretically by Sakaue [118]. As the polymer moves from a deeper into a shallower region, it loses entropy and its free energy increases. At the same time it is moving to a lower field potential. The combination of the two gives a free-energy barrier, ΔF – a maximum in the free energy at a certain polymer-centre-of-mass position. Sakaue [118] analysed the transition rate from the deeper into shallower regions by considering the rate of attempts that the polymer makes to cross the free energy barrier and the barrier size. Expressions for both were found using a scaling approach based on the blob picture. Different regimes were identified. There is a low field regime where the barrier is dependent on length because the whole chain must move into the shallower region before the free-energy maximum is reached. There is an intermediate regime, corresponding to the behaviour seen by Han *et al.* [116], where the barrier is independent of length because only a fraction of the chain must move into the shallower region to reach the free-energy peak. Here, as stated before, longer chains migrate faster because they have more nucleation sites for barrier crossing. Finally, there is a high field regime, where trapping does not occur. As field strength is increased, it is predicted that the crossover to this final regime, 'free' migration, should occur at a field strength $E^{(inj)} \sim 1/D_1^2$, where D_1 is the depth of the shallower region and inj stands for 'injection'.

Computational approaches have also been employed to model the experiments

of Han *et al.*; first a Monte Carlo study by Tessier *et al.* [119] and later Langevin Dynamics simulations by Streek *et al.* [80, 120]. Tessier *et al.* briefly considered the effect of topology, comparing unknotted rings to those with trefoil knots, finding that knots generally migrate slower. Streek *et al.* were able to reproduce the qualitative behaviour seen in experiment.

5.1.2 Aims and Overview

The physical mechanisms that underlie the behaviour observed in the gel electrophoresis of knotted DNA [24, 113] are not well understood. The first aim of this chapter, therefore, is to investigate whether entropic trapping could be responsible for the trends seen in the knot-gel electrophoresis results. We approach this by performing simulations of knotted polymers in designed channels, which model gel electrophoresis in the entropic trapping regime. Our second aim is to demonstrate that this simpler, more easily understandable system, could be used for separations of knotted DNA.

We employ the simulation model of Streek *et al.* [80, 120], which reproduced qualitatively the behaviour seen experimentally in micro-channels [116, 117], but consider knotted rather than linear polymers. Given the simplicity of the model, and the complexity of the electrophoresis systems, we do not attempt to map simulation parameters to experiment. Instead, we find the regime in our model where separation according to knot type occurs and then look for qualitative similarities to experiment. These suggest that equivalent physical effects could be responsible for the effects seen in both systems.

In section 5.2, we discuss our chosen model in more detail. In section 5.3, we present our results. First, we look at unknotted polymers as a guide for the parameter choices in simulations with knots. Then, we look at the mobility of knotted polymers. Finally, we attempt to understand the mobility results by considering transition probabilities. We summarise and discuss our findings, and suggest directions

for further research, in section 5.4.

5.2 Model

In the work presented here, the model of Streek *et al.* [80] is employed. This corresponds to using the polymer model with harmonic springs, Eq. (3.1), with the Langevin dynamics model described in section 3.2.1. As discussed by Streek *et al.*, this model neglects hydrodynamic interactions between beads. This is justified since experimentally hydrodynamic interactions will be screened [55]. As Streek *et al.* point out, polymers should experience additional friction when stopped by a wall due to counterion flow: the wall will prevent the chain from moving but not the counterions. It has, however, been argued that, since the equations describing this electro-osmotic flow take the same form as the equations describing the field, this effect will result only in a renormalisation of the field strength [121, 120, 122].

Fig. 5.1 depicts the channel geometry used in the simulations. Fig. 5.1(a), with the shallower section at the top of the channel, corresponds more closely to the type of channel used experimentally [116, 117] and in previous simulation works [119, 80, 120]. However, the behaviour, as described in ref. [118], should not be qualitatively affected by shifting the shallower section to the centre, as in Fig. 5.1(b): the important details are the typical strength of the field and the depths of the deeper and shallower sections. Initial simulations suggest this to be the case.

Monomers are also subject to an additional potential $q\phi(\mathbf{r})$, where q is the charge on one bead. The electric potential, $\phi(\mathbf{r})$, is found by solving the Laplace equation with the boundary conditions that the first derivative in the direction normal to the walls is zero at the walls. The solution is found using finite differences on a grid of size 0.1σ: this is small compared to both the typical size of a section of the chain and the features of the channel and gives a sufficiently fine resolution. During simulation,

the field strength at a given point is found by considering the difference in potential between the nearest grid points.

The interactions between the beads and the walls are taken to be of the same form as the bead-bead interactions. We take a unit of electric field to be $E_0 = k_B T/\sigma |q|$. The electric field strengths, E, that we quote are the potential difference across one repeat of the the channel, divided by the length. Due to the channel geometry, shown in Fig. 5.1, the local field strength at a given point in the channel is not generally equal to E. In the shallower part of the channel, the field lines are concentrated but in the deeper part they spread out. There are regions where the field is relatively weak, away from the part in line with the shallower section and particularly in the corners, see Fig 5.1.

We consider chains of length $N = 200$, with the following knots: $0_1, 3_1, 4_1, ..., 12_1$. If we take the persistence length to be one bead then our polymers are of comparable length to the DNA typically used in electrophoresis experiments. In ref. [113], for example, molecules of about 77 persistence lengths were used. As discussed in section 4.2 a given knot will have a larger effect on shorter polymers.

The simulated chains do not have torsional stiffness. In electrophoresis experiments with closed rings, the DNA is typically nicked using an enzyme to relax any torsional tension [5]. If this were not done then, as discussed in section 1.1, the DNA might form super-coiled configurations, which would significantly affect its properties.

We expect interesting behaviour to arise through the effect of the knots on the translocation of the polymer from the deeper part of the channel to the shallower. To maximise the frequency with which such translocation events occur, we choose a depth for the deeper part of the channel, $D_2 = 24\sigma$, that is relatively small compared to previous studies [80]. By also using the geometry depicted in Fig. 5.1(b), the polymer is kept closer to the opening of the shallow part of the channel. In ref. [80], an effect whereby polymers may become trapped in the corner of the deep part of the

channel was identified. Our choice of geometry and parameters should also minimise this and so simplify the interpretation of results.

We consider channels with shallow sections of depth, $D_1 = 4, 6$ and 12σ: as in the results of Chapter 4 we find strikingly different results for these different cases. The radius of gyration of the chains, averaged whilst the polymer is migrating through the channel, depends on knot type, channel geometry and field strength, but is $\approx 10\sigma$.

We choose the length of both the deep part, L_2, and of the shallow part, L_1, to be 48σ. We performed a trial run for an unknotted ring with $D_1 = 4\sigma$ at $E = 0.024E_0$, the highest field employed for simulations considering the effect of knot type. These parameters are the choice for which the largest polymer extensions would be expected. The largest separation between any two beads in the direction of the field, seen at any instant during the trial run, was about 45σ, showing that the lengths are sufficient that the polymer will not explore two 'different' deep sections at the same time.

Polymers are initialised in the centre of the deeper part of the channel and then equilibrated for $10^5 t_0$ without the field and subsequently for $10^5 t_0$ with the field. This time is much longer than the relaxation of such polymers as shown, for example, in Chapter 4. Data is then recorded for $2 \times 10^6 t_0$. The reported results are typically averaged over 10 such runs, sometimes more for weaker fields.

5.3 Results

5.3.1 Mobility of Unknotted Polymers

We begin by presenting, in Fig. 5.2, results for the displacement of the centre of mass of an unknotted polymer against time for three individual runs with $D_1 = 4\sigma$ at $E \times D_1^2 = 0.288E_0\sigma^2$. Fig. 5.2 clearly shows trapping, evident in the periods when the displacement remains approximately constant for extended times. It also shows that, compared to the trapping, the time spent moving through the channel is short.

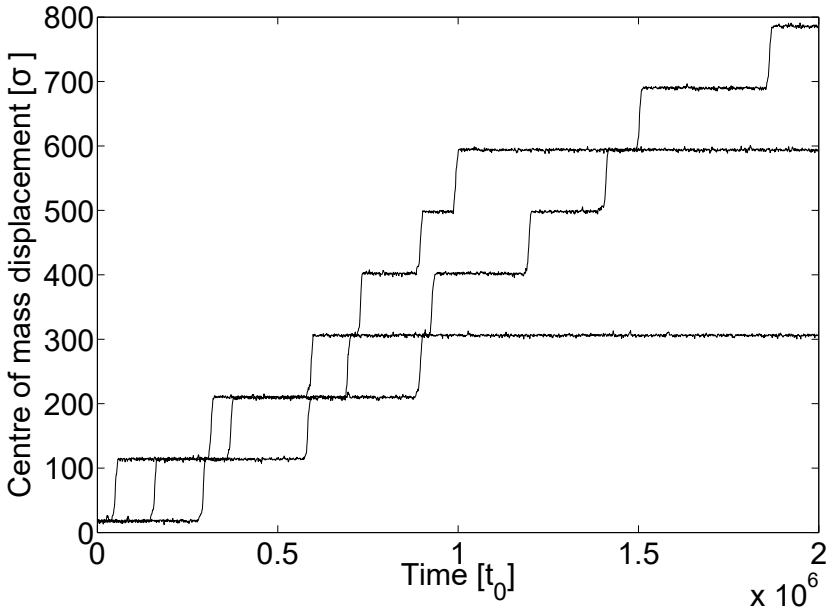


Figure 5.2: Displacement of the centre of mass of an unknotted polymer ring in a designed channel with $D_1 = 4\sigma$ at $E \times D_1^2 = 0.288 E_0 \sigma^2$. The three lines each show the results for individual runs.

We next consider the mobility of unknotted ring polymers, $\mu = \langle v \rangle / E$, where $\langle v \rangle$ is the average migration velocity of the polymer through the channel, as a function of the field strength, E. We expect that as E is increased the behaviour will change from a regime where the polymer does not migrate between subsequent wells (or does so only very rarely), through a crossover where it does migrate but spends time trapped in the wells, to a regime where it migrates without trapping. As mentioned in section 5.1, in ref. [118] it is predicted that the crossover to 'free' migration should occur at a field strength, $E^{(inj)} \sim 1/D^2$.

Results are plotted in Fig. 5.3. The E values on the x-axis are multiplied by D_1^2: the curves for different D_1 are quite close, suggesting reasonable agreement with the predictions of ref. [118]. μ is plotted as a ratio to μ_0, the mobility that would be observed for a polymer in a uniform channel with the same potential difference across it. Eventually, for extremely high fields it would be expected that $\mu/\mu_0 \to 1$. In the range of fields considered, this is not the case. Similar results were found

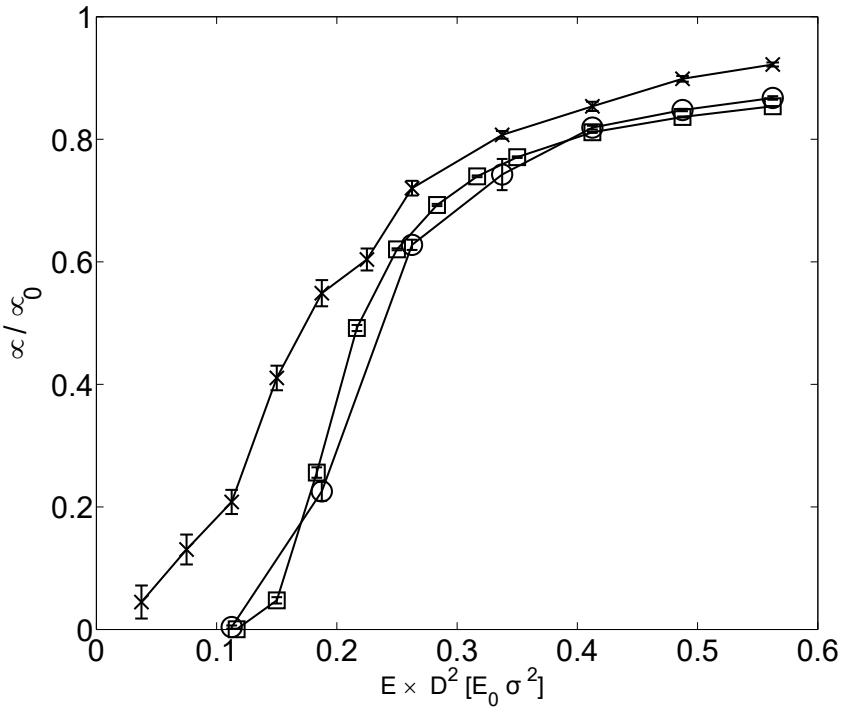


Figure 5.3: Mobility of an unknotted polymer ring in a designed channel as a function of field strength for different shallower channel depths: $D_1 = 12\sigma$ ($\times$), $D_1 = 6\sigma$ ($\bigcirc$) and $D_1 = 4\sigma$ ($\square$).

in ref. [80]: although the field may be high enough that there is no barrier to the polymer migrating, it will explore regions of the wells where the field is relatively weak, reducing its overall mobility. This also explains why the mobility at high $E \times D_1^2$ is lower for shallower channels: for them the relative size of the region away from the central part, where the field is lower, is larger.

5.3.2 Mobility of Knotted Polymers

We expect interesting behaviour for knotted polymers to occur around the crossover in Fig. 5.3. We thus pick a single field strength for each D_1 such that $E \times D_1^2 = 0.288 E_0 \sigma^2$. This corresponds to a mobility of about $0.7\mu_0$ for an unknotted ring, see Fig. 5.3. In Fig. 5.4, we plot the mobility as a function of the essential crossings of the

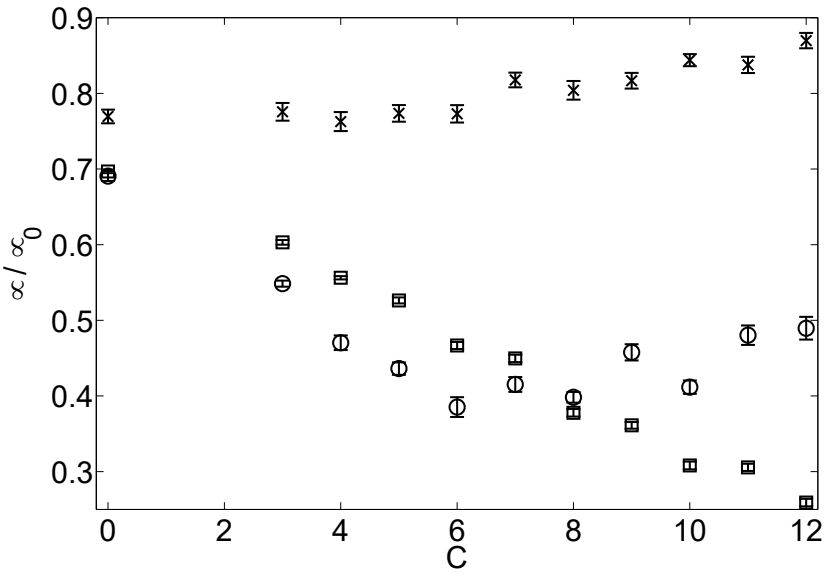


Figure 5.4: Mobility of ring polymers with different knot types, indicated by essential crossings, C, at $E \times D_1^2 = 0.288 E_0 \sigma^2$ for $D_1 = 12\sigma$ ($\times$), $D_1 = 6\sigma$ ($\bigcirc$) and $D_1 = 4\sigma$ ($\square$).

knot, C. For $D_1 = 12\sigma$, the mobility increases slightly with C and, for $D_1 = 4\sigma$, it decreases. For $D_1 = 6\sigma$, non-monotonic behaviour is seen: there is a clear minimum in the mobility at about $C = 6$. The dependence of the trends, as a function of C, on D_1 is reminiscent of results from Chapter 4, where the confinement of knotted polymers in slits is considered.

This qualitative behaviour, the mobility trends for different D_1, appears to be typical for fields at the crossover. In Fig. 5.5, we consider a lower field strength, $E \times D_1^2 = 0.232 E_0 \sigma^2$, and, in Fig. 5.6, a higher one, $E \times D_1^2 = 0.384 E_0 \sigma^2$. Note that the range on the y-axis changes between Figs. 5.4, 5.5 and 5.6. The three figures suggest that the effect of knots on mobility is more pronounced for lower fields. However, if the field is too low, as for $D_1 = 4\sigma$ in Fig. 5.5, and the mobility becomes too small, some knots may show very similar migration: if the field is such that a knot of a certain complexity does not migrate then knots of higher complexity will not migrate either and there will be no separation. A similar effect is seen for $D_1 = 12\sigma$

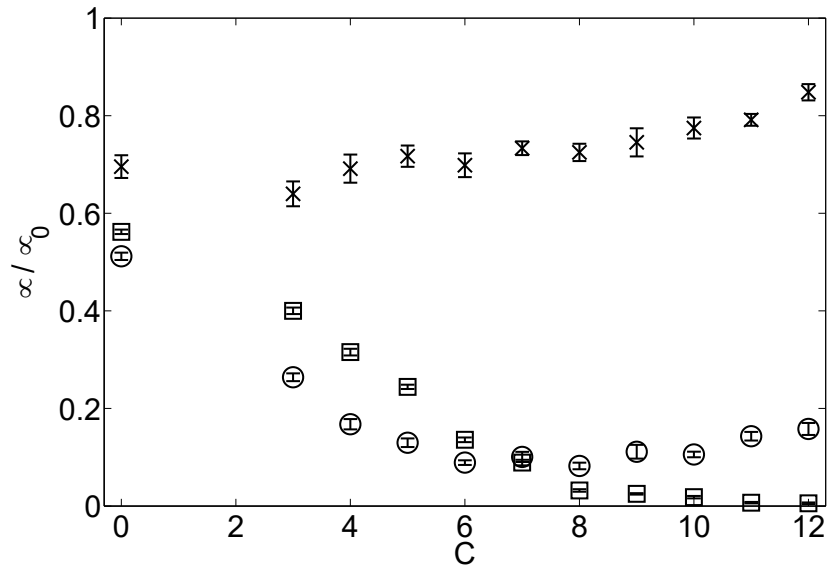


Figure 5.5: Mobility of ring polymers with different knot types, indicated by essential crossings, C, at $E \times D_1^2 = 0.232 E_0 \sigma^2$ for $D_1 = 12\sigma$ ($\times$), $D_1 = 6\sigma$ ($\bigcirc$) and $D_1 = 4\sigma$ ($\square$).

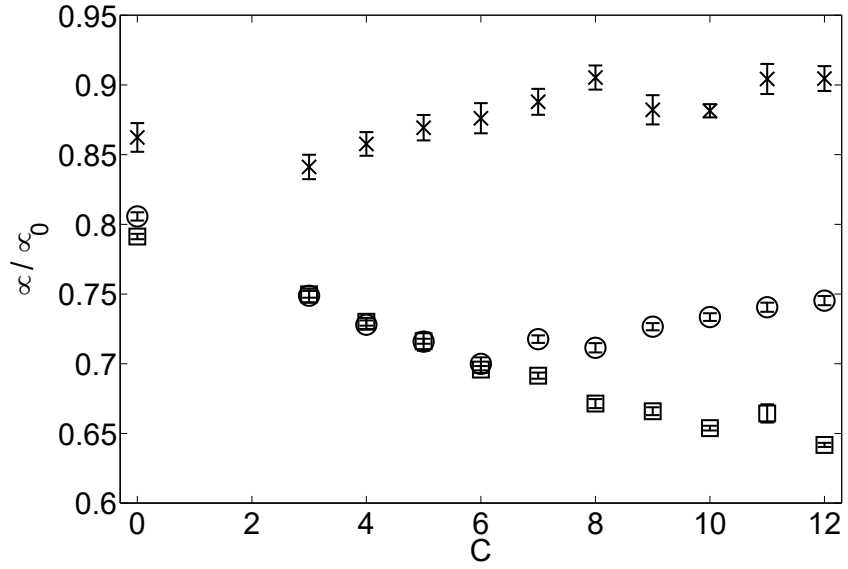


Figure 5.6: Mobility of ring polymers with different knot types, indicated by essential crossings, C, at $E \times D_1^2 = 0.384 E_0 \sigma^2$ for $D_1 = 12\sigma$ ($\times$), $D_1 = 6\sigma$ ($\bigcirc$) and $D_1 = 4\sigma$ ($\square$).

in Fig. 5.6 – between the most complex knots there is little change because the field is too high. Although we do not attempt it here, it appears that, for $D_1 = 4\sigma$ and $D_1 = 6\sigma$, it should be possible to find a value of E that gives an optimal separation of the different knot types. This could be important if such devices were used as a practical method for identifying knots.

5.3.3 Attempt Frequency and Transition Probability

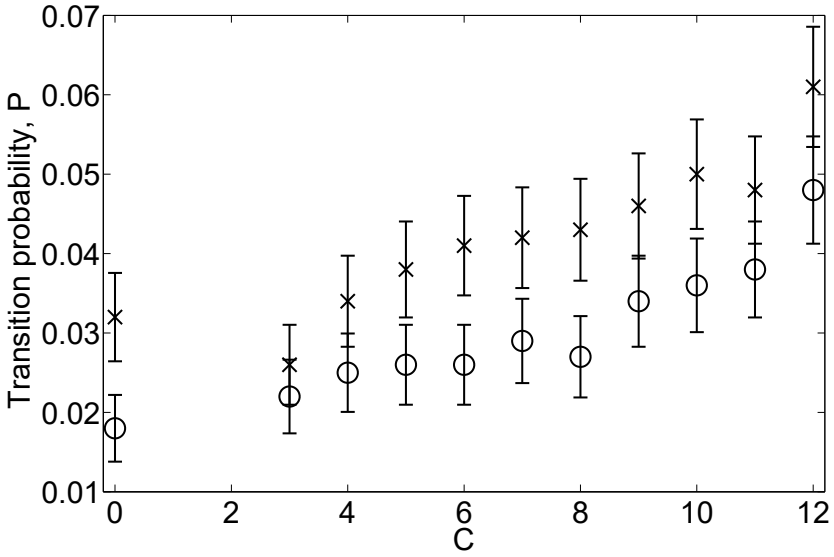


Figure 5.7: Transition probability of ring polymers with different knot types, indicated by essential crossings, C, at $E \times D_1^2 = 0.288 E_0 \sigma^2$ for $D_1 = 12\sigma$. Results for equilibration with ($\times$) and without ($\bigcirc$) the field are plotted.

We concentrate on the results for $E \times D_1^2 = 0.288 E_0 \sigma^2$, shown in Fig. 5.4. We assume that the differences in mobility between polymers with different knot types arise from the transition rate of the polymer from the deeper to the shallower part of the channel: in simulations with uniform channels all knots are seen to have the same mobility. Our assumption is also supported by Fig. 5.2, which shows that the time spent moving through the channel is relatively short.

To try to gain some understanding of the underlying mechanism, we use the picture

put forward by Sakaue in ref. [118] and assume that the transition rate is given by *attempt frequency* $\times$ *transition probability* ($f \times P$). f depends on how much of the polymer lies adjacent to the opening of the shallow section and is affected by polymer length and also whether the polymer in the well is significantly deformed by the field. P is of the form $e^{-\Delta F/k_B T}$, where ΔF is the free energy barrier that must be overcome.

We wish to discover whether it is f or P that gives rise to the changes in mobility seen. We first focus on P. To measure the probability of an 'attempt' being successful, we must define what an 'attempt' is. There is no obvious way that this should be done, so we use the following sensible protocol to measure P for a single 'attempt': the polymer is equilibrated with one bead tethered to a point 2σ into the shallow part of the channel using the same spring as in the polymer. A wall across the channel prevents other parts of the polymer exploring further into the shallow part. By adopting this protocol, we are defining an 'attempt' as starting when the polymer is extended into the shallow part of the channel but at no point by more than 2σ. For our purpose of determining whether f or P dominates the behaviour, the exact definition of an 'attempt' is not crucial.

After equilibration, the tether and wall are removed. If, at any subsequent time, no bead is within the shallow section then the 'attempt' is recorded as having failed. If the centre of mass of the polymer passes the halfway point to the next well, then the 'attempt' is recorded as having been successful. P is calculated as the fraction of 'attempts' that are successful. For $D_1 = 4\sigma$ and 6σ, 300 repeats were performed, whilst for $D_1 = 12\sigma$, 1000 were performed. We consider both the case where the field is applied during equilibration and the case where it is not. Results are plotted in Figs. 5.7, 5.8 and 5.9.

Looking first at the results for equilibration with the field, we note that the same general trends as for the mobility are observed: for $D_1 = 12\sigma$, P tends to increase

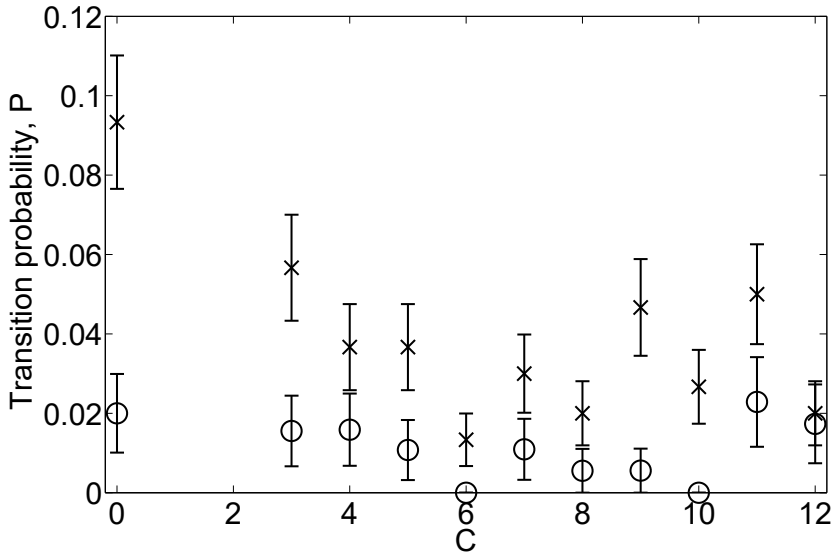


Figure 5.8: Transition probability of ring polymers with different knot types, indicated by essential crossings, C, at $E \times D_1^2 = 0.288 E_0 \sigma^2$ for $D_1 = 6\sigma$. Results for equilibration with ($\times$) and without ($\bigcirc$) the field are plotted.

with C, for $D_1 = 4\sigma$, it tends to decrease and, for $D_1 = 6\sigma$, there is a minimum at $C = 6$.

Interestingly, the results for $D_1 = 4\sigma$ and 6σ show very large differences between equilibration with and without the field: for the case without the field, P shows no clear trend as a function of C. It appears that the topology of the polymer, in other words the polymer as whole, is not very important. This may be because many 'attempts' fail due to local fluctuations of the polymer. For $D_1 = 12\sigma$, in contrast, although results for the two equilibrations are clearly not the same, they are very similar. These comparisons suggest that, for $D_1 = 4\sigma$ and 6σ, the parameters are in the regime where the field is strong enough to significantly deform the polymer in the well, whilst for $D_1 = 12\sigma$, they are on the edge of this regime [118].

The similarity in the trends suggests that the changes in the mobility may be explained by the effect of the knot topology on P. It may, however, be the case that the topology also changes f. To assess whether this is true, we use a simple

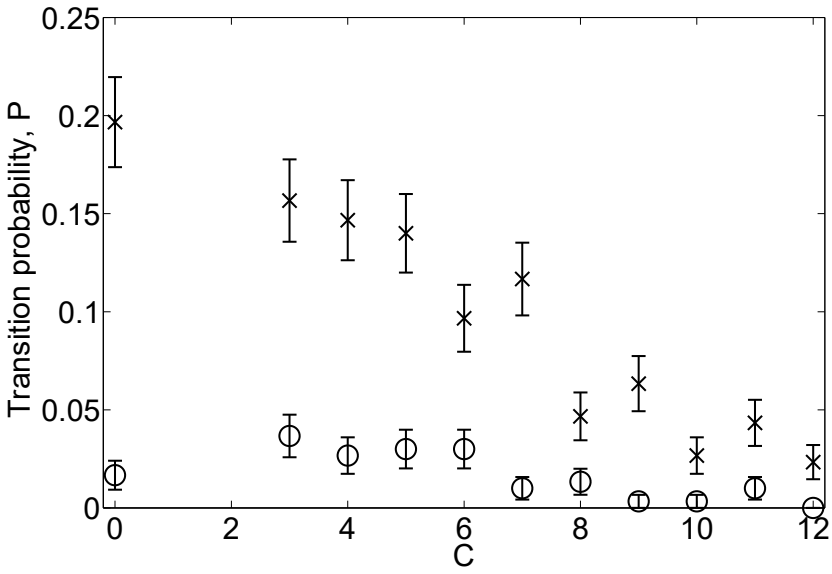


Figure 5.9: Transition probability of ring polymers with different knot types, indicated by essential crossings, C, at $E \times D_1^2 = 0.288 E_0 \sigma^2$ for $D_1 = 4\sigma$. Results for equilibration with ($\times$) and without ($\bigcirc$) the field are plotted.

approximation to estimate f from the results already presented. We say that the average time for the polymer to traverse one repeat of the system, $L/\langle v \rangle$, where L is the system length, will be the sum of the average time spent attempting to move from the well into the shallow part of the channel, $1/fP$, and the time taken to migrate through the system, which we approximate as $L/\mu_0 E$. As discussed earlier, the field experienced by the polymer during its migration will not generally always be equal to E (defined as the potential difference across the channel divided by its length). However, given that, as shown in Fig. 5.2, the time spent migrating through the channel is small compared to that spent trapped, its exact value will not be crucial. For *attempt frequency* we obtain

$$f = \frac{1}{LP\left(1/\langle v \rangle - 1/\mu_0 E\right)}, \tag{5.1}$$

where P is the transition probability obtained in simulations with the field applied

during equilibration. It should be noted that this is the frequency of attempts whilst the polymer is *at* the entrance to the shallower part of the channel.

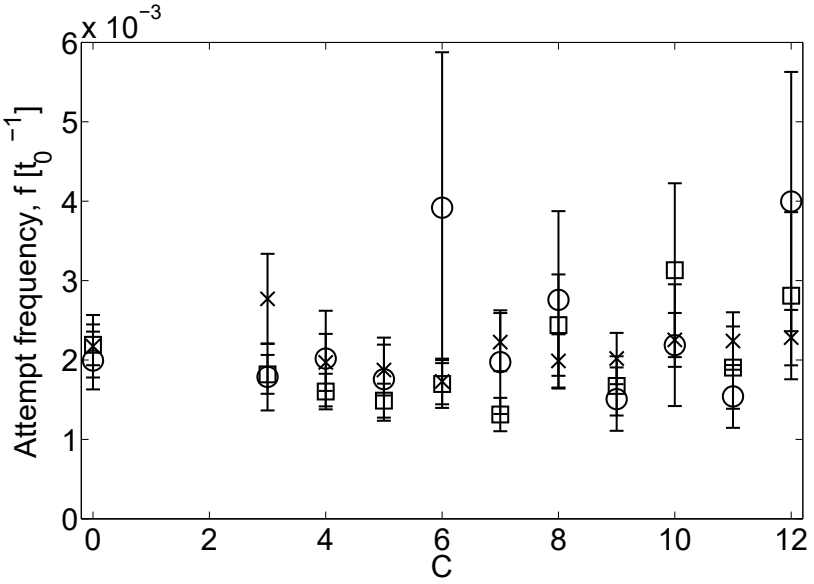


Figure 5.10: Attempt frequency, calculated using Eq. (5.1) for ring polymers with different knot types, indicated by essential crossings, C, at $E \times D_1^2 = 0.288 E_0 \sigma^2$ for $D_1 = 12\sigma$ ($\times$), $D_1 = 6\sigma$ ($\bigcirc$) and $D_1 = 4\sigma$ ($\square$).

The resulting f are plotted in Fig. 5.10 as a function of C. Although there is some spread and relatively large errors for some points, the results are consistent with f being approximately the same for all knot types: the evidence of our results suggests that the changes in mobility are dominated by the effect of knot topology on P, the transition probability.

5.3.4 Free Energy Barrier

As previously mentioned, the transition probability is proportional to $e^{-\Delta F/k_B T}$, where ΔF is the free energy barrier that must be overcome as the polymer moves into the shallower section [118]. To get a very rough estimate of ΔF, we consider the free energy difference between a polymer confined in a channel with the depth of the deep section and a polymer in a channel with the depth of the shallow section. This

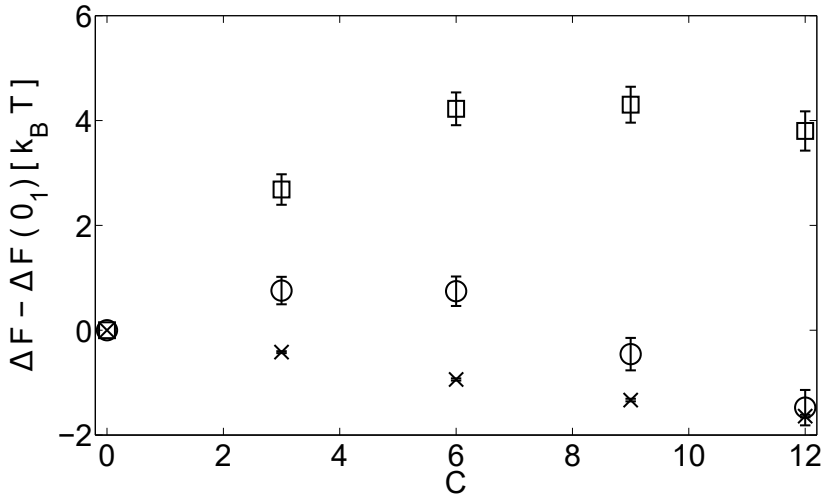


Figure 5.11: Free energy difference, ΔF, for ring polymers with different knot types, indicated by essential crossings, C, between confinement in a channel of depth $D_1 = 24\sigma$ and $D_1 = 12\sigma$ ($\times$), $D_1 = 6\sigma$ ($\bigcirc$) or $D_1 = 4\sigma$ ($\square$). ΔF for an unknotted ring is subtracted to ease comparison of the results for different D_1.

entirely neglects the field and so the estimates are not accurate but are interesting nonetheless, in that they give some feel for whether our conclusion is plausible.

We perform simulations similar to those in Chapter 4 to measure the average force exerted by polymers with different knot types on the walls of channels with a range of depths, D_1. We estimate the value of ΔF from the force-D_1 curves by integrating using Simpson's rule [123]. The error in an integral of a function g from a to b approximated by Simpson's rule using strips of width h may be estimated as $\frac{b-a}{180} h^4 \langle g'''' \rangle$, where $\langle g'''' \rangle$ is the average of the fourth derivative of g over the interval [123]. We estimate g'''' using finite differences.

The results are plotted in Fig. 5.11. There are some similarities to the ΔF that would be expected from the results for P (see Figs. 5.7, 5.8 and 5.9): ΔF decreases with C for $D = 12\sigma$ and has a maximum at about $C = 6$ for $D_1 = 6\sigma$. For $D_1 = 4\sigma$, the values do initially increase with C but then also reach a maximum. See Chapter 4 for a discussion of why such trends are found.

Although there are qualitative similarities, if relative transition probabilities from

the results are calculated using $P \propto e^{-\Delta F/k_B T}$, they are quantitatively quite different to the ratios between the data points in Figs. 5.7, 5.8 and 5.9: as expected, the estimates of ΔF are significantly different to those that would be inferred from the migration simulations. However, the basic trends suggest that our conclusion, that it is the effect of knot topology on the transition probability that leads to the behaviour observed, is plausible.

5.4 Summary and Discussion

To summarise, we have demonstrated that polymers in designed channels may migrate with quite different mobility depending on their knot type. This suggests that channels of the type made experimentally by Han *et al.* [116, 117] could be used to separate knotted DNA molecules. Generally, bigger differences in mobility were seen for lower fields, although they must be sufficiently high that all knots migrate. Evidence was found that the observed changes in mobility arise from the effect of knot type on the transition probability for the polymer to move into the shallower part of the channel. Depending on the depth of the shallower section, different trends in the mobility were observed. These are reminiscent of results observed in electrophoresis experiments with knotted DNA [24, 113]: there, mobility increases with knot complexity for 'weak' fields and decreases or shows non-monotonic behaviour for 'strong' fields.

Electrophoresis gels have pores with a range of sizes [55]. It may be that at different field strengths pores of different sizes become traversable for the polymer. Movement through the smallest pore size accessible could become a rate limiting step and determine overall mobility. Thus, at larger fields, behaviour corresponding to movement through shallower constrictions would be seen. Although the structure of electrophoresis gels is complicated and these remarks are very speculative, the

similarities suggest that entropic trapping could play a role in such experiments. This possibility is worth investigating further.

It could potentially be interesting to explore the parameters in more detail to determine the channel geometry and field that give the best separation of polymers with different knot types. However, whilst ref. [80] demonstrated that the model can qualitatively reproduce experiment, it would be difficult to map *quantitative* values determined from such simulations and so such an exercise might have little practical value.

Experiments, such as those in ref. [113], show that DNA molecules that are covalently closed, and so have torsional tension, migrate differently to those that are nicked. An interesting extension would be to perform similar simulations on rings with a defined twist and torsional stiffness, closed at different linking numbers. To introduce twist, it would be necessary to include additional orientational vectors for the beads: a possible method for doing this would be that proposed by Chirico and Langowski [82].

Chapter 6

Knotted Polymers under Tension

6.1 Introduction

As discussed in Chapter 2, knots occur naturally in biological molecules such as DNA and proteins. The need to understand the dynamics of these molecules raises questions about the dynamics of knotted polymers. Further, there have been experiments in which knots were tied in biopolymers such as actin [63] and linear DNA [32] with optical tweezers. Bao *et al.* [32] measured diffusion coefficients of DNA knots with fluorescence microscopy. The knots were held under tensions in the range 0.1-2 pN. These forces may be similar to those induced *in vivo* by enzymes such as polymerases [124].

Huang and Makarov [125], who applied Langevin Dynamics simulations to explore a wide range of parameter choices, showed that the experiments by Bao *et al.* were in the intermediate 'elastic' regime, where the external force $f > k_BT/l_p$, with l_p being the persistence length [1]. In this regime, the diffusion coefficient varies weakly with tension. At higher tension there is a 'tight knot' regime, where $f \gg k_BT/l_p$, and the knot properties are dominated by the details of monomer-monomer interactions. For low tensions, $f \ll k_BT/l_p$, there is a 'blob' regime where the knot size fluctuates

widely. Using Brownian dynamics simulations, with parameters matched to the experiments by Bao *et al.*, Vologodskii [126] obtained similar diffusion coefficients. As in the experiments, they increase roughly linearly with knot length. In these studies, polymers were under externally applied tension but it has also been argued that knots could exist in metastable tight states due to entropy alone [127].

Whilst work on knots under tension has tended to focus on diffusion coefficients, for knotted ring polymers other aspects have been investigated. In section 2.4.2, we discussed how knotting ring polymers introduces a new relaxation time-scale. Previous work on knot relaxation has focussed on the 'blob' regime [29, 64, 65, 66, 67].

The experiments on artificially knotted DNA [32], and the ability of enzymes to introduce tension *in vivo* create a need for understanding of the dynamics of knots in the elastic regime. In this chapter, we perform coarse-grained simulations to work towards this aim. As well as considering diffusive motion, we extend previous work in the blob regime by looking at knot relaxation. In both areas, we focus on the effect of the particular topology of the knot rather than just its length.

6.2 Model

We choose to study two knot groups: torus knots and even-twist knots. The first few knots in each group are shown in Fig. 6.1. Knots of higher complexity have more crossings but a similar structure. By focussing on two groups with a topological difference between them, we may gain a clear picture of the effect of topology.

We use the polymer model with FENE springs from Eq. (3.2) coupled to the Stochastic Rotation Dynamics solvent described in section 3.2.3. We use flexible polymers, as we are mainly interested in generic, qualitative effects. For a quantitative comparison to experiments, it would be important to also include a bending potential that captures the semi-flexible nature of DNA, as has been done in previous

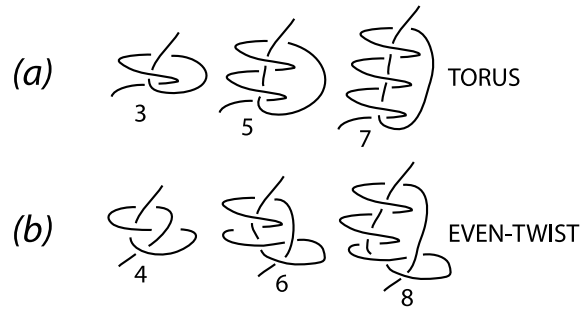


Figure 6.1: (a) The first three torus knots. (b) The first three even-twist knots.

simulations [126, 125]. For example, in the elastic regime that we study, semi-flexibility can lead to knots that extend fewer persistence lengths [32] than those in our simulations. It would be interesting to investigate what difference, if any, this makes to the effects we uncover.

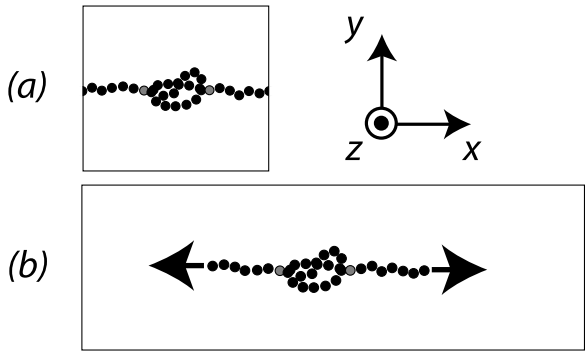


Figure 6.2: The two geometries used in the simulations. In (a) the polymer ends are connected using periodic boundary conditions, forming a ring polymer under tension. In (b), the polymer is linear and the two end beads are subjected to a constant force to provide the tension. Grey circles indicate the beads identified as the first and last beads of the knot by the knot tracking algorithm

To simulate a polymer under tension, two different geometries, illustrated in Fig. 6.2, were considered. In the geometry (a), a simulation box of 32σ by 32σ by 20σ or 21σ was used. The polymer was connected to itself across the periodic boundary. By varying the number of beads in the polymer, the tension can be changed. This approach offers the advantage of no free ends. Simulations may be run as long as

necessary for good statistics, without worrying about unknotting or other end effects. In the geometry (b), a much larger simulation box of 32σ by 32σ by 300σ was used and the polymer ends were not joined. Instead, the first and last beads were subjected to a constant force. Geometry (b) was mainly used to test the reliability of the more efficient geometry (a). Knots were introduced by hand.

In the elastic regime which we consider, crossings of the polymer in the x-y-plane only occur in the knot. So knot-finding algorithms that use knot polynomials, such as the one described in section B.3, are unnecessary. Instead, the first and last beads of a knot, shown in Fig. 6.2, can be identified by finding bond crossings of bead to bead vectors from the projection in the x-y plane. The mid-point between the first and last beads was taken as the knot's position and the difference as its length. Distances were measured along the polymer contour, as in the experiments [32].

6.3 Results

Persistence length may be considered as the length scale on which the polymer behaves like a rigid rod [1]. So, for a flexible polymer, it is reasonable to take $l_p \approx \sigma$, the bead size. We primarily use a tension of $f = 5\frac{k_B T}{\sigma}$, in the elastic regime, as in the experiments of Bao *et al.* [32]. If we were modelling DNA, where $l_p \approx 50nm$, our force would map onto $f \approx 0.4$ pN, which is comparable to ref. [32].

We first investigate the variation of knot length with tension to show where our chosen tension lies on such a curve. Fig. 6.3 shows that the length of the 3_1 knot decreases with tension and plateaus at higher tension, consistent with ref [125]. A tension of $5\frac{k_B T}{\sigma}$ lies at the crossover from the region where knot length varies rapidly to the plateau. This behaviour holds for the other knots we investigate too.

In Table 6.1, we compare the average length of different knots for polymers under a tension of $f = 5\frac{k_B T}{\sigma}$. The knot length increases approximately linearly with the

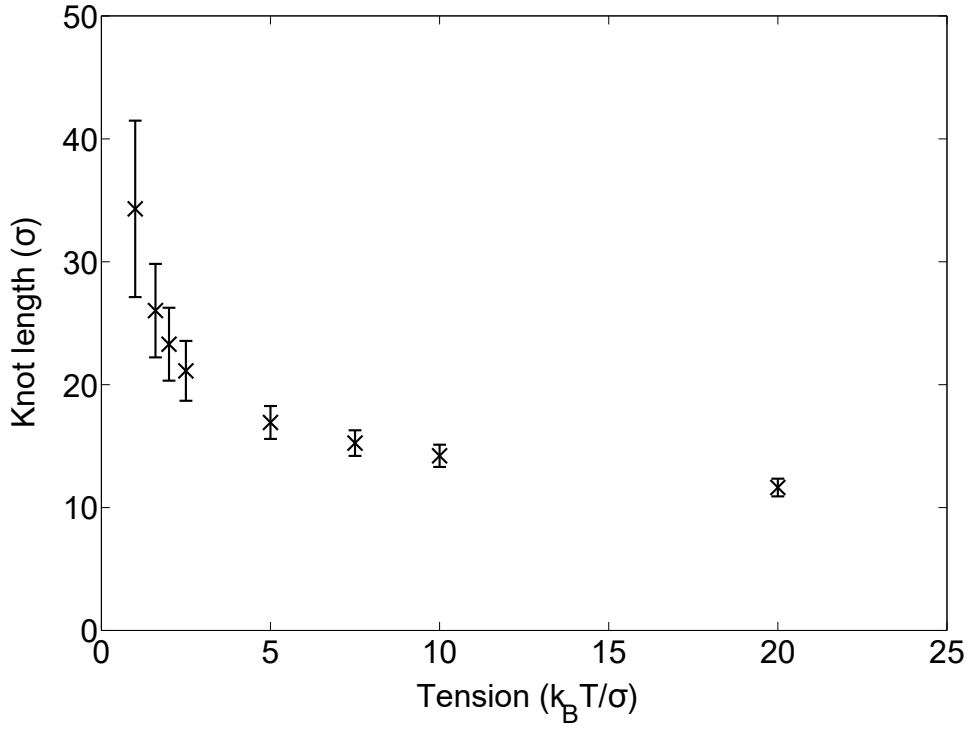


Figure 6.3: Average knot length for the 3_1 knot on a polymer under tension. Simulations were performed using geometry (b).

Table 6.1: Average knot length for linear polymers under a tension of $5\frac{k_BT}{\sigma}$ for geometries (a) and (b).

Knot type	Length in (b) geometry(σ)	Length in (a) geometry(σ)
3_1	17 ± 1	17 ± 1
4_1	24 ± 2	24 ± 1
5_1	28 ± 2	29 ± 2
6_1	35 ± 2	35 ± 2
7_1	39 ± 2	39 ± 2
8_1	46 ± 3	45 ± 2
9_1	49 ± 3	50 ± 2
10_1	56 ± 3	57 ± 2
11_1	59 ± 3	59 ± 2
12_1	66 ± 3	67 ± 2

number of essential crossings, an effect we observe at other tensions as well. For geometry (a), it is harder to set tension explicitly. Instead either the number of polymer beads was changed, or the box length was varied between $L = 20\sigma$ and $L = 21\sigma$ (the Stochastic Rotation Dynamics algorithm uses boxes of size σ, which constrains us to integer values). By comparing the knot length to results from geometry (b), see Fig. 6.2, a similar effective tension could be simulated. It was found that it was easier to achieve this that by allowing the box length to vary slightly. We tested that the knot diffusion coefficient only depends very weakly on tension in the range $f = 2 - 8\frac{k_B T}{\sigma}$, as expected for the elastic regime [32, 125].

6.3.1 Diffusive Motion

We begin by studying the diffusive motion of the knots along the chain. In Fig. 6.4, we show the mean square displacement of the torus and even-twist knots as a function of time. At shorter times, we observe sub-diffusive behaviour with $\langle x^2 \rangle \sim \sqrt{t}$, but this crosses over to Fickian ($\langle x^2 \rangle \sim t$) diffusive motion, typically around $t \gtrsim 10^5 t_0$. The resulting diffusion coefficients, extracted from the mean-square displacements at later times, typically $t = 10^5 - 2 \times 10^5 t_0$, are listed in Table 6.2. The diffusion coefficients clearly decrease with increasing crossing number, but for a given complexity, torus knots have larger diffusion coefficients than even-twist knots. We observe a similar topology induced non-monotonic behaviour with crossing number in simulations of knotted polymer ejection from a capsid in Chapter 8.

The diffusion coefficient is calculated by fitting a straight line to the mean-squared displacement curve, $X(t)$, in the chosen range using least-squares regression. To correctly estimate the error, however, we need to determine the number of independent points that the curves provide. To do this we considered the quantity $Y = X(t) - (a + bt)$, where a and b are the coefficients from the fit. We group the points into blocks [74] of time t_b, calculating the average of Y within each, $\bar{Y}_b$.

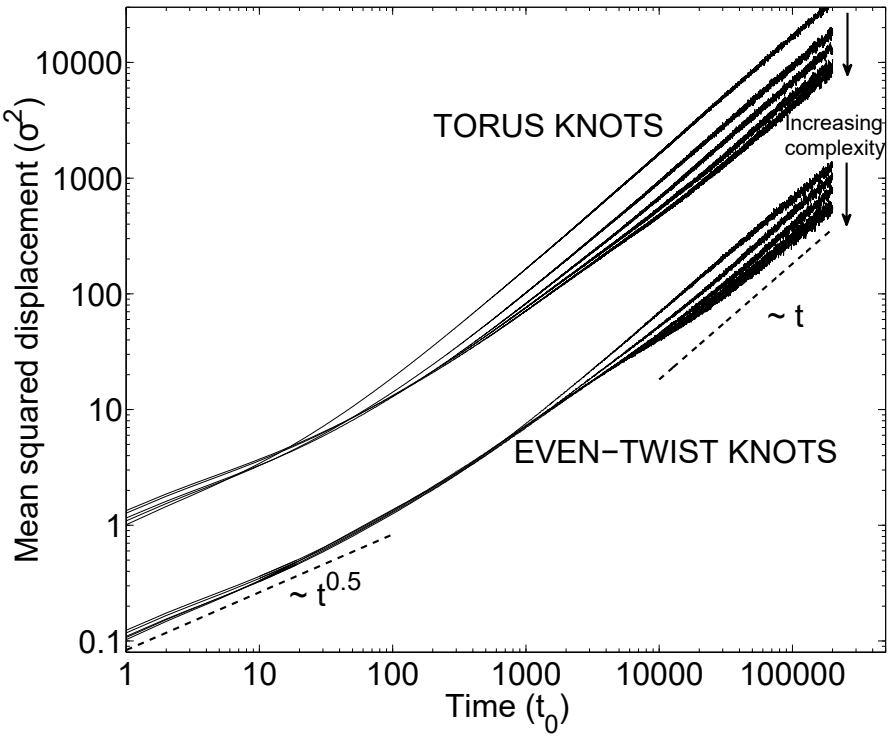


Figure 6.4: Mean squared displacement curves plotted on log-log scales. The upper lines are for the torus knots and have been displaced on the vertical axis by a factor of 10. The lower lines are the even-twist knots. Within each group knot complexity increases from top to bottom (at long times). The dashed lines have slopes of 0.5 and 1.

We plot the quantity $\sigma^2(\bar{Y}_b)t_b$, where σ^2 is the variance, as a function of t_b. Once t_b is sufficiently long that the points are not correlated this quantity should tend to a constant (from which an estimate of the correlation time may be extracted by dividing by $\sigma^2(Y)$). As a conservative estimate we took the time between independent points to be $8 \times 10^3 t_0$. A similar analysis was performed to look at errors in the measured knot-length auto-correlation decay time-scales, which are discussed later.

The diffusion coefficient can be related to the friction coefficient through the Einstein relation $\xi = k_B T/D$. We show results for friction vs. knot length in Fig. 6.5. Both knot groups show the same linear dependence on length, with the same slope, but there is a constant shift between them. A very similar linear dependence of the

Table 6.2: Relaxation time-scales and diffusion coefficients for knots in a polymer under tension. time-scales were found by an exponential fit to the autocorrelation decay between 0.5 and 0.05, see Fig. 6.6.

Knot type	Relaxation Time-scale ($\times 10^3 t_0$)	Diffusion coefficient ($\times 10^{-3} \frac{\sigma^2}{t_0}$)
3_1	0.020 ± 0.001	8.0 ± 0.4
4_1	0.029 ± 0.001	3.1 ± 0.2
5_1	2.1 ± 0.1	4.5 ± 0.3
6_1	1.2 ± 0.1	2.5 ± 0.2
7_1	2.5 ± 0.1	3.4 ± 0.2
8_1	1.4 ± 0.1	2.0 ± 0.1
9_1	3.5 ± 0.1	2.3 ± 0.2
10_1	1.9 ± 0.1	1.4 ± 0.1
11_1	5.2 ± 0.1	2.1 ± 0.1
12_1	2.1 ± 0.1	1.3 ± 0.1

friction on length was measured in experiments [32], as well as in simulations [125]. In both cases, the only even-twist knot measured was 4_1, and the friction was consistently higher than that expected from torus knots. We also plot a simple approximation to the friction, $\zeta_0 \times$ the average knot length, where ζ_0 is the friction coefficient of a monomer in the Stochastic Rotation Dynamics solvent. This simple approximation provides a good estimate of the slope of the friction vs. knot length curve in this tension regime, as also seen in ref. [125].

For unknotted polymers, neglecting the hydrodynamic interactions leads to a linear dependence of the diffusion coefficient for centre of mass motion on the number of beads, but taking the hydrodynamics into account changes the scaling substantially. The scaling with hydrodynamic interactions may be calculated using the Zimm approximation [1]. The methods used in refs. [126, 125] neglect hydrodynamic interactions, but the simulation technique we use here can reproduce the correct Zimm scaling for linear polymers [128, 96]. Removing hydrodynamic interactions *quantitatively* reduces the magnitude of the knot diffusion coefficients by about a factor of 1.5 but does not appear to alter their *qualitative* scaling with knot length. Simulations

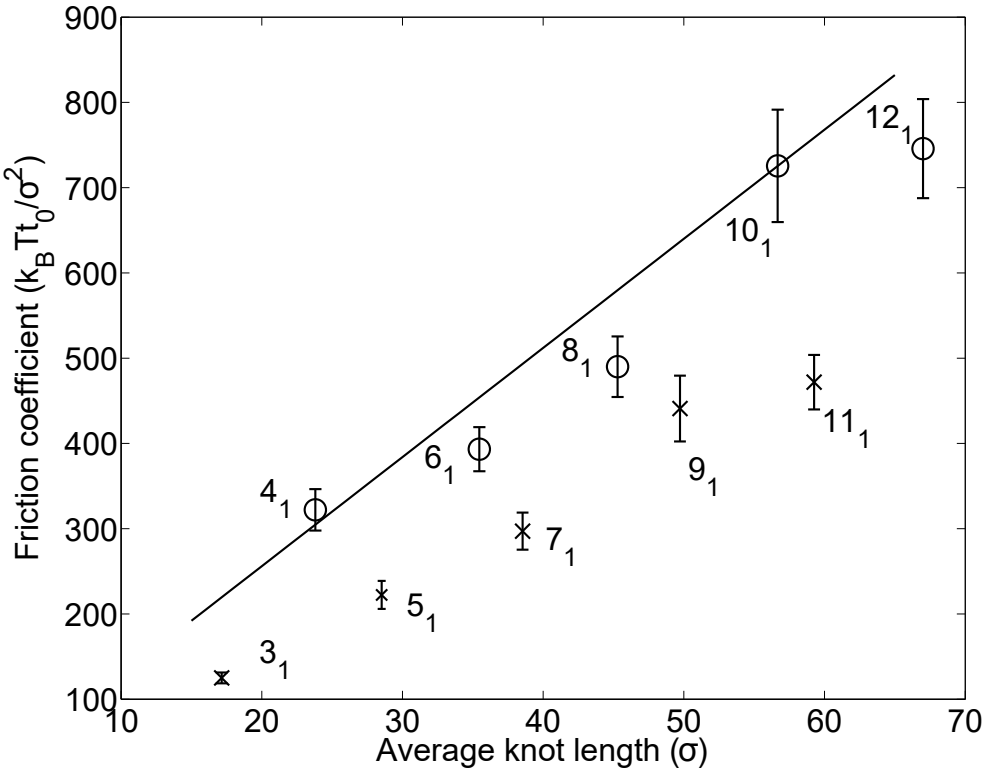


Figure 6.5: Friction coefficient against average knot length for torus knots (crosses) and even-twist knots (circles). The solid line is $\zeta_0 \times$average knot length, where ζ_0 is the friction coefficient of a monomer in the SRD solvent (each bead contributes a length of σ.)

without hydrodynamic interactions were performed by randomly interchanging the velocities of solvent particles after every collision.

The difference in friction between torus and even-twist knots can be linked to an important topological distinction. As knots diffuse along the chain, they must reptate through themselves [32]. From Fig. 6.1, one can appreciate that the polymer may pass relatively smoothly through a torus knot, always curving in the same sense. For an even-twist knot, however, the twist at one end introduces a sharp inversion of the direction in which the polymer is curving, making the polymer passage less smooth and increasing the effective friction. Since this inversion occurs only once in an even-twist knot, it may explain why the frictions are higher than those of the torus knots

by an additive constant.

Evidence that the main mode of knot diffusion in this regime is through reptation can be found in the mean-square displacement data in Fig. 6.4. At short times the motion is sub-diffusive because as the polymer in the knot tries to move it tends to be bounced back by other sections of the knot. At longer times, when the polymer contour has relaxed within the constraints formed by the knot, we observe ordinary Fickian diffusion. This crossover corresponds to two regimes in the reptation model [1], where the mean squared displacement of the polymer *along its own contour* increases with the exponents we observe.

The mapping of dynamics from coarse-grained simulation units to physical units is always subtle [100]. In the experiments of ref. [32], $D \approx 1.25\mu m^2/s$ for a 3_1 knot. Comparing to our simulated value for the same knot, and assuming $l_p \approx \sigma$ gives a mapping of $t_0 \approx 16\mu s$. Very similar values for t_0 are found when using the other knots to do the mapping. This suggests that sub-diffusive $\langle x^2 \rangle \sim \sqrt{t}$ behaviour should persist up to a time-scales of order ms, with the full crossover to Fickian diffusion occurring at time scales on the order of s. These time-scales correspond qualitatively to the experiments of ref. [32].

6.3.2 Knot Length Relaxation

We next investigate the fluctuations and dynamic modes of the diffusing polymer knot under tension. Orlandini *et al* [65] showed that the long time-scale originally observed in the radius of gyration autocorrelation function in the 'blob' regime [29] can also be observed in the decay of the knot-length autocorrelation function $\frac{<l(t)l(0)>-<l(0)><l(0)>}{<l(0)l(0)>-<l(0)><l(0)>}$, where $l(t)$ is the length of the knot at a given time. We investigated the same autocorrelation function for knots under tension, and plot the results in Fig. 6.6. The decay of the knot-length autocorrelation function is approximately exponential, and the associated time-scale (the inverse of the slope of the lines) of this exponential

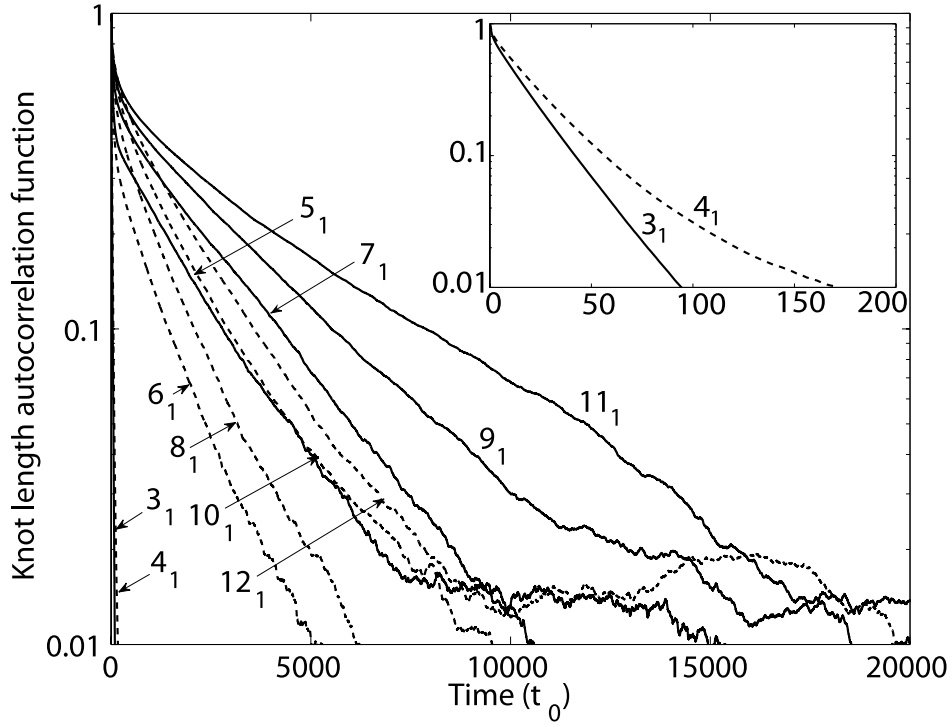


Figure 6.6: Decay of the knot-length autocorrelation with time. Results for torus knots are plotted using solid lines and for even-twist knots using dashed lines. The inset shows 3_1 and 4_1 results on a different scale.

decay depends on the knot type, see Table 6.2. The time-scale increases with knot complexity and is also significantly longer for torus knots than for even-twist knots of similar complexity. There is a remarkably large jump (a factor of about 100) in the decay time-scale between the most simple knots (3_1 and 4_1) and the more complex knots (5_1 and larger). Preliminary investigations of polymer length, N, dependence showed that the time-scales for the more complex knots vary weakly with N, whereas the 3_1 and 4_1 time-scales are more sensitive to N.

To identify the source of the slow decay of the knot-length autocorrelation function, the knot configurations were more closely investigated. Two different modes were identified: a spiral-flipping mode and a breathing mode, both depicted in Fig. 6.7(a).

The spiral-flipping mode involves switching between a state where the strand

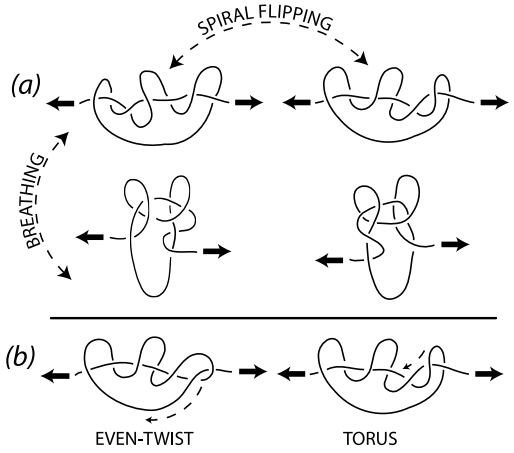


Figure 6.7: (a) Examples of knot modes (for 7_1). Arrows indicate the direction of the tension force. The change between the left and right involves inversion of the spiral – the spiral-flipping mode. The change between top and bottom involves switching the alignment of the spiral with respect to the tension force – the breathing mode. (b) Origin of the faster breathing mode in even-twist knots. Left: in even-twist knots, the end of the spiral, the twist, may slide relatively freely along the strand that passes through it. Right: if the end of the spiral moves in a similar manner in a torus knot it collides with other loops.

entering from the left predominantly curves around the strand entering from the right and vice-versa. The breathing mode involves switching between a state where the axis of the spiral is aligned with the tension force and one where the spiral forms a loop perpendicular to it. To characterise the knot state, two order parameters were used: one for each mode.

For the spiral-flipping mode the sum of angles between successive bonds, in the plane defined by those bonds, multiplied by the displacement from the centre of the knot was taken over all of the beads in the knot. Depending on whether the polymer is more curved towards one end of the knot or the other, this quantity is positive or negative. For the breathing mode the ratio between the maximum distance between any two beads in the knot in the direction of the tension force to the maximum distance perpendicular to the tension force was taken. When the spiral of the knot is aligned with the tension this quantity is larger.

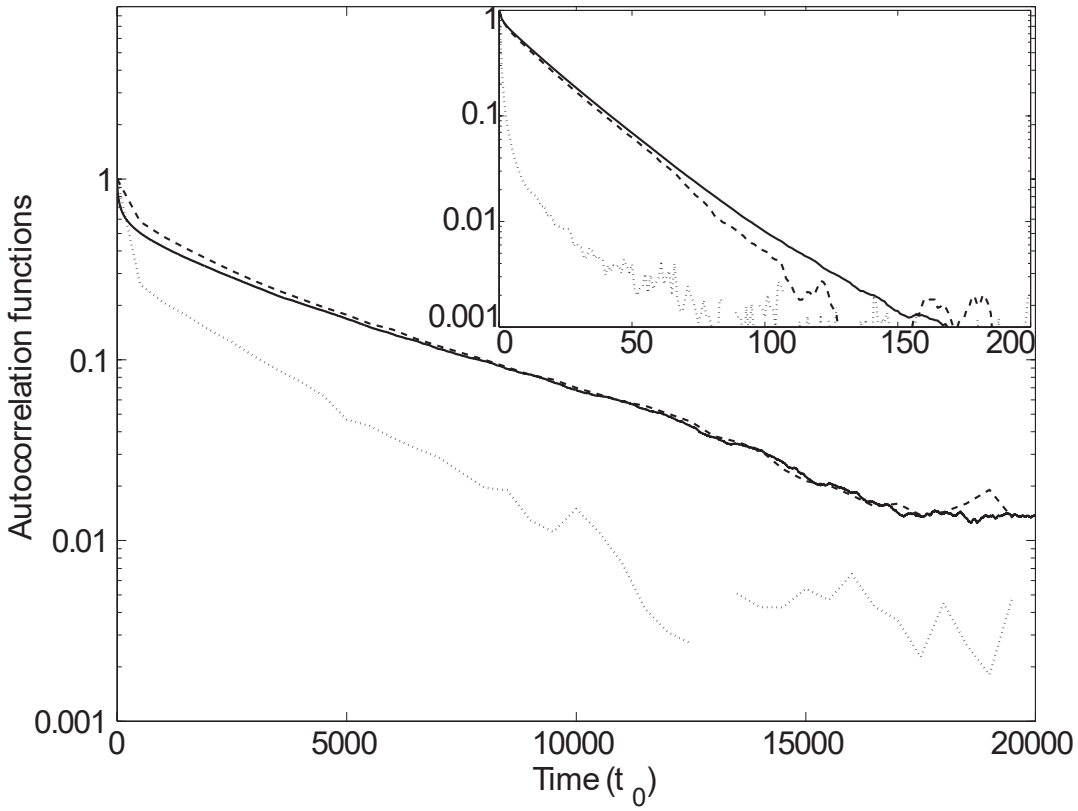


Figure 6.8: Autocorrelation functions for 11_1 for the knot length (solid line), the breathing mode order parameter (dashed line) and the spiral-flipping mode order parameter (dotted line). The inset shows results for 3_1 on a different scale.

We calculated the autocorrelation functions, $\frac{<\phi(t)\phi(0)>-<\phi(0)><\phi(0)>}{<\phi(0)\phi(0)>-<\phi(0)><\phi(0)>}$, where ϕ is the order parameter value, for both order parameters. As an example, the autocorrelation functions for the 3_1 and 11_1 knots are depicted in Fig. 6.8. The breathing autocorrelation function has a very similar decay to the knot-length autocorrelation function, whereas the spiral flipping autocorrelation function decays more rapidly. Nevertheless, both modes show a large jump in time scale between the 3_1 and 4_1 and the more complex knots.

These results suggest that the breathing mode is responsible for the slow decay of the knot-length autocorrelation. The average knot lengths for high and low values of

the breathing mode order parameter support this. The extended configuration has a larger knot length; for the most complex knots a difference of about 3σ is seen.

The coupling to the breathing mode offers an explanation for the large jump in the time-scale between 3_1 and 4_1 and the more complex knots. The spiral of the most simple knots consists of only one loop and so shifting from a configuration which is extended in the tension direction only involves changing its shape. In contrast, for more complex knots, it involves co-ordinated movement of multiple loops. It also offers an explanation for the difference between torus and even-twist knots. As depicted in Fig. 6.7(b), an even-twist knot may deform from being extended by sliding the twist along the strand that passes through it. In a torus knot, the equivalent movement is blocked by the loops of the spiral, so breathing is slower.

Note that there is no big jump in the diffusion coefficients between 3_1 and 4_1 and the more complex knots. While the breathing and spiral-flipping modes may affect the crossover from sub-diffusive to diffusive behaviour (in fact the sub-diffusive range is considerably shorter for the 3_1 and 4_1 knots), they do not appear to determine the long-time diffusive dynamics. Further evidence follows from the fact that the torus knots have slower relaxation but faster diffusion than the even-twist knots.

It is instructive to compare our results for the longest relaxation time-scale to ring polymers without tension in ref. [64]. In contrast with our results, the long time-scale was shown to *decrease* with increasing knot complexity and there was no significant difference between knot groups. This suggests that the dominant modes determining relaxation in the 'blob' regime are not related to the breathing modes we observe for polymers under tension.

By contrast, simulations in ref. [67] that studied the relaxation of initially knotted polymers that are cut (without tension) exhibited a relaxation time-scale that increased with knot complexity, and was longer for torus knots than for even-twist knots. The similarity is perhaps not surprising. For a cut knot to become unentangled

the polymer must move along the contour formed by the erstwhile knot, a process analogous to the self-reptation [32] of knots under tension.

6.3.3 Summary

In summary: we exploited a new boundary condition that minimises end-effects to study the effect of topology on the dynamics of knots in polymers under tension in the 'elastic regime', where the force is strong enough to affect the behaviour of the knot, but not so strong that details of the inter-molecular potentials dominate the behaviour.

The observed motion of the knot, including a sub-diffusive regime of the mean-square displacement at short-times, is consistent with a self-reptation mechanism [32]. To first order, the friction coefficient scales linearly with knot length. Topological differences also play a role. For a similar knot length or complexity, torus knots have a smaller friction (and so a larger diffusion coefficient) than even-twist knots.

Fluctuations and dynamic modes are also affected by knot topology. The longest relaxation mode of the length-length autocorrelation function is dominated by a breathing mode. This topological time-scale increases with knot complexity and is significantly longer for the torus knots than for even-twist knots of similar complexity. These differences can be rationalised by examining knot topology.

6.4 Further Work

Our results have uncovered interesting effects, particularly with regards the relaxation of polymer knots under tension. We expect these to be generic but it would be interesting to simulate semi-flexible polymers that provide a better DNA model. Such simulations could give a more accurate estimate of physical time-scales, and aid experiments to measure them. Another possibility for further study would be to

determine how the relaxation behaviour seen in the elastic regime crosses over to that seen in the blob regime as tension is reduced.

As well as to experiments like those by Bao *et al.* [32], our results are also potentially relevant to knots in DNA in *in vivo* [129]. Particular questions in this area that would be important to address include: what are the magnitudes of the biological forces, and what is the role of macromolecular crowding on knot diffusion and relaxation rates?

Unnicked ring DNA is a polymer with torsional tension and a defined linking number, which can lead to super-coiling. Indeed, *in vivo*, DNA is typically maintained in a super-coiled state. It would be interesting to investigate how torsion and super-coiling affect the diffusion of knots. Do super-coils and knots diffuse separately? Do their interactions lead to new regimes of sub-diffusive behaviour? The effect of torsional stiffness on the modes identified here could also be of interest.

The advent of nanotechnology has brought questions about the diffusion and dynamics modes of knotted polymers in strong confinement to the fore. It would be interesting to extend work that looks at the interplay of confinement and tension [130, 131].

Chapter 7

Knotted Filaments in Shear

7.1 Introduction

In this chapter, we study the dynamics of non-Brownian knotted filaments in shear flow. We build on a long history of work that has demonstrated fascinating dynamical behaviour for a wide variety of objects in shear. We begin this introductory section by reviewing a few examples, before focussing on other recent work, on the equilibrium shapes of knots and on chiral objects in shear, that includes features more specifically related to our chosen system.

In 1922, G. Jeffrey [132] predicted that rigid bodies trace out periodic orbits that depend in detail on their shapes. He analysed the expected periods of rotation and the paths of the orbits. In this chapter, we are concerned with deformable objects [133] and for these even richer behaviour is possible. Red blood cells, for example, change shape with increasing shear rate [134]. Furthermore, the coupling to shear can lead to either unstable tumbling or to a steady state mode where the cells remain at a fixed angle to the flow while their outer membrane rotates like the treading of a tank [97]. A similar crossover to tank treading is predicted for star polymers [135].

For extended linear objects, work has been performed in both the Brownian and

non-Brownian regimes. Experimental advances in single molecule techniques have made it possible to directly observe the stretching and tumbling behaviour of individual DNA molecules [7]. This work inspired a great deal of theoretical research on the way that the polymer flexibility, shear and Brownian noise interact [136]. Several decades earlier it had been shown that filaments in the non-Brownian regime exhibit at least five distinguishable regimes of motion as stiffness, length, and shear rate are varied [11]. These results are still the subject of active investigation by theorists [137]. The crossover between the Brownian and non-Brownian regimes has also been recently considered [138].

Compared to linear objects, knots have more complex properties, for example they may be topologically chiral. Recent work on chiral objects in shear has demonstrated that they migrate in the vorticity direction [139], a hydrodynamic effect that has been recognised for some time [140]. Fascinating experiments by Marcos *et al.* demonstrated it experimentally using helical bacteria [141]. We investigate to determine if this effect is also seen for knots.

A recent investigation by Gallotti and Pierre-Louis [57] considered the equilibrium shapes of stiff knotted filaments. In the limit of strong bending modulus, A, or weak shear rate, $\dot{\gamma}$, our knotted filaments remain in a configuration close to equilibrium and rotate in a manner similar to the rigid bodies considered by Jeffrey [132]. In the opposite limit, with strong shear rate, the filament is deformed and the knot is typically pulled tight. This leads to rich dynamics.

7.1.1 Knot Deformation Number

The focus of this chapter is what happens for relative strong shear forces or for more flexible filaments, the regime where the knots can be tightened by the flow. To estimate where the crossover to this regime occurs we consider the following argument: in the limit of small local bond deformations, the bending energy of a knot of length

L scales as $\sim A/L$, where A is the bending modulus, so there is a force opposing knot tightening $\sim A/L^2$. Neglecting the logarithmic factor [142], the drag on a slender filament in Stokes flow $\sim \eta L$. To tighten the knot, strands which are close to each other must be moved in opposite directions The typical velocity difference will be $\sim \sigma\dot{\gamma}$, where σ is the filament width. Combining this with the drag and comparing to the bending force results in a dimensionless knot deformation number, $\alpha = A/\eta\sigma\dot{\gamma}L^3$. At the crossover, the knot length $\approx$ total filament length, so in calculating α we take L to be total filament length. α resembles the sperm number used with microscopic swimmers [143] but instead of determining when the filament as a whole may be deformed, it indicates when the knot will be tightened. For larger α, we expect the stiff knot regime, but, for lower α, the shear should cause significant deformation.

7.1.2 Summary and Overview

Inspired by the wide variety of previous examples in the literature, we consider knotted filaments as intriguing new object for study in shear flow. The ability of the shear to tighten the knot introduces an interesting aspect not present in other cases. The structure of the chapter is as follows: after introducing a simple model, we present results for it in section 7.3. We then consider an additional aspect of the model that is neglected in the main results. We go on to identify some weaknesses of our model and introduce, and test, a modified bead rotation model in sections 7.5 to 7.7. We check how bead rotation model results for knotted filaments compare to those from our original model, before concluding in section 7.9.

7.2 Model

We apply the coarse-grained bead-spring model [144] with FENE springs, Eq. (3.2) and a bending potential, Eq. (3.5). We update bead positions using the Euler

method [139]:

$$\mathbf{r}_i(t+\Delta t) = \mathbf{r}_i(t) + \left[\mathbf{v}(\mathbf{r}_i) + \sum_j \mathcal{H}_{ij}\cdot\mathbf{f}_j\right]\Delta t, \tag{7.1}$$

where $\mathbf{v}(\mathbf{r}_i)$ is the applied flow, $\mathbf{v} = \dot{\gamma}y\hat{x}$ and $\mathbf{f}_i$ is the force on the i^{th} bead. Assuming zero Reynolds number, the hydrodynamic interactions, $\mathcal{H}_{ij}$, can be approximated by the Rotne-Prager tensor, Eq. (3.9). The natural input units for the simulation are σ (bead size), η (viscosity) and k (spring constant), from which a natural time unit of $t_0 = \sigma\eta/k$ follows. The key parameter that we vary is κ, the bending energy in Eq. (3.5). We used $\dot{\gamma} = (150t_0)^{-1}$, and verified that the stretching of individual bonds relaxes much more quickly than the characteristic time for shear induced motion and so should not influence the dynamics [83].

We simulated single filament rings with one knot, using chains of $N = 50$ beads (unless otherwise stated). We mainly study the left-handed enantiomer of the trefoil knot ($3_1(-)$).

Filaments were given a knotted configuration and then equilibrated for $6\times10^5 t_0$ at finite temperature with no shear to generate random starting points. A $6\times10^6 t_0$ initialisation period was allowed, before data was recorded for $1.5\times10^6 t_0$. The relatively long initialisation was chosen to avoid transients. We ran 50 simulations for most parameter sets. The majority of runs exhibited the same mode of motion throughout the observation time, but for a small number (less than 1%, 1 run at $\alpha = 0.04\times10^{-3}$ and 2 runs at $\alpha = 0.02\times10^{-3}$) of runs a slightly longer initialisation was necessary. The long transients may be caused by the system being close to a parameter value at which a mode appears/disappears [145]. Eq. (7.1) was typically integrated using $\Delta t = 10^{-2}$ although for some parameter choices, for example high κ, it was necessary to reduce this for numerical stability. We checked that using $\Delta t = 10^{-3}$ gave equivalent results.

7.3 Results

7.3.1 Mode Families

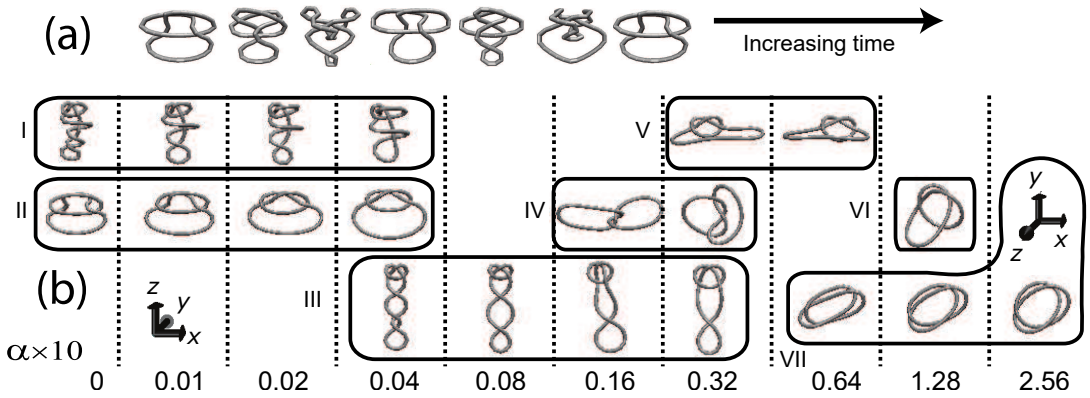


Figure 7.1: Predicted modes of behaviour as a function of the knot deformation number α. x is the flow direction, y is the direction of the shear gradient, and z is the vorticity direction. All configurations are for filaments with a $3_1(-)$ trefoil knot (a) Time series for a filament in a II mode at $\alpha = 0$. Time increases from left to right. The knot rotates clockwise around the z axis. The series spans approximately one period, the time between successive configurations is $1028.7t_0$ and migration is in the $-z$-direction. (b) Example configurations for different mode families over a range of α. Note that the orientation is different for the VII mode. Full animations of the modes are available online [146].

Fig. 7.1 illustrates that lowering α, the knot deformation number, leads to a crossover from knots that remain close to their equilibrium shape, to a regime of surprisingly rich dynamical behaviour where the whole filament exhibits intricate shape oscillations in time (see also the videos accessible online [146]). These orbits may be grouped into a few distinct families comprising very similar types of motion (modes). The seven families the we identify, labelled I-VII, are shown in Fig. 7.1 (b). Some modes show regular, and others chaotic, motion. Different modes show distinct rates and directions of drift along the vorticity axis. A few families are accessible at each α, and the knot typically falls into one type of motion depending on initial conditions. Changing α therefore changes the modes that are accessible, as well as the probability that a certain mode is selected. It should be noted that the results

shown for $\alpha = 0$ correspond specifically to the case where the bending modulus is set to zero: considering instead, for example a very large shear rate would give different results.

The elastic modulus of our bead-spring model $A = \kappa\sigma$ [143], so that the knot deformation number defined earlier takes the form $\alpha = \kappa/\eta\dot{\gamma}L^3$. In Fig. 7.1, we consider 10 different values of κ corresponding to $\alpha = 0 - 2.56 \times 10^{-3}$. For the largest α, the filament remains in braid-like configurations [57] that characterise family VII in Fig. 7.1(b). The motion is composed partly of rotation of the configuration and partly of tank-treading – a particular point moves around the contour. As flexibility is increased (α is lowered) there is a change from modes which rotate in the x-y-plane to modes which have relatively large extensions in the z-direction. Interestingly, a similar shift was seen in experiment with linear filaments [11]. The first family in which the knot is significantly tightened is V.

7.3.2 Identification of Mode Families

Mode families were identified by visual inspection of their motion (see, for example, videos accessible online [146]) and by measuring their drift velocity in the vorticity direction, which distinguished well between different modes. The identity was confirmed by two additional order parameters.

We next discuss our two order parameters in a little more detail. The first, ϕ, was the angle of the direction of maximum extension to the z-axis. It was allowed to vary between 0 and $\pi/2$. ϕ was determined by finding the eigenvector of the largest eigenvalue of the radius of gyration tensor. The second, C_2, was defined as follows

$$C_2 = \frac{1}{NR} \sum_i \min(|\mathbf{r}_i - \mathbf{r}'_j|), \tag{7.2}$$

where R is the average bead separation and $\mathbf{r}'_j$ are the bead positions rotated about

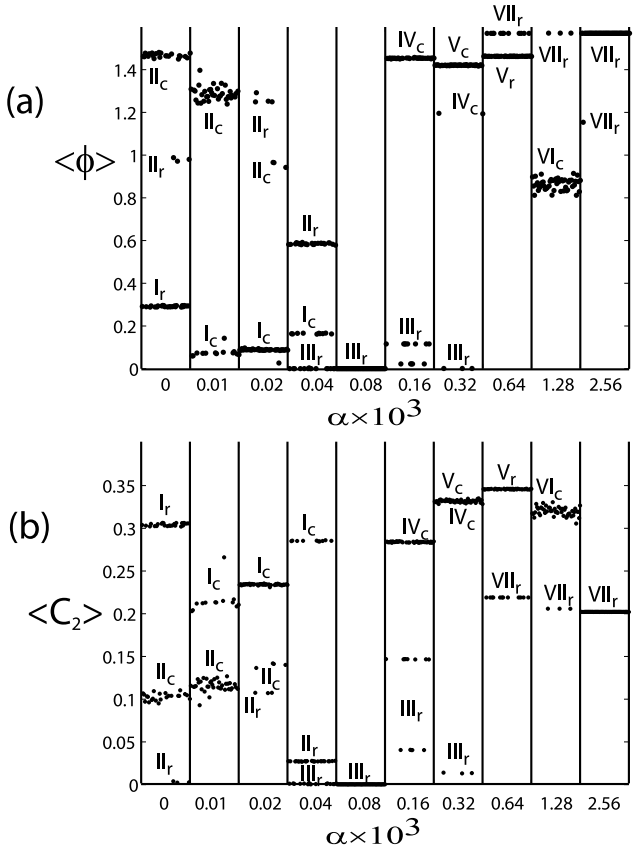


Figure 7.2: The modes observed for $N = 50$ filaments at different values of α. (a) The angle of the direction of maximum extension to the z-axis, ϕ. The averages of ϕ for each run are plotted for a given α in an arbitrary order. The labels indicate the modes to which the points correspond. (b) The same as (a) but for C_2, an order parameter to detect two-fold symmetry about the z-axis. Lower values indicate more symmetric configurations. It should be emphasised that all the points within two consecutive vertical lines correspond to different runs for the same α – the different positions along the x-axis within each section are irrelevant. The subscripts, r and c, denote regular and chaotic motion, which will be discussed in more detail in subsection 7.3.3.

the z-axis by π in the centre of mass frame: the minimum distance from each bead to a bead in the rotated configuration is summed. Smaller values of C_2 indicate configurations which are closer to being symmetric under a π rotation. For the modes considered here C_2 varies from 0 to about 0.4.

Figs. 7.2 (a) and (b) show the values for these two order parameters for different α. Each point is the average over one of fifty runs – they are plotted in an arbitrary order. It should be emphasised that all the points within two consecutive vertical lines are different runs for the same α – the different positions along the x-axis within each section are irrelevant.

The process of mode family identification was guided by quantitative values but was essentially subjective. Nevertheless, the behaviour of the different modes is quite distinct (as can be seen in the animations [146]).

7.3.3 Regular and Chaotic Motion

Some mode families show both regular and chaotic modes, sometimes at the same α, for example family II. Others showed only regular (VI), or only chaotic (IV), motion. To distinguish regular and chaotic modes, we calculated the largest Lyapunov exponent, σ_1 [147]: a second system was created with the bead positions $\mathbf{r}_i$ each randomly displaced to $\mathbf{s}_i$ and constrained so that $d^2 = \sum_i \mid \mathbf{r}_i - \mathbf{s}_i \mid^2 / \sigma^2 = 1$. Both systems were integrated forward in time. After each $1.5t_0$, $\mathbf{r}_i - \mathbf{s}_i$ were rescaled by changing $\mathbf{s}_i$ so as to make $d = 1$. The Lyapunov exponent is then given by [147]: $\sigma_1 \equiv \lim_{n\to\infty}\sigma_n = \lim_{n\to\infty}(2/3nt_0)\sum_{i=1}^{n}\ln(d_j)$, where d_j is the distance after the j^{th} evolution. If the measured σ_n tended to zero or a positive constant as a function of n, the motion was identified as regular or chaotic respectively. This behaviour is illustrated in the inset of Fig. 7.3.

Fig. 7.3 compares the movement of the average bead position around its average drift in the z-direction for two modes from family II at $\alpha = 0$, one regular and

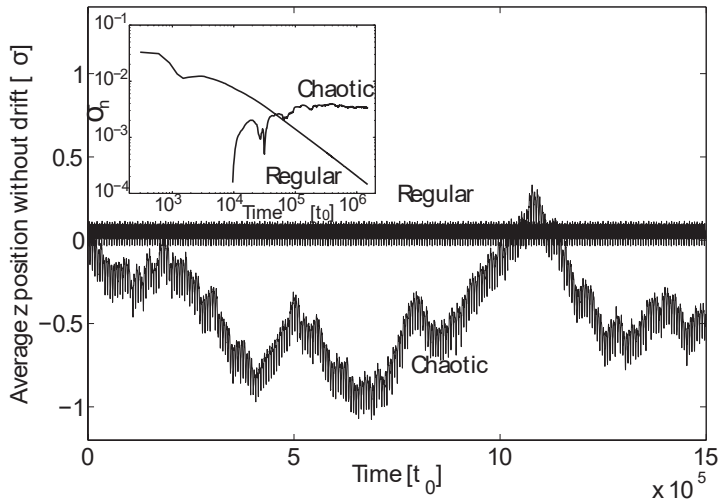


Figure 7.3: Comparing regular and chaotic runs with modes in family II at $\alpha = 0$. The average z-position of the filament beads with the average drift subtracted is plotted as a function of time. The inset shows the estimate of the largest Lyapunov exponent as function of time for the two runs, plotted on a log-log scale.

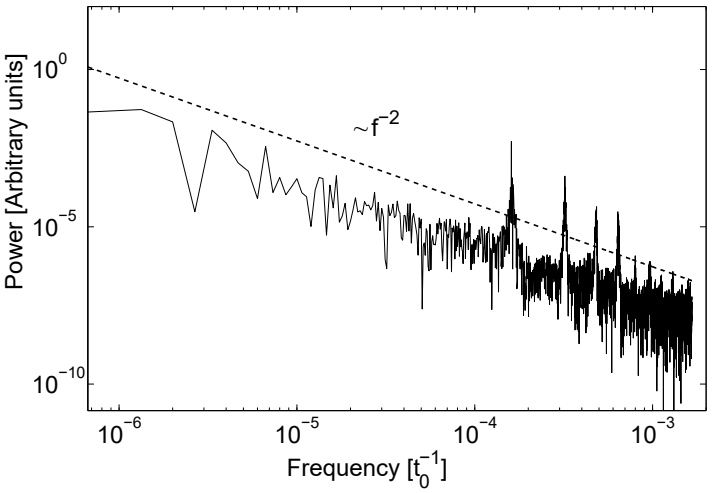


Figure 7.4: Power spectrum calculated by discrete Fourier transform of the displacement about the average drift for the chaotic mode plotted in Fig. 7.3.

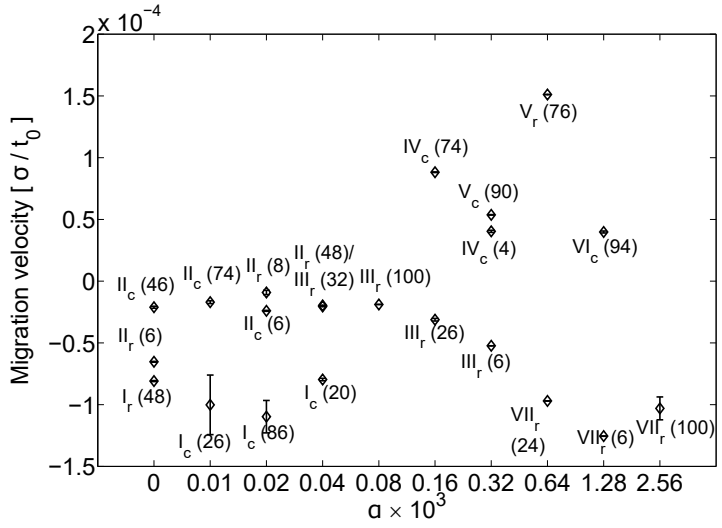


Figure 7.5: Migration velocity in the z-direction, averaged over all runs belonging to each family. The labels indicate families and are subdivided into regular and chaotic modes, denoted by the subscripts r and c respectively. Error bars show the standard deviations. The figures in brackets indicate the percentage of runs at each α that were observed to fall into each group.

one chaotic. The regular mode simply oscillates. By contrast the chaotic mode, whilst showing oscillations, also displays larger movements. The power-spectrum of the curve for chaotic motion, plotted in Fig. 7.4, exhibits a power-law decay with an exponent of about minus 2 (1.94 ± 0.03), suggesting a random walk around the average drift. The power-spectrum was obtained by taking the modulus squared of the discrete Fourier transform of the data series for the displacement of the average bead position around its overall drift.

7.3.4 Average Migration Velocities and Periods of Rotation

Average migration velocities were calculated by a linear fit to the z-displacements of the centre of resistance. Fig. 7.5 plots the averages over all runs, grouped into families and then subdivided into regular and chaotic modes at each α. Error bars indicate the spread of velocities observed. For most families, they are smaller than the data points. Fig. 7.5 also shows that at some α there exist modes that migrate in opposite

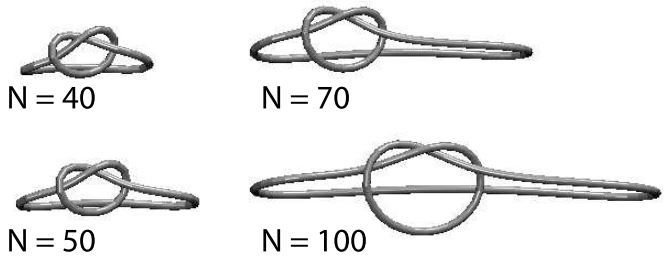


Figure 7.6: Example configurations of the modes at $\alpha = 0.64 \times 10^{-3}$ for $N = 40$, 50, 70 and 100. Full animations of the modes are available online [146].

directions. The period of rotation of regular modes varies with α, approximately in the range $2-6\times10^3 t_0$. The shortest periods were seen for the highest α. For example, at $\alpha = 0$ the average period of modes in the II family was $6220 \pm 40t_0$ and that of family VII at $\alpha = 2.56 \times 10^{-3}$ was $2040 \pm 90t_0$. Fig. 7.5 also shows the percentage chance that a run with random initial conditions ends up in the particular mode family.

7.3.5 Other Parameter Choices

We also considered simulations for other knot types at $\alpha = 0$. For $3_1(+)$, the same modes are seen but the migration, and the orientation, is as expected, in the opposite z-direction. We see similar behaviour – regular and chaotic modes with migration – for more complex knots such as 4_1 and 5_1. For achiral 4_1, the distribution of migration velocities is symmetric about zero: all migrating modes have a partner with opposite migration direction. Depending on initial conditions, the 4_1 knot may thus migrate in the $\pm z$-direction, but that the average migration velocity over many runs would be zero.

Finally, we consider the sensitivity of our results to changes in parameters and changes in simulation details. It should be kept in mind that for these dynamical systems with behaviour that may depend sensitively on initial conditions, one would expect quantitative changes when simulation details are changed. The main thrust of

the chapter is qualitative, and so the most important tests will be whether the overall behaviour, the mode families, are robust to these changes.

Firstly, we consider the effect of hydrodynamic interactions by setting $\mathcal{H}_{ij} = 0$ for $i \neq j$ in Eq. (7.1). We find, as expected, that the motion in the vorticity direction is a consequence of off-diagonal hydrodynamic interactions. Modes that resemble those of families V and VII were seen but none with large z-extensions.

Secondly, linear filaments or unknotted rings with point force hydrodynamics simply align in the x-z plane without access to different shear velocities. Simulations must therefore explicitly take the finite thickness into account by considering the torque on individual beads [137]. We tested this sensitivity by using algorithms that include the torque, and find that, in contrast to unknotted filaments, similar mode families are observed. These simulations are described in detail in sections 7.5 to 7.8. The knot forces the system out of the plane so that it always accesses different shear velocities, and this dominates.

Thirdly, we checked how the behaviour is affected by changing κ, η and $\dot{\gamma}$ in such a way as to keep α fixed. We ran two sets of simulations where $\dot{\gamma}$ was reduced by a factor of 10 and either κ was decreased or η increased to compensate. We obtained very similar results.

Finally, most of our results are for a fixed length filament with $N = 50$ beads. It is interesting to investigate how sensitive our results are to the length, $L = N\sigma$. For example, for $N = 50$, significant tightening first occurs in family V at $\alpha = 0.64 \times 10^{-3}$. We ran additional simulations with $N = 40$, 70 and 100 at $\alpha = 0.64 \times 10^{-3}$. In each case, the majority of runs show a mode very similar to those in family V, see Fig. 7.6. The migration velocities are similar but decrease with L. The measured velocities are 1.60, 1.51, 1.35 and 1.27 $\times 10^{-4}\sigma/t_0$ respectively (in each case all runs in the mode had exactly the same velocity to the accuracy given.) At other α's we checked that the results at different N were also qualitatively similar, although the

agreement worsens at lower α. For example, at $\alpha = 1.28 \times 10^{-3}$ modes like families VI and VII were seen for all N but for $\alpha < 0.16 \times 10^{-3}$ we observed families for $N = 100$ that were qualitatively different to any seen for other N. In fact, we expect substantial differences at small α because the shape of the tighter knot is then fixed by the excluded volume of the chain and not just by the physics that enters into the derivation of α. In that regime, for fixed filament thickness, we expect the influence of the knot to become progressively smaller as $L/\sigma \to \infty$. While it would be interesting to explore these effects further, at fixed $\dot{\gamma}$, changing N while fixing α means that κ must be increased as N^3 and the integration timestep correspondingly decreased for stability. Combining this with N^2 time for calculation of $\mathcal{H}_{ij}$ gives a prohibitive $\sim N^5$ scaling of simulation time.

7.3.6 Summary of Main Results and Overview

To summarise, we have demonstrated that knotted filaments in shear exhibit a rich dynamical behaviour, with modes which can be divided into families. Some families have both regular and chaotic modes. Mode families migrate in different directions along the vorticity axis. The crossover from a stiff knot to the regime where multiple modes are possible can be described by a dimensionless number.

Experimentally, this behaviour would be most easily observable with macroscopic filaments in highly viscous solutions [11]. However, it may also be visible for DNA. For example, the P4 phage genome (common in knotting experiments [28]) is about 77 thermal persistence lengths long. We estimate a crossover ($\alpha = 10^{-3}$) at $\dot{\gamma} \approx 2 \times 10^3 s^{-1}$ in water. The Weissenberg number ≈ 10, so shear should be reasonably strong compared to thermal effects.

In the remainder of this chapter, we consider two issues that arise from the results presented so far. Firstly, in section 7.4, we consider whether there is any evidence of our model displaying behaviour typical of attractors, a feature of dynamical systems

that we have ignored. Secondly, in sections 7.5 to 7.8, we address two deficiencies of our model. We first describe what these are. We then introduce a bead rotation model that introduces new features to address them. We compare results to experiments on linear filaments before finally repeating knotted filament simulations. In section 7.9, we summarise the entire chapter.

7.4 Attractors

The model under investigation is a dissipative dynamical system – the equation of motion fits the general form [147]:

$$\frac{d\mathbf{x}}{dt} = \mathbf{V}(\mathbf{x}), \tag{7.3}$$

where $\mathbf{x}$ is a vector of the system co-ordinates and $\mathbf{V}(\mathbf{x})$ does not have explicit time dependence. As $t \to \infty$, the motion of such systems lies on an attractor, a 'surface' of lower dimension than the system itself [147]. As the parameters of such systems are varied changes in their attractors occur which may be associated with processes such as period-doubling [148], intermittency [149] or crises [145].

We have so far refrained from considering our results in terms of attractors because of two issues: firstly, with our numerical approach, it is difficult to ascertain if the long time motion we observe does truly correspond to attractors of the system. Secondly, assuming that it does, since we integrate using finite time steps, these attractors will be those of a discrete map. It is not simple to say how these might relate to the attractors of the underlying differential equations [150].

For the remainder of this section, we ignore the issues raised above and assume that the long time motions we observe do correspond to attractors of the system. We search for evidence of behaviour characteristic of such systems. Due to the high-dimensionality of our phase space, with typically many attractors at a given set

of parameter values, exploring the system exhaustively is not feasible. Instead, we choose a single example of evidence that appears to indicate an interior crisis [145].

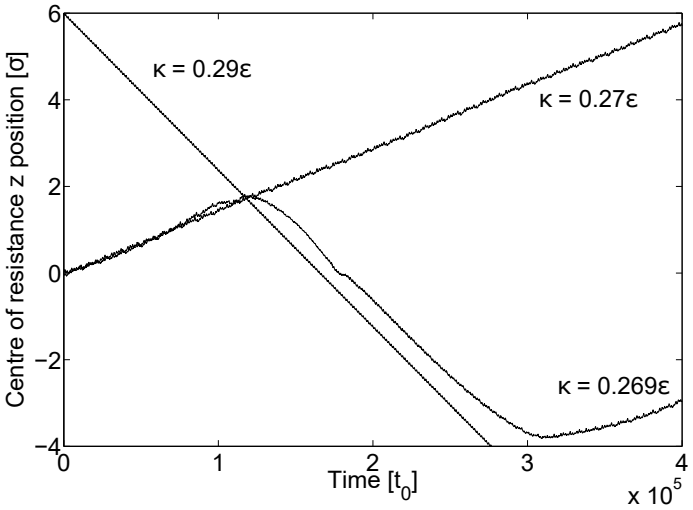


Figure 7.7: Migration of the centre of resistance in the z-direction for filaments of different stiffness in three attractors corresponding to family I. The values of κ, the bending stiffness, are indicated by labels. The attractor labelled $\kappa = 0.29\epsilon$ becomes unstable when κ is reduced. At $\kappa = 0.27\epsilon$ filaments that begin in it fall into another attractor that migrates in the opposite direction. At $\kappa = 0.269\epsilon$ this second attractor changes and moves stochastically between performing motion like at $\kappa = 0.27\epsilon$ and motion like the attractor at $\kappa = 0.29\epsilon$. This may be seen in the different sections of the curve, where migration in opposite directions is observed.

In an interior crisis, an unstable orbit within the basin of attraction of a chaotic attractor collides with it. This results in a sudden expansion of the chaotic attractor [145].

To investigate changes as stiffness is varied, we took configurations from an attractor at a particular κ and used them as starting configurations for simulations at slightly altered values. Initialisations of length $1.5 \times 10^8 t_0$ were run to find if the filaments remained in the original attractor or fell into a new one.

A configuration from a regular attractor corresponding to the I family of modes at $\kappa = 0.29\epsilon$ was taken. It showed $-z$-migration, see Fig. 7.7. It was found that, if κ was reduced, this attractor disappeared. Runs beginning with the configuration performed

the motion transiently but eventually settled into a different, chaotic, attractor. At $\kappa = 0.27\epsilon$ this chaotic attractor (also belonging to the I family) was observed to show $+z$-migration, see Fig. 7.7. By $\kappa = 0.269\epsilon$ the chaotic attractor had changed and filaments were observed to move stochastically between performing motion from the $+z$-migrating, chaotic attractor and the $-z$-migrating (previously) unstable orbit, see Fig. 7.7. We believe this is an example of an interior crisis [145].

An interesting further question is how chaos emerges in the system. We were unable to find evidence of two of the standard routes to chaos – period-doubling [148] or intermittency [149]. We did observe that once chaotic attractors disappeared their orbits were still seen for relatively long transient periods. This is characteristic of crises [151], a third route to chaos, although we were not able to find more definite confirmation of this (the crisis we observed is in a region where chaotic behaviour has already appeared in the system).

7.5 Extensions to Model

In simulations of knotted filaments using the model described in section 7.2, the knot leads to rich dynamical behaviour. Linear filaments and unknotted rings, however, simply align with the flow, adopting configurations in the x-z-plane. This occurs because the current model neglects the action of the shear across the finite thickness of the filament. If this effect is included, it pushes the filament out of the x-z-plane, even with no fluctuations. By contrast, when a knot is present it naturally extends outside a single plane, and so we expect that our model gives a reasonable qualitative picture of the behaviour.

A second possible deficiency of the current model is the lack of torsional stiffness and the omission of the twist of the filament. Without these, a basic feature of closed rings is neglected. As discussed in section A.1.4, closed elastic rings with

torsional stiffness and a defined twist may be assigned a quantity, linking number – the sum of the twist and writhe, which is conserved. The writhe, which depends on the configuration of the contour of the filament, and the twist, the of rotation of the filament around its contour, are thus coupled.

To check the validity of our results for knotted filaments, we modify our existing bead-spring model to include the effect of shear acting across the finite filament thickness so that it can qualitatively reproduce more of the experimental observations for linear filaments. We also consider including torsional stiffness such that linking number for closed rings is conserved.

7.6 Bead Rotation Model

We wish to modify the bead-spring model from section 7.2 to include two effects: the action of the shear across the finite filament thickness and torsional stiffness. The model of section 7.2 neglects the first of these because the bead rotation is ignored or equivalently because the beads are completely free to rotate, unimpeded by their neighbours. We include the effect by introducing a potential that penalises such rotation. The potential depends on bending orientation vectors, which are assigned to the beads. To include torsional stiffness we assign a second set of torsional orientation vectors. These describe the twist of the filament around its contour (see Appendix A.1.4). Fig. 7.8 depicts the orientation vectors employed.

7.6.1 Finite Thickness

To include the effect of finite thickness, the bending potential used in the model of section 7.2, Eq. (3.5), which depends on the relative directions of subsequent bead-to-bead vectors, is replaced by a potential that depends on the relative directions of bending orientation vectors (solid arrows in Fig. 7.8(a)) and adjacent bead-to-bead

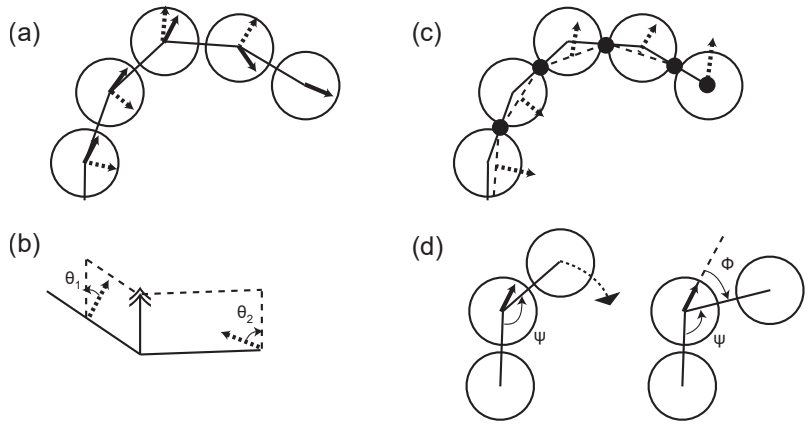


Figure 7.8: (a) There are two orientation vectors assigned to each bead: bending (solid arrows) and torsional (dashed arrows). The solid arrows may rotate in any direction. The dashed arrows rotate around the bead-to-bead vectors. For linear chains there is no dashed arrow associated with the last bead (though there is with the first). (b) Calculation of the twist angle (see Appendix A.1.4) between subsequent beads: The torsional orientation vectors are again represented by dashed arrows. The solid lines join bead centres. The double headed arrow is binormal to the two bead-to-bead vectors. The twist is calculated as the sum of the angles, $\theta_1+\theta_2$. (c) A second approach to including a torsional potential: The black dots indicate the mid-points on bead-to-bead vectors (except for the final one.) The torsional orientation vectors rotate around the mid-point to mid-point vectors indicated by the dashed lines. (d) Contribution of the 'bending' potential to torsion. The top bead in the diagram on the left is displaced in the direction indicated by the dotted arrow to the configuration shown on the right such that the angle labelled ψ doe not change. A force opposing this motion, depending on ϕ, arises from the 'bending' potential although the bending angle, ψ, remains the same.

vectors

$$V_{bend} = -\kappa \sum \hat{\mathbf{t}}_i \cdot \hat{\mathbf{n}}_i + \hat{\mathbf{t}}_{i+1} \cdot \hat{\mathbf{n}}_i, \tag{7.4}$$

where $\hat{\mathbf{t}}_i$ is the unit vector pointing from bead $i-1$ to bead i and $\hat{\mathbf{n}}_i$ is the bending orientation vector associated with bead i. For small deformations, the bending energy for such a potential $\sim \phi^2$, where ϕ is the angle between the vectors.

7.6.2 Torsion

The torsional orientation vectors (dashed arrows in Fig. 7.8(a)) are used to represent the twist of the filament around its contour. The approach from ref. [82] is employed: the torsional orientation vector of bead i rotates around the vector from bead i to bead $i+1$.

The twist of the filament between subsequent beads is calculated by the procedure depicted in Fig. 7.8(b). A torsional potential is included [82]:

$$V_{torsion} = \frac{1}{2}\kappa \sum \gamma_i^2, \tag{7.5}$$

where γ_i is the twist angle, the sum of θ_1 and θ_2 in Fig. 7.8(b), between bead i and bead $i+1$, restricted to the range $-\pi < \gamma_i < \pi$. The potential produces both torques and forces on the beads. The bending and torsional stiffness of the filaments, in the experiments [11] to which we wish to compare the bead rotation model, are not specified. So, since they are typically proportional to each other [83], we simply choose the values of κ appearing in Eqs. (7.4) and (7.5) to be the same.

Note that this treatment of the torsion is not symmetric. There is no twist angle between the final two beads of a linear filament since the bead-to-bead vector for the final bead is not defined. To check whether this has a qualitative effect, we also employ a second approach: now the twist orientation vectors are defined around the mid-point to mid-point vectors as depicted in Fig. 7.8(c). In this scheme, the vectors for the final beads for linear filaments are taken as being the same as the bead-to-bead ones. This approach is symmetric but has the disadvantage that the twist vectors are defined around a contour that does not coincide with the natural one, which passes through bead centres. Nevertheless, we find that very similar motion is seen for both methods.

Although Eq. (7.5) is denoted as the torsional potential, the 'bending' poten-

tial given in Eq. (7.4) will also contribute to the torsional stiffness. As shown in Fig. 7.8(d), Eq. (7.4) will produce forces opposing deformations that do not affect the local bend of the filament.

7.6.3 Dynamical Method

The bead rotation model considers the rotation of beads as well as their translation. For consistency, rotation-rotation and rotation-translation hydrodynamic interactions are included, in addition to the Rotne-Prager tensor, which treats only the translation-translation interactions. Mobility tensors which include terms up to the same level of approximation (up to x^{-3}) as the Rotne-Prager tensor are used [152, 153].

Integration is again performed using the forward Euler scheme. Forces and torques due to the potentials are calculated and the resulting linear and angular velocities, including the hydrodynamic effects from other beads, are found. The linear velocity due to the bead position and an angular velocity of $\frac{1}{2}\dot{\gamma}$ [154] are added. The beads are translated and the bending orientation vectors are rotated. The appropriate component of the rotation *at the beginning of the time step* is applied to the torsional orientation vectors. Then, the rotation due to the displacement of the beads during the time step is added.

7.6.4 Linking Number

In order to check that linking number, Lk, is conserved, the writhe of configurations of closed filaments simulated with the torsional potential, Eq. (7.5), was calculated. A method from ref. [155], which allows the exact value of the writhe for a contour composed of straight sections, was used. The linking number, the sum of the twist and the writhe, was found, to within numerical error, to be an integer and to be conserved. Closed filaments with non-zero writhe were observed to relax to compact, 'super-coiled' configurations, an example of a configuration adopted by unknotted

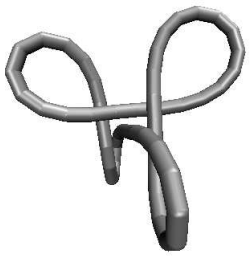


Figure 7.9: An example of a 'super-coiled' configuration adopted by an unknotted filament with $Lk = 4$.

filament with $Lk = 4$ is given in Fig. 7.9.

7.7 Results for Bead Rotation Model: Linear Filaments

Before going on to consider knotted filaments simulated with our bead rotation model, we first look at results for linear filaments. The aim of this section is to determine if our bead rotation model shows reasonable qualitative agreement with experiments of Forgacs and Mason [11], at least in comparison to other simulation approaches [137]. As in section 7.2, and consistently with Forgacs and Mason, we choose the flow to be in the x-direction and the shear to be in the y (such that there are higher velocities at higher y values).

Jeffrey [132] predicted that a rigid prolate spheroid in shear flow will rotate with a period given by

$$T\dot{\gamma} = 2\pi \left(r_e + \frac{1}{r_e} \right), \tag{7.6}$$

where r_e is the axis ratio. For flexible filaments in a highly viscous fluid performing rotations in the shear plane, Forgacs and Mason [11] simply took r_e as being equal

to r, the aspect ratio of the filament. In experimental data, T was seen to initially increase similarly to Eq. (7.6) but deviate below its prediction for higher r because of deformation of the filament. For motion in the shear plane, Forgacs and Mason identified three different regimes:

1. **Rigid motion** The filaments rotate whilst maintaining a straight configuration.

2. **Springy motion** The filaments rotate but the configuration bends slightly as the filament moves away from alignment with the x-axis.

3. **Snakelike motion** The filament is sufficiently deformable that the two ends appear to be able to move independently.

Beyond the regimes where the filament remained in the shear plane, Forgacs and Mason [11] found that when the filaments were made more flexible, or shear rate was increased, motion with extensions out of the shear plane was observed. As deformability increased two more regimes were seen:

4. **Coiled motion** The filaments no longer remain in the x-y plane. They take on configurations in which they are extended along, and coiled around, the z-axis.

5. **Entangled motion** The filaments move towards configurations like those seen in coiled motion but become entangled.

There have been several simulation studies of such filaments in shear flow [144, 156, 137]. These have generally been quite successful at reproducing the first three regimes. There is a tendency for simulations to produce 'S'-type deformations in regimes 2 and 3 as opposed to the 'C'-type deformations seen experimentally [11]. This may be attributed to the lack of shape perturbations [157]. These works have been less successful with regards the last two regimes. In ref. [137], the authors found it necessary to introduce an intrinsic curvature to their filaments in order to observe coiled and entangled motion.

We perform two sets of simulations. The first, described in subsection 7.7.1, compares our model to experimental results from the regimes where the filament remains in the shear plane. The second, described in subsection 7.7.2, looks at the regime where the filament extends out of the shear plane. The results in subsection 7.7.2 are preliminary. Finally, in subsection 7.7.3 we summarise our results and discuss how well our model performs.

7.7.1 In Shear Plane Motion

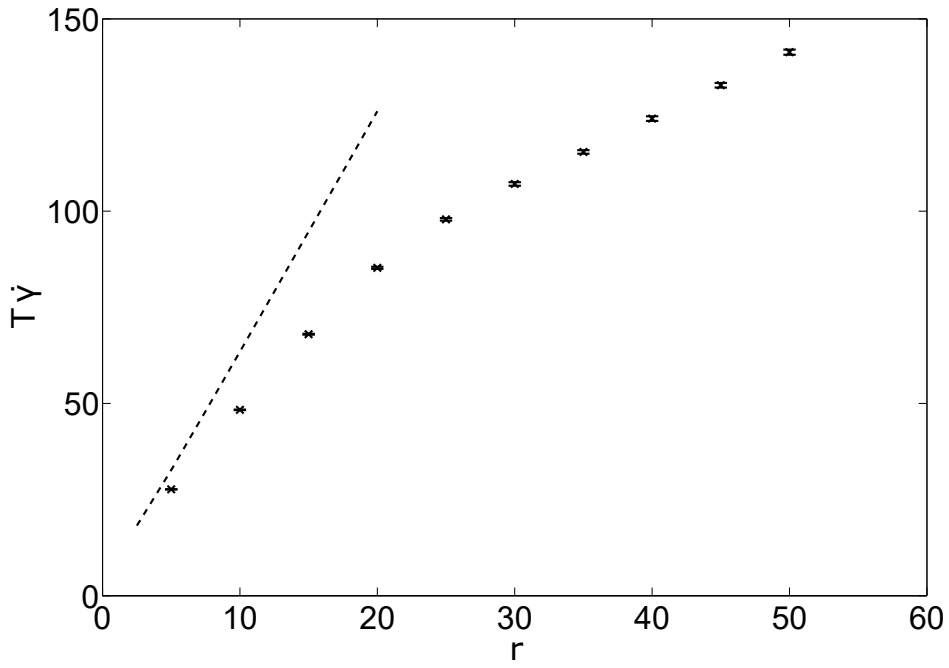


Figure 7.10: The period T as a function of aspect ratio r for filaments with $\kappa = 32\epsilon$ at $\dot{\gamma} = (150t_0)^{-1}$. The dotted line is the prediction from Eq. (7.6) for rigid prolate spheroids of the same aspect ratio.

We investigate the behaviour of filaments performing orbits in the shear plane, in particular the dependence of T on r. Since the motion is confined to a plane, torsional stiffness is not expected to affect results. Simulations confirmed this.

A range of filament lengths, $N = 5-50$, was used with $\kappa = 32\epsilon$ and $\dot{\gamma} = (150t_0)^{-1}$.

Initial filament configurations were in the shear plane. After an initialisation period, T was measured by considering $2\pi t/\phi$ for large t, where ϕ is the angle of the vector from the centre of resistance to the end of the filament (taken to increase continuously) and t is time. Errors were estimated by looking at the oscillations of this quantity in the observation window.

As in experiment [11], for short filaments no significant deformation was observed during their rotation but as length was increased, more and more shape change was seen. Similar to previous simulations, the filaments showed 'S'-type rather than 'C'-type deformations [157]. We plot the dependence of T on r in Fig. 7.10. Qualitatively, although the values of r considered are smaller, Fig. 7.10 shows reasonable agreement with the experimental results; T increases with r and increasingly deviates from the prediction for rigid prolate spheroids. For large r, however, T seems to increase linearly. This feature is not seen, at least not clearly, in experiment. It would be interesting to investigate the origin of this effect further. The deviations from the predictions for rigid objects arise due to deformation. It may be that because our r values are relatively small, beyond a certain flexibility, excluded volume prevents further filament deformation.

7.7.2 Out of Shear Plane Motion

We next look at the motion of more flexible filaments, for comparison to the experimental regimes where extension out of the shear plane was seen. For these simulations, filaments have non-planar configurations, so torsion is expected to affect results. We consider simulations both with and without torsional stiffness. Results for the two different torsional potentials described in section 7.6 were very similar.

We consider filaments of $N = 50$ beads with $\dot{\gamma} = (150t_0)^{-1}$ and $\kappa = 2\epsilon$. We also ran simulations with other κ but we choose to only show results for $\kappa = 2\epsilon$ because they illustrate the main point we wish to make in this section well: for more

flexible filaments our bead rotation model produces some modes of motion that are qualitatively similar to experiment but also others that are not.

We use the simulation protocol from section 7.3: a thermal equilibration to give a 'random' initial configuration, followed by a 'long' initialisation. We only perform a relatively small number of runs, 5. We aim to gain a general picture of the behaviour without exploring it in detail.

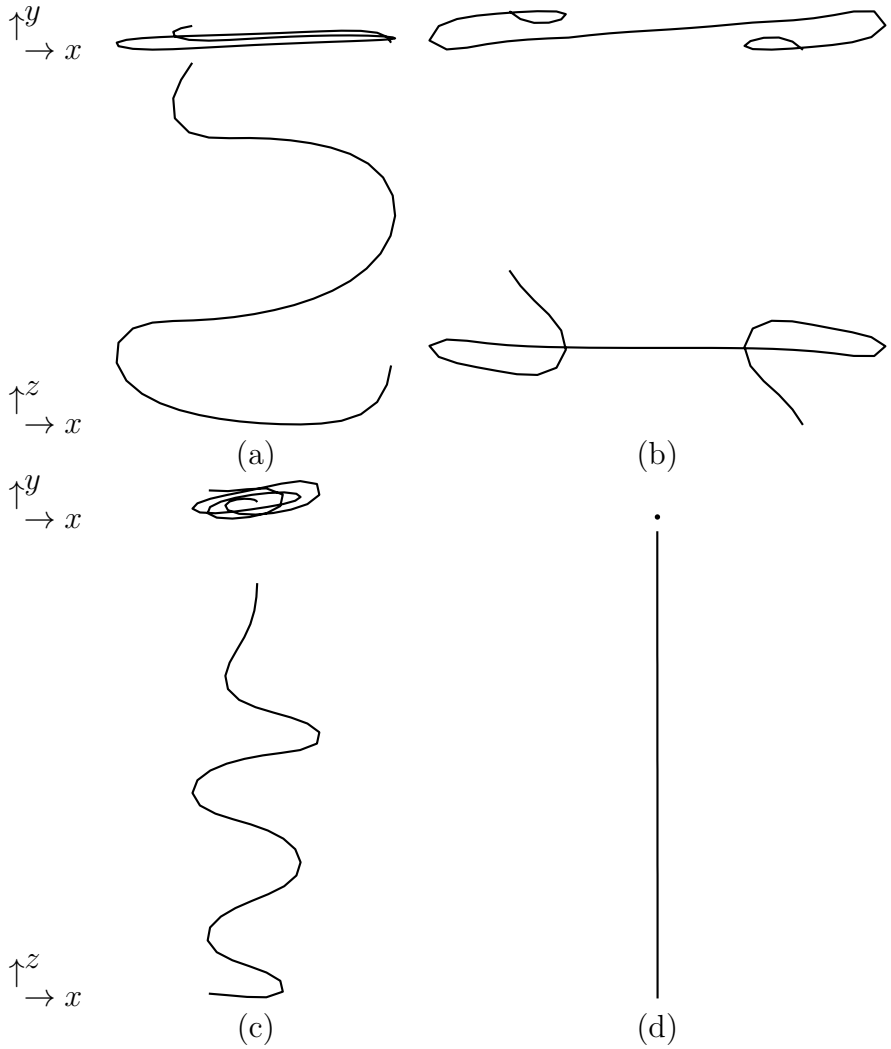


Figure 7.11: Snapshots of filaments of length $N = 50$ at $\dot{\gamma} = (150t_0)^{-1}$ with $\kappa = 2\epsilon$. (a) and (b) Without torsion. (c) and (d) With torsion. In (a) and (c) examples of behaviour observed in simulations that is qualitatively similar to experiment are shown. In (b) and (d) examples of behaviour observed in simulations that is qualitatively different to experiment are shown.

Without torsional stiffness, we observed two different types of modes, which are illustrated by snapshots in Fig. 7.11(a) and (b). In the mode depicted in Fig. 7.11(a) the filament forms a coil whose projection in the x-y-plane has a maximum extension at an angle to the flow. We recall that the flow has been chosen to be in the x-direction and the shear in the y-direction, making z the vorticity direction. The qualitative appearance of the coil is similar to photographs of experimental motion [11], except that the ends are aligned approximately with the vorticity axis, whereas in experiment they are aligned in the flow direction. During motion the coil rotates but its basic shape is maintained, again like experiment. In the mode depicted in Fig. 7.11(b), most of the filament performs rotations in the shear plane but its ends are aligned with the z-axis. This is unlike any motion reported by Forgacs and Mason [11].

With torsional stiffness the picture is broadly similar: the two types of modes we observed are illustrated by snapshots in Fig. 7.11(c) and (d). Again a mode, depicted in Fig. 7.11(c) was seen where the filament forms a coil. Fig. 7.11(d) shows a snapshot of a mode where the filament aligns with the z-axis in a straight configuration, which performs small amplitude oscillations. As for Fig. 7.11(b), this mode does not resemble anything observed by Forgacs and Mason [11].

We did not observe any entangled modes. This may be because of the relatively short aspect ratio of our filaments compared to experiment [11].

7.7.3 Summary and Discussion

To summarise, we have performed two sets of simulations to make a qualitative comparison of our bead rotation model to the experiments of Forgacs and Mason [11]. For relatively stiff filaments, we observe motion in the shear plane, qualitatively like experiment: in particular we see a similar dependence of the period of rotation on filament length. For more deformable filaments, we observe that the filaments tend to adopt configurations with extensions along the z-axis, similar to experiment [11].

Also like in experiment, they show a tendency to form coils whose projection in the x-y plane have a longest extension that is inclined at an angle to the flow. We also observe motion that is different to experiment such as a mode where the filament aligns with the z-axis in a straight configuration and performs small amplitude oscillations. We did not observe any entangled motion.

In earlier work [137], a more sophisticated simulation model failed to produce any extension in the z-direction, or coiling, unless a curvature of the filaments was imposed. In the context of this, we feel that our bead rotation satisfactorily reproduces qualitative features of experiment. We go on to use it to simulate knotted filaments in section 7.8.

7.8 Results for Bead Rotation Model: Knotted Ring Filaments

We repeat simulations from section 7.3 with $N = 50$ filaments using the bead rotation model described in section 7.6, with and without torsional stiffness (we do not repeat $\kappa = 0$ since then both models are identical). For $3_1(-)$ knots with torsional stiffness, we close the ring at $Lk = -3$. The writhe of the equilibrium configuration of an $N = 50$ filament with this knot is close to this value.

In both cases, we observe modes that qualitatively fit with families I, III, V, VI and VII but not families II or IV (see Fig. 7.1). The order in which the families appear as κ is increased is the same. The new modes show migration in the vorticity direction with velocities of similar magnitudes to the old but there are differences. For example, modes belonging to family I tend to migrate in the opposite direction.

With torsional stiffness, two modes that are qualitatively somewhat different to any seen for the simpler model are also found. One, seen at $\kappa = 0.5\epsilon$, is most like family I but with two 'tails' of opposite handedness extending in the $\pm z$-directions, a



(a) (b)

Figure 7.12: Snapshots from simulations of $N = 50$ ring filaments with a $3_1(-)$ knot with torsional stiffness at $\dot{\gamma} = (150t_0)^{-1}$ with hydrodynamic interactions. The snapshots are from the two modes observed that are qualitatively different to any seen with the model from section 7.2. (a) $\kappa = 0.5\epsilon$ (b) $\kappa = 1\epsilon$.

snapshot is shown in Fig. 7.12(a). The second, seen at $\kappa = 1\epsilon$, is most like family V, in that the largest extension is approximately in the flow direction, see Fig. 7.12(b).

Without torsional stiffness, regular and chaotic modes are seen, as with the simpler model. Intriguingly, with torsional stiffness, motion appears to always be regular. It would be interesting to investigate further to establish the reason for this.

Without hydrodynamic interactions, as with the simpler model, only modes in which the filament does not have 'large' extensions in the z-direction are seen.

7.9 Summary and Further Work

To summarise, we initially used a simple model to demonstrate that knotted filaments in shear exhibit a rich dynamical behaviour with modes which can be divided into families. Some families have both regular and chaotic modes. Mode families migrate

in different directions along the vorticity axis. The crossover from a stiff knot to the regime where multiple modes are possible can be described by a dimensionless knot deformation number.

We then discussed two limitations of our original model: that it could not reproduce experimental behaviour for linear filaments and did not have torsional stiffness. We introduced the bead rotation model, which used new potentials to remedy the situation. The bead rotation model showed reasonable qualitative agreement with experimental results for linear filaments. For knotted filaments, it showed similar qualitative behaviour to our original model.

In future work, it may be interesting to consider more sophisticated treatments of the hydrodynamics that include effects such as lubrication. It may also be interesting to consider the effect of noise on knotted filaments: initial simulations suggest that fluctuations may alter the stability of modes leading to a variation or even flipping of migration velocity as function of noise strength. The Stochastic Rotation Dynamics algorithm described in section 3.2.3 could be a useful method for such simulations. However, it is likely that modified methods that conserve angular momentum locally [158] would be necessary. Determining if our proposed knot deformation number does truly dictate when knot-tightening occurs would be a key issue to address. If it does, then the interplay between it and the sperm number [143] would be interesting to understand.

For linear filaments, examining the bead rotation model in more detail might give some insight into the mechanism by which filaments are pushed out of the shear plane when they become more deformable. We have not explored the parameters of this model in great detail. It may be that by varying the relative values of the bending and torsional stiffness, closer agreement with experiment could be achieved. By increasing filament length, it might be possible to observe entangled dynamics.

The interplay of torsion and shear and its effect on dynamics is a potentially

interesting area and it would be intriguing to explore it further. In particular, the observation that for knotted filaments the introduction of torsional stiffness leads to motion that is exclusively regular is very surprising and would be fascinating to understand. A final possibility would be to simulate knotted and unknotted rings with non-zero linking numbers under shear.

Chapter 8

Ejection of Knotted Polymers from a Capsid

8.1 Introduction

In this chapter, we consider the effect of knotting on a polymer being pushed out of a spherical shell through a small hole by confinement pressure. Our simulations are a simple model of the ejection of DNA from a bacteriophage. In this introductory section, we start by reviewing some basics about bacteriophages and then go on to describe experiments on the ejection of DNA from them. We consider evidence for knotting and discuss why its relation to ejection is important to understand.

Bacteriophages are viruses that infect bacteria. The processes by which the genome is transferred have been the focus of considerable experimental interest. A phage consists of a capsid head, typically with dimensions of several tens of nanometres, comparable to the persistence length of the DNA. The genome is contained in the head. The capsid also has a tail of length up to several times the diameter of the head, through which the DNA exits. Before genome transfer the tail binds to a membrane protein. For example, phage T5 [159], which infects *E. coli*, binds to

FhuA, a channel used as a ferrichrome transporter. In ref. [159], electron tomography was used to image T5 phages bound to liposomes containing FhuA. The tails were resolved as cylinders with inner diameter of a few nanometres. The tip of the tail was seen to transverse the lipid bilayer and also to undergo a conformational change upon binding. By purifying receptor proteins such as FhuA (or LamB for λ phage) it becomes possible to trigger the ejection of phage DNA *in vitro*. This has led to many experiments looking at the ejection process that use a variety of techniques, which we now summarise.

Ejection dynamics may be monitored by staining DNA with fluorescent dye and using fluorescence microscopy, although this does have the disadvantage that the binding of the dye changes the DNA properties. This approach has been applied to T5 [160] and λ [161] phages. For λ phage Grayson *et al.* [161] found that longer genomes eject faster. A second possibility is light scattering, which has been used to study T5 [162, 163], λ [164, 165, 166] and SPP1 phages [166]. Both Frutos *et al.* [162] and Löf *et al.* [164] investigated temperature effects and found results consistent with an activation process.

A third approach, first reported by Evilevitch *et al.* [167], which does not follow dynamics but gives information on forces, is the use of osmotic pressure to suppress ejection. Various techniques may be applied to measure the amount of DNA remaining in the capsids once equilibrium is reached. Evilevitch *et al.* found that a pressure of 20 atmospheres was sufficient to stop ejection from λ phage entirely, whereas all lower, non-zero pressures investigated led to partial ejection. In ref. [168], it was shown that the partial ejection corresponded to all phages ejecting part of their genome. This technique has also been applied to T5 [169] and SPP1 [170] phages with similar results observed.

It is believed that, for many phages, ejection is largely driven by the pressure arising from the packing of the genome in the rigid capsid head. Remarkably long

strands of DNA can be packed to almost crystalline densities. For example, λ phage has a genome of length $16\mu m$ squeezed into a spherical capsid with a diameter of just 58 nm. Internal pressures can thus be on the order tens of atmospheres. A number of the generic features of the ejection experiments can be explained by treating the DNA as a simple model polymer that is driven from the capsid by the energetic and entropic penalty of close confinement [171, 172, 173, 174, 175].

There have been a pair of interesting experiments [28, 62] that look at the knotting of DNA inside a capsid. Arsuaga *et al.* [28] extracted DNA from phage P4 and a tailless mutant thereof. After extraction, the DNA was cyclised via the cohesive ends of the genome and the spectrum of knots present analysed by electrophoresis. The probability of knotting was higher for tailless mutants but there was still almost a 0.5 probability that DNA from the tailed P4 phage was knotted, much higher than the probability of about 0.03 found in earlier work for P4 genomes cyclised in free solution (but after first being incubated at high temperature to remove knots). The genomes of the phages used in the ejection experiments discussed are all significantly longer than the 11.6 Kbp P4 genome (bp stands for base pairs) – 48.5 Kbp for λ, 121.4 Kbp for T5 and 44.0 Kbp for SPP1 – so may well be more highly knotted than P4 [176].

Recent simulations have provided further evidence for the prevalence of knots in a confined polymer: Micheletti *et al.* [176] showed that the probability of knotting for a polymer contained in a sphere increases with the polymer length and the degree of confinement, in agreement with earlier work [23]. Although the spectrum of knots seen in experiments was not exactly the same as those from simulations of a random polymer, a fact which presumably reflects the chiral nature of the DNA packing [62], the fact that DNA is highly knotted is remarkable. Knots can prevent the transcription of DNA by RNA polymerase [26], and cells have developed a number of active ways to control these entanglements, for example through the use of topoisomerases.

Although phage genomes do code for topoisomerases, these could only act later once DNA had been transcribed and so another mechanism to remove knots may be necessary. The head-tail connector has a channel of diameter 2.3 nm in λ [177] and 1.7 nm in $\phi 29$ [178], compared with an interstrand spacing of about 2.5 nm for packed DNA [179, 180]. Considering that, for a knot to pass, multiple strands must go through simultaneously, even simple knots in DNA are expected to be too large to fit. We assume that instead the DNA must be extruded by reptating through the knots. A biological advantage would be that the viral DNA would enter the bacteria unknotted.

The knotting of bacteriophage DNA has been demonstrated by experiments, which are supported by simulation work. The ejection of the DNA from the capsid could act as an crucial mechanism for removing these knots. The effect of knotting on ejection is thus important to understand and it is our aim in this chapter to contribute towards this goal by performing coarse-grained simulations.

8.2 Method

Our approach builds on the success of previous modelling [181, 174, 175] that reproduced generic effects seen in experiments. The polymer representing DNA is initially confined to a spherical capsid. It is allowed to eject through a small hole, and the driving force is the pressure of the packed DNA in the capsid.

We applied the polymer model with FENE springs, Eq. (3.2). We coupled it to the Stochastic Rotation Dynamics solvent described in section 3.2.3. We considered both flexible and semiflexible chains by including the bending potential given in Eq. (3.5). κ is a bending energy: we used $\kappa = 0$ and $\kappa = 10 k_B T$, which corresponds to a persistence length of 10 beads, on the order of the diameter of the capsids, as is the case for real bacteriophages.

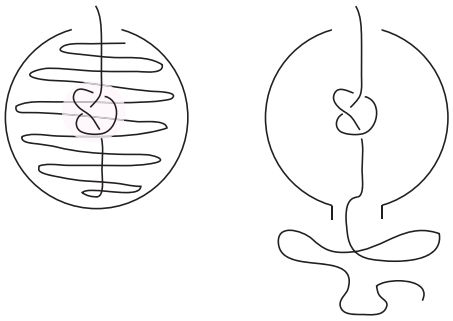


Figure 8.1: Schematic of initial configurations: Left, a spooled chain, right, a random configuration is achieved by packing the chain through a hole at the bottom of the capsid, which is closed before equilibration.

The viral capsid was modelled as a hard spherical shell by applying a force of magnitude $k_BT/(\sigma f^4)$ to beads when their positions satisfied the inequality $\mid f \mid \leq 0.2$, where $f = 1 - (x^2 + y^2 + z^2)/R^2$. In addition, we added a single hole small enough that only one bead at a time could pass through. Two sizes of capsid were considered: one with a radius of $R = 3.02\sigma$ and a second with $R = 4.36\sigma$, which leads to a volume three times larger.

Two types of initial configuration, shown in Fig. 8.1, were considered. In both cases, the knot was put in by hand in a tight configuration near the exit, its type confirmed using the Alexander polynomial. In the first case, the remaining beads were positioned to form a spool [179]. In the second, they were initialised in a random configuration outside the capsid and the polymer was then packed by a motor pulling it through a second hole in the capsid, opposite to the first. After the packing was completed, the second hole was closed. In both cases the polymer was equilibrated (within its local minimum), with the first bead held in position just outside the capsid, before the start of the ejection.

Polymers of length 100 beads were used with the smaller capsid, and polymers of length 300 and 230 were used in the larger capsids for the random packing and the spooled packing respectively. All reported simulation results are averaged over at least 50 independent runs.

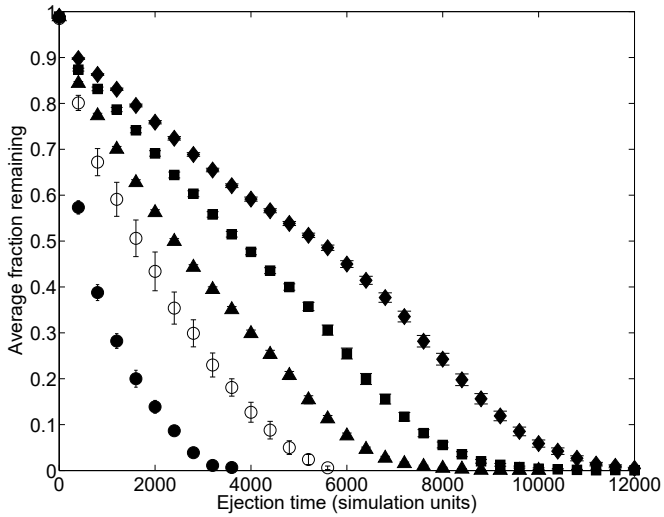


Figure 8.2: Fraction of beads remaining in the capsid as a function of time for unknotted flexible (●) and semiflexible (○) polymers and for flexible polymers with 3_1 (▲), 4_1 (■) and 6_1 (⧫) knots. The knots have a clear effect on the shape of the ejection curve, and the rate of ejection is primarily determined by knot type.

8.3 Results

We find that the knots control the rate at which the polymer can leave the capsid, with slower ejection rates observed for more complex knots. Fig. 8.2 shows typical results for the fraction of beads left in the capsid as a function of time from the release of the polymer. For this figure, we used a small capsid and a random initial configuration but very similar results are found for other packings, initial conditions and capsid sizes. We compare results for unknotted chains to those with the knots 3_1, 4_1 and 6_1. Fig. 8.2 shows that there is a clear slowing of the rate of ejection when a knot is present. Moreover, the rate of ejection depends on the type of knot: the more complex the knot, the slower the rate of ejection.

At very early times, the rates of ejection are similar and relatively high for both knotted and unknotted polymers. This corresponds to the knot being tightened and pushed to the capsid entrance as any free beads between the knot and the exit are

ejected. The knot is too large to escape, so once it has moved to the hole it is held there by the excess pressure inside the capsid. Now the polymer has to reptate through the knot before any monomers are free to allow further ejection. Essentially the knot is acting as a ratchet. If it diffuses a small distance into the capsid, this frees a length of polymer between the knot and the capsid entrance. The knot is then quickly pushed back towards the entrance by the driving force and the free section of polymer is ejected. Near the end of the ejection, when only about $\sim 30 - 40$ beads remain in the capsid, the ejection speeds up and there is a shoulder in the curves in Fig. 8.2. This corresponds to the knot becoming undone.

Simulations for longer polymers in a capsid of radius 4.36σ showed the same generic behaviour. Some small differences were that the final unknotting occurred with a somewhat larger number of beads left in the capsid because there was more free space, and that the rates sometimes showed a slight decrease with time, most likely because the pressure decrease has an effect on knot dynamics. For the $N = 300$ randomly packed polymer, we sometimes also observed initial jamming, with large variations in ejection time between runs. This occurred because the knot was initially trapped in a very tight configuration. However, once ejection did start, the rate was independent of the initial jamming time.

8.3.1 Changing Knot Position

To confirm the effect of the knot on the dynamics, Fig. 8.3 compares similar ejection curves for a semiflexible polymer for length $N = 100$ for three different initial conditions (i) unknotted, (ii) with a knot initially at the the polymer mid-point (iii) with a knot initially at capsid exit. For case (ii) the polymer initially ejects with the same speed as the unknotted polymer (i), but, once the knot has reached the capsid exit, the rate becomes similar to case (iii).

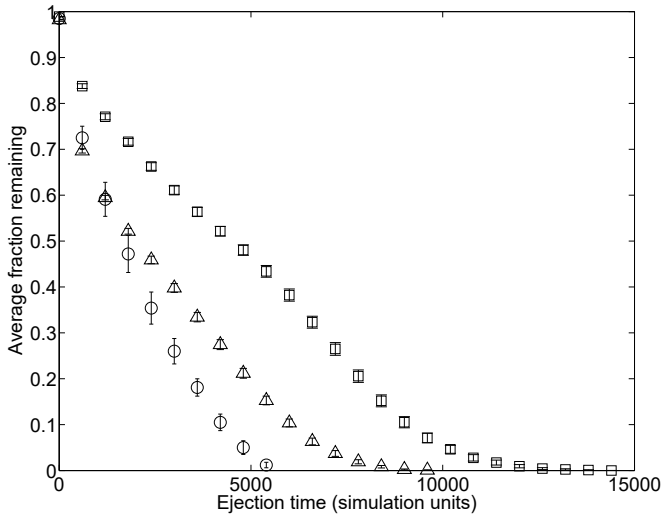


Figure 8.3: Fraction of beads remaining in the capsid as a function of time for semiflexible polymers: (i) unknotted polymer (○) (ii) polymer with a 6_1 knot initially at the mid-point of the polymer chain (△) and (iii) a polymer with a 6_1 knot initially near the capsid entrance (□).

8.3.2 Ejection Rates

A quantitative comparison of ejection rates is shown in Fig. 8.4. Results are presented for both flexible and semiflexible polymers for knots with up to 6 crossings for $N = 100$ chains in the small capsid, and for knots with up to 12 crossing for $N = 230$ chains in large capsids. Average rates were obtained by measuring the time taken for between 75% to 35% of the beads to be expelled. This protocol was chosen to avoid any early time jamming and the late time unravelling of the knot. Small changes in the cut-offs gave no qualitative changes in the results. The results plotted are for the knots of type C_1. Other knots, such as 5_2 and 6_2, were considered. The results were very similar to the C_1 knots with the same C.

Fig. 8.4 shows the trend of decreasing ejection rate with increasing knot complexity. For the unknotted case, there are clear differences between the different kinds of polymers and capsids, but for more complex knots, the rates converge and seem to be almost completely determined by the knot type. This suggests that, for tight,

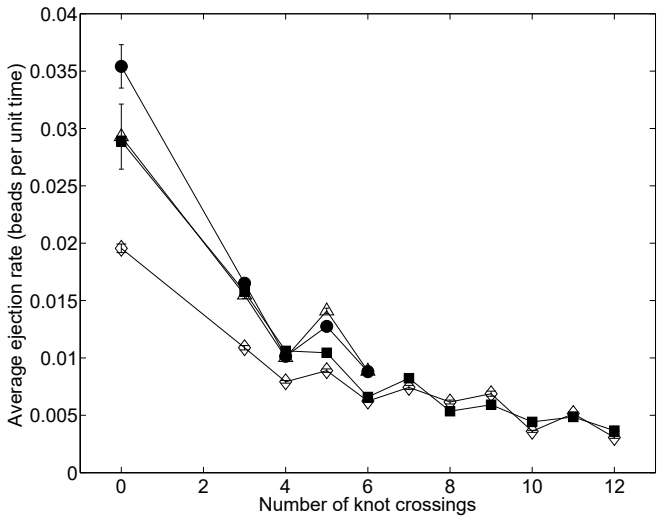


Figure 8.4: Average ejection rates for C_1 knots: flexible polymers in the smaller capsid (•); semiflexible polymers in the smaller capsid (△); flexible polymers in the larger capsid (■); semiflexible polymers in the larger capsid (◊). For more complex knots, the rates for flexible and semiflexible polymers are very similar.

confined knots, the rate of reptation of a knot may be independent of its flexibility. A similar independence of knot properties – the minimum length-to-radius ratio required for a tube forming a knot [56] and the diffusion constant [125] – from flexibility has been reported.

Finally, we note that the ejection rates show a weak oscillation as a function of knot size. The plausible explanation for this is that the knots we consider here with even and odd crossings belong to families with different topologies. Knots 3_1, 5_1 and 7_1 are torus knots and 4_1, 6_1 and 8_1 are even-twist knots. It is reasonable that there is a weak dependence of the reptation rate along the chain on the knot topology. We have observed a similar oscillation of the polymer diffusion coefficients of knots on unconfined polymers under tension, see Chapter 6.

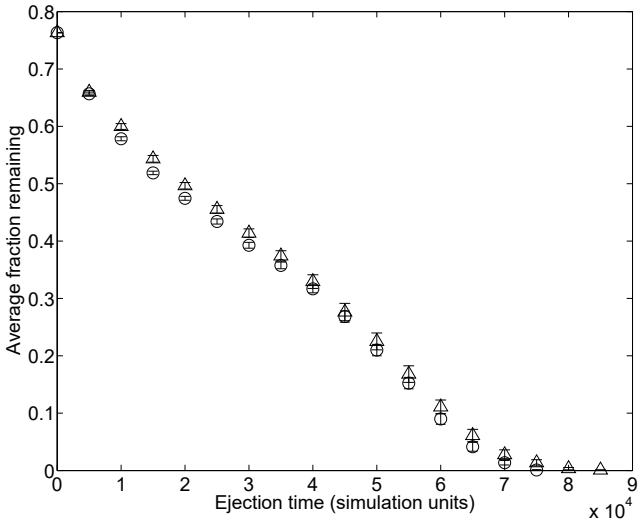


Figure 8.5: Fraction of beads remaining in the capsid as a function of time for semiflexible polymers with three knots randomly selected from 3_1, 4_1, 5_1, 5_2 and 6_1 ($\triangle$) and the prime knot 12_1 ($\circ$).

8.3.3 Multiple Knots

Experiments suggest that there could be multiple knots in the DNA in a viral capsid [28, 62]. To investigate the effect of multiple knotting we ran 50 simulations in each of which three knots, chosen randomly from 3_1, 4_1, 5_1, 5_2 and 6_1 were placed on the chain, near to the entrance of a larger capsid. Fig. 8.5 compares the averaged ejection curve to that for a single 12_1 knot, showing that the knots stack up at the capsid entrance and behave like a single prime knot with a similar number of crossings. For the longer DNA in a viral capsid, one might expect to see multiple knots which would sequentially collect at the exit. Thus the knot length would increase with time, which is expected to slow the ejection rate. It will be interesting to see if any sign of this effect can be seen experimentally.

8.4 Summary and Discussion

To summarise, we have used simulations to determine the effect of knotting on the ejection of flexible and semiflexible polymers from a spherical capsid. We find that the ejection rate is controlled primarily by the knot, not the pressure of confinement. The knot moves to the hole in the capsid and then acts as a ratchet. Polymers with more complex knots eject more slowly. For tightly confined knots, the flexibility of the polymer is not key in determining the rate of ejection.

Our model of a bacteriophage is highly simplified. For example, we ignored the tail. We checked that this does not have an important effect on the qualitative behaviour by simulating a capsid with a tail attached (modelled as a cylindrical shell). Perhaps more importantly, to make simulation feasible, our model of DNA inevitably ignores much chemical detail and our polymer diameter to persistence length ratio is much larger than in real DNA. Moreover, viral DNA is typically much longer than the polymers we study. However, we argue that the generic effects we observe: that the ejection rate is dominated by the rate of knot reptation, and that the knot is unravelled as it emerges from the capsid, are basic properties of knotted polymers moving through a narrow exit hole, and should therefore be robust to the inclusion of these details. Knots in phages may initially be loose but they may be tightened as the DNA is forced through the capsid entrance.

The mechanism by which the knot acts as a ratchet should be common to situations where the translocation of knotted polymers through a pore is driven. It might also be of interest to ask whether knots can affect the motion of biomolecules as they traverse artificial nanopores [182]. We investigate a similar system in Chapter 5 but there the channel size is similar to the radius of gyration rather than the width of a strand and so different physics is observed. Repeating capsid packing experiments [183] with knotted DNA could also shed light on the dynamics of knots in polymer chains.

Recent simulations [184], published since the completion of the work described in this chapter, suggest that knots formed by confining a polymer in a capsid will not be pulled sufficiently tight during ejection to have an effect. In ref. [184], Monte Carlo simulations were performed packaging chains of $\sim 10^3$ beads into capsids. Knots were found to be formed in this process but to be delocalised, taking up $\sim 60\%$ of the chain. When knotted chains were subsequently allowed to eject the dynamics were not observed to be significantly different from unknotted chains. It would be interesting to investigate the conditions under which knot-tightening will occur in such processes.

Chapter 9

Knots in Polymers of Non-Uniform Flexibility

9.1 Introduction

As discussed in section 2.2.2, type II topoisomerases are enzymes that may knot or unknot DNA by introducing a transient break in one strand and passing a second through it. They tend to act preferentially on certain sequences in DNA [46].

There is evidence that sites that are more frequently cleaved tend to be located in or next to parts of the genome called scaffold associated regions (SARs) or matrix attachment regions (MARs) [185, 186, 187], which are rich in adenine (A) and thymine (T), two of the nucleotides in DNA. Further, the specific sequence evolved *in vitro*, which was preferentially cleaved by a certain type II topoisomerase, was highly AT-rich [46].

A and T from complementary strands only form two hydrogen bonds when they bind in the formation of the DNA double helix, compared to three for cytosine (C) and guanine (G). It is believed that AT-rich sequences are more flexible than random ones [187, 188, 189, 190]. For example, the work of Okonogi [189] suggests that a

sequence of AT repeated is about 20% more flexible than a random sequence and earlier work found that such an AT sequence had a persistence length less than half that of a GC sequence [188]. Scipioni *et al.* [190] observed a correlation between AT-rich parts of a DNA fragment and flexibility using scanning force microscopy.

Further, Masilah *et al.* [187] found that there is a large opening of the base-pairs immediately adjacent to a preferentially cleaved site. This opening was found to be dependent on the sequence context. Opening of base-pairs can lead to greatly increased local flexibility [191]. Very high flexibility at the topoisomerase II cleavage sites is probably necessary because the enzyme enforces a large bend in DNA when it binds to it [50].

The combination of these facts, the tendency of topoisomerase II to act near more flexible regions of the genome and its role in knotting and unknotting DNA, suggest that it would be interesting to investigate the behaviour of knots in polymers that are of non-uniform flexibility. Exploring such systems could also give insights into the entropic penalty of knotting, which is generally important for understanding knotted polymers. Therefore, we investigated knots in coarse-grained polymer chains with regions of different flexibility. We found that, if a polymer is composed of two parts of different flexibility, the probability of locating the knot within each changes depending on their stiffnesses and the applied tension.

In section 9.2 of this chapter, we describe the model and methods applied. The results we have obtained are presented in section 9.3. It should be emphasised that we only consider a limited selection of parameter choices. We aim to demonstrate the interesting effects that are present in the system to stimulate, and guide, efforts to explore them in more detail. We outline a possible explanation for our results in subsection 9.3.5. Since our results are preliminary, it is particularly important to consider possibilities for further work: we finish the chapter by discussing a variety of extensions in section 9.4.

9.2 Model and Methods

Initially simulations were performed using closed ring polymers. Knots' positions were found using the method described in section B.3. The results suggested knots tend to be found with higher probability in the parts that have higher stiffness. However, without tension the knot size became very large compared to the total polymer length and it was questionable whether it was meaningful to claim that a knot was located in any particular subsection.

We thus considered instead the case where the polymer is held under tension. For lower tensions, the knot may still become relatively large but it is generally pulled sufficiently tight that in animations a visual identification of its position is possible. In this way, it is possible to get a feel for whether the results given by the knot-finding algorithm are reasonable.

The problem of knots in polymers under tension is also considered in Chapter 6. There hydrodynamic interactions were included but not found to qualitatively change the behaviour. Here we are interested in equilibrium distributions so we applied the Langevin dynamics method described in section 3.2.1 with the polymer model with FENE springs, Eq. (3.2). Tension was applied to the polymers using the method of connecting the polymer across the periodic boundaries described in section 6.2.

The bending stiffness was introduced using the following potential, identical to Eq. (3.5), except that the bending energy may be changed between different beads by choosing different values of κ_i

$$V_{bend} = \sum_i \kappa_i \left(\hat{\mathbf{r}}_i \cdot \hat{\mathbf{r}}_{i-1} \right),$$

where $\hat{\mathbf{r}}_i$ is a unit vector from bead i to bead $i+1$. For all the results shown the knot type is the trefoil, 3_1.

Since we wish to use relatively low tensions, at which there will be crossings of

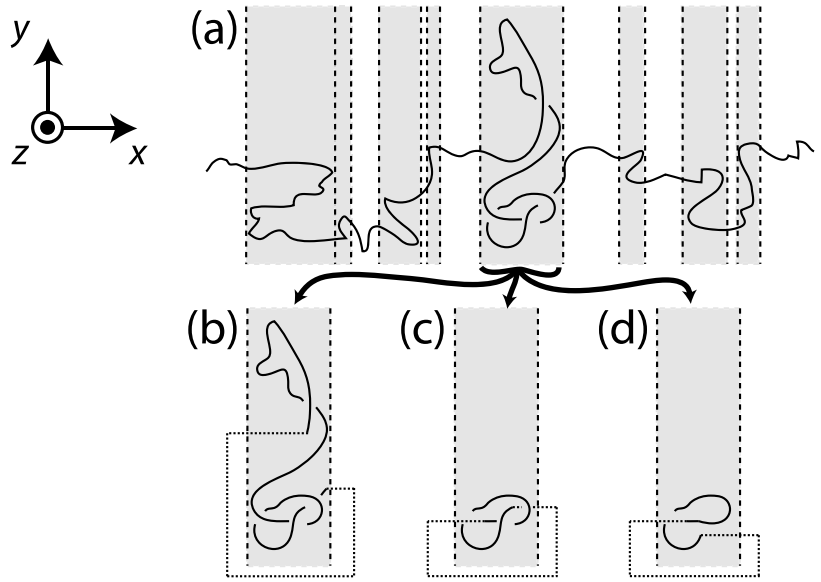


Figure 9.1: Schematic depiction of the knot-finding process. (a) The polymer is divided into sections by finding points along its contour – indicated by the dashed lines – at which there is a boundary between regions where only one strand crosses the y-z plane and those where multiple strands do. Regions in which there are multiple crossers are identified, these are indicated by the shaded areas. They may be closed and the Alexander polynomial calculated to identify which of them contains the knot. (b) - (d) A finer determination of the knot position may be achieved by taking the knot-containing section and closing subsections of it by extending the polymer ends in the x-direction as shown by the dotted lines. The Alexander polynomial may then be calculated. The smallest section with the correct Alexander polynomial is taken as containing the knot. (b) - (d) show a few examples of subsections. The subsection shown in (c) would be identified: that in (b) is too large and that in (d) has the wrong polynomial.

the polymer in a given projection outside the knot region, the knot-finding method of Chapter 6 is not useful. The knot-finding algorithm that we used here is summarised in Fig. 9.1. Like that in section B.3, it is based on calculating the Alexander polynomial for subsections of the polymer. Since the polymer is extended in the x-direction by the tension there will be, as long as the tension is not too low, x-positions at which only one part of polymer crosses the y-z-plane. Regions that are bounded by such points are considered. Only one of them will have the correct polynomial and it may be said with certainty that the knot is located within it – the false positives depicted

in Fig. B.5 will not occur. The centre of this region, measured along the contour, is taken as one measure of the knot position. A second, finer, knot position is found by taking subsections of this region and closing them by extending the open ends in the $\pm x$-direction. Errors of the type shown in Fig. B.5 may now occur.

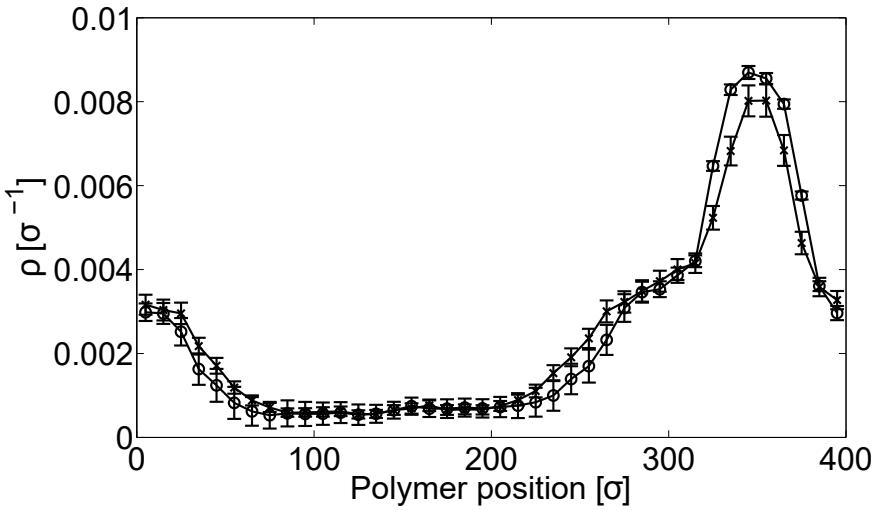


Figure 9.2: Probability density of finding a knot at different positions along a polymer of non-uniform flexibility (section from $300-400\sigma$ is less flexible). $\kappa_{flex}=0$, $\kappa_{stiff}=5k_BT$ and x-length $=100\sigma$. The two knot-finding algorithms are compared: that which introduces closing sections ($\bigcirc$) and that which does not ($\times$).

In Fig. 9.2, we compare results for the two knot-finding algorithms, that which introduces closing sections, and that which does not. Larger differences between the two were observed for lower tensions. We plot results for an x-length of 100σ, the shortest simulation box used, because it has lower tension. As may be seen, whilst differences greater than the errors are apparent, the results are quantitatively very close and the same qualitative features are seen. Both methods have disadvantages: there is the possibility of errors when closing sections are used but if they are not then the position is less precise. The similarity of the results for both gives us confidence that they are reasonable. In all other figures, unless otherwise stated, results from the method that does not introduce closures are presented.

9.3 Results

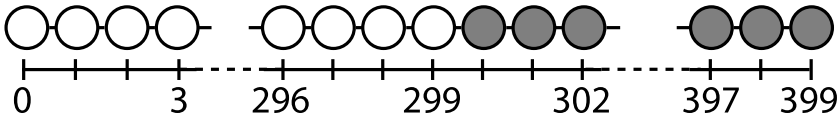


Figure 9.3: The division of the polymer into sections of different flexibility. For the open beads $\kappa_i = \kappa_{flex}$ and for grey-filled beads $\kappa_i = \kappa_{stiff}$. The beads are labelled as shown. Position along the polymer contour of the bead labelled i is taken to be $i \times \sigma$. Bead 399 is bonded to bead 0.

Typically, polymers of length $N = 400$ beads were used. κ_i in Eq. (9.1) was set to one lower value, κ_{flex}, usually for 300 of the beads (labelled 0 - 299) and to a single higher value, κ_{stiff}, for the remaining 100 (labelled 300 - 399). This situation is depicted in Fig. 9.3. In the following, the position of the i^{th} bead along the contour is taken to be $i \times \sigma$.

Errors were estimated by using the method of block averages [74] to find the correlation time for the knot position: as discussed in Chapter 6 the variance of the averages over blocks of a particular time is considered. Once this time is long enough that the averages are independent, the variance will be inversely proportional the number of blocks. The correlation time was typically on the order of 10^4 - $10^5 t_0$. The probability density for each bin was calculated over each correlation time and the standard error in the average of the resulting values taken. A total simulation time of $10^7 t_0$ was used for each set of parameters.

9.3.1 Varying Tension

We start by using $\kappa_{flex} = 0$ and $\kappa_{stiff} = 5k_BT$ and considering simulation boxes with x-lengths of 300σ, 200σ and 100σ. The average tension, τ, of the polymers due to the x-extension was measured by considering the force exerted by a bead on its neighbour in the x-direction. The measured τ were $4.2729 \pm 0.0003 k_BT/\sigma$ for 300σ,

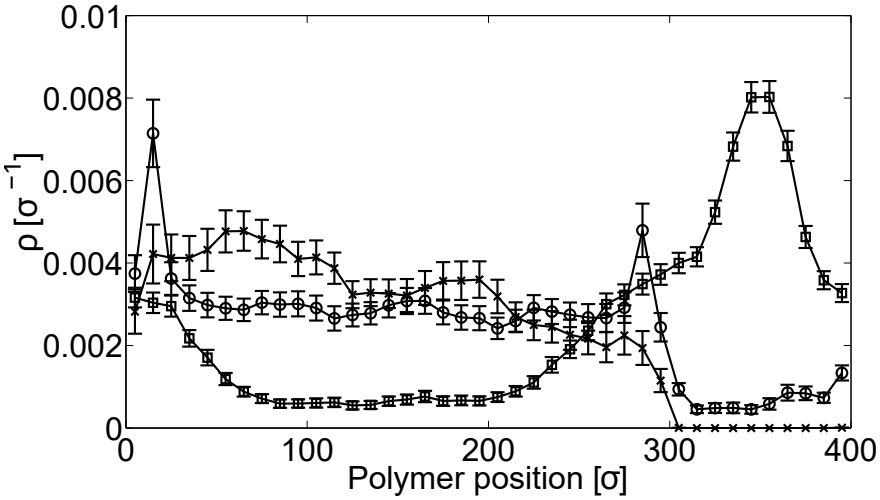


Figure 9.4: Probability density of finding a knot at different positions along a polymer of non-uniform flexibility (section from $300 - 400\sigma$ is less flexible). $\kappa_{flex} = 0$ and $\kappa_{stiff} = 5k_BT$. Results for three different x-lengths, giving three different measured tensions (τ), are shown: 300σ, $\tau = 4.2729 \pm 0.0003k_BT/\sigma$ ($\times$); 200σ, $\tau = 1.6169 \pm 0.0003k_BT/\sigma$ ($\bigcirc$); 100σ, $\tau = 0.7161 \pm 0.0007k_BT/\sigma$ ($\square$).

$1.6169 \pm 0.0003k_BT/\sigma$ for 200σ and $0.7161 \pm 0.0007k_BT/\sigma$ for 100σ. The tensions are thus around the crossover from the elastic regime to the blob regime [125], see also Chapter 6.

Results are plotted in Fig. 9.4. For the highest tension, the probability density for finding the knot within the stiffer section is identically zero – during the simulation the knot was never observed to enter this region. At the intermediate tension, the probability density in the stiffer section remains lower than that in the more flexible section but is non-zero. Two sharp peaks at the borders between the two sections may also clearly be seen. Finally, at the lowest tension, the situation is reversed and the probability density in the stiffer section is much higher. The probability density rises to a peak in the centre of the stiffer section but there are also shoulders at the borders, suggesting some propensity for the knots to be found at the boundaries remains.

9.3.2 Varying Flexibility

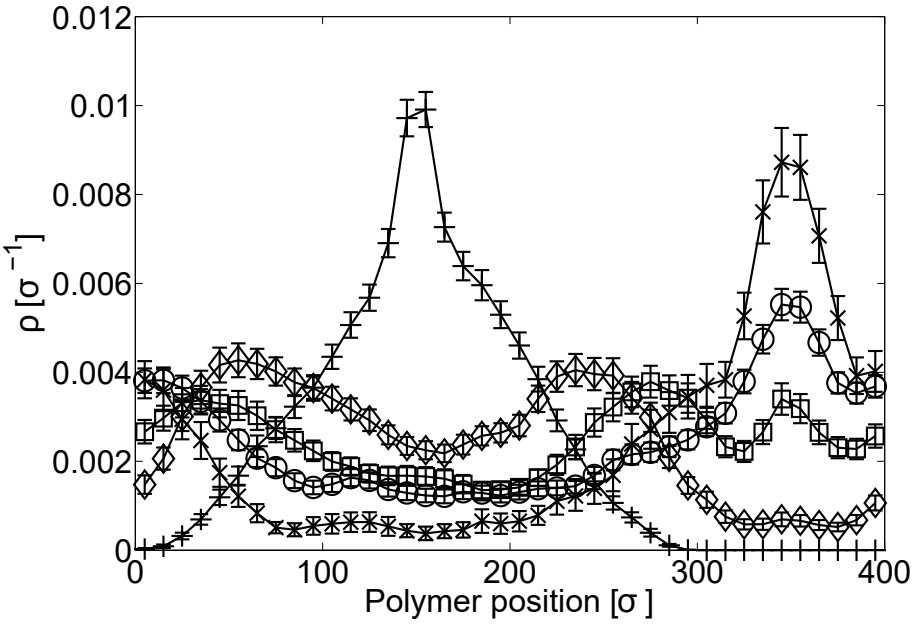


Figure 9.5: Probability density of finding a knot at different positions along a polymer of non-uniform flexibility (section from $300 - 400\sigma$ is less flexible). All simulations were performed with x-length $= 100\sigma$. All κ are in units of k_BT and all tensions, τ, are in units of k_BT/σ: $\kappa_{flex} = 0$, $\kappa_{stiff} = 5$, $\tau = 0.7161 \pm 0.0007$ ($\times$); $\kappa_{flex} = 1$, $\kappa_{stiff} = 5$, $\tau = 0.6535 \pm 0.0005$ ($\bigcirc$); $\kappa_{flex} = 1$, $\kappa_{stiff} = 7$, $\tau = 0.6462 \pm 0.0007$ ($\square$); $\kappa_{flex} = 1$, $\kappa_{stiff} = 10$, $\tau = 0.6348 \pm 0.0006$ ($\Diamond$); $\kappa_{flex} = 5$, $\kappa_{stiff} = 50$, $\tau = 0.5845 \pm 0.0007$ ($+$).

We again take x-length $= 100\sigma$, for which localisation in the less flexible part of the polymer was observed, see Fig. 9.4, and consider varying the values of κ_{flex} and κ_{stiff}. Results are shown in Fig. 9.5. The different flexibility did lead to changes in the measured tensions, which are given in the figure captions. The largest change in τ between any two parameter choices (with x-length $= 100\sigma$) was about 20%.

In Fig. 9.5, it may be seen that, if κ_{stiff} is held constant at $5k_BT$ and κ_{flex} is increased from 0 to $1k_BT$, then the qualitative shape of the distribution remains the same but the probability density in the stiff section decreases and that in the flexible section increases. Subsequently increasing κ_{stiff} to $7k_BT$ and $10k_BT$, it is seen that the probability density in the stiff section decreases further: the results

shown in Fig. 9.5 suggest that it is not just the relative sizes of κ_{flex} and κ_{stiff} that are important. For $\kappa_{stiff} = 7$ and $10k_BT$, it is seen that relatively broad peaks near the borders between the two sections appear. The results for $\kappa_{stiff} = 50k_BT$ show that if κ_{stiff} is increased sufficiently then the knot will be excluded entirely from the stiff section.

As discussed, changing κ_{flex} and κ_{stiff} does change the measured tension. This opens the question as to what extent the changes observed are due to the different flexibilities and to what extent they are due to the different tensions. The results show the general trend that as κ_{flex} and κ_{stiff} are increased, the probability density in the stiff section decreases. The measured tensions for higher κ_{flex} and κ_{stiff} are lower. Fig. 9.4 shows that lowering the tension tends to increase the probability density in the stiff section. So it seems likely that the changes observed are due to the changing flexibility and not the tension.

9.3.3 Varying Section Length

In Fig. 9.6, we consider varying the length of the rigid section, increasing it from the usual 100σ to 200σ and 300σ. The x-length of the system is kept at 100σ. Bending energies $\kappa_{flex} = 0$ and $\kappa_{stiff} = 5k_BT$ are used. As the length of the rigid section is increased, the probability density there remains higher than in the flexible section but the maximum value decreases.

9.3.4 Summary

To summarise, the results presented indicate that, depending on the flexibilities and tension, a knot in a polymer with a flexible and a stiff section may be found with higher probability in either, or near the boundaries between the two. In general, the probability of finding the knot in the stiff section is highest for lower tensions. The results depend on the particular stiffnesses, not just the difference. If the tension or

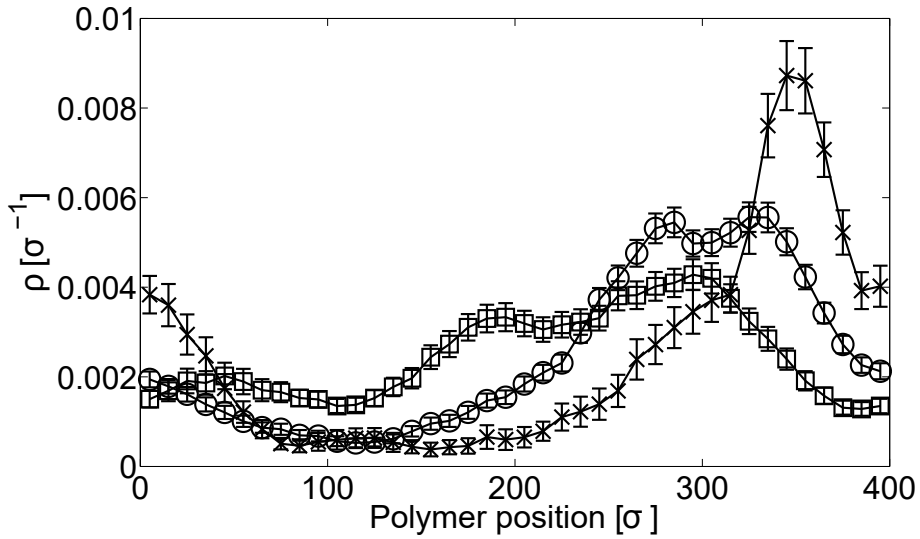


Figure 9.6: Probability density of finding a knot at different positions along a polymer of non-uniform flexibility, $\kappa_{flex} = 0k_BT$, $\kappa_{stiff} = 5k_BT$, x-length $= 100\sigma$. The extent of the rigid section is varied: $300 - 400\sigma$, tension, $\tau = 0.7161 \pm 0.0007k_BT/\sigma$ ($\times$); $200 - 400\sigma$, $\tau = 0.6581 \pm 0.0008k_BT/\sigma$ ($\bigcirc$); $100 - 400\sigma$, $\tau = 0.6113 \pm 0.0007k_BT/\sigma$ ($\square$).

the stiffness is sufficiently high, then the knot is never found in the stiff section.

9.3.5 Discussion

The probability density distributions observed will be determined by the underlying free-energy of the system. The important contributions are the bending energy of the polymer and its entropy. A rough picture of the situation may be developed using the concept of blobs, described in section A.1.5. Under tension, the polymer will form a series of blobs, each of which is like a smaller, free polymer, as depicted in Fig. 9.7. The blob size is determined by the tension, not the persistence length. The contour length of polymer in one blob will be less for a stiffer polymer (Fig. 9.7(a) compared to Fig. 9.7(b)). Assuming the knot remains in one blob and the blob size is not too large, then, since there is only weak knot localisation in a free polymer in a good solvent, the knot will take up most of that blob. The stiffer polymer, having less of

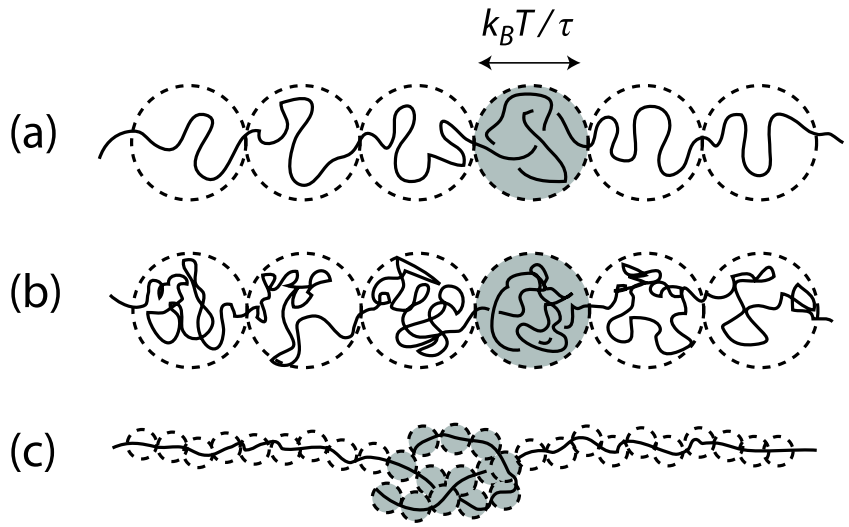


Figure 9.7: A polymer under tension forms a series of blobs within each of which it is as if free [192]. The blobs are indicated by the dashed circles. The typical size of a blob is set by the tension force, τ. (a) and (b) Polymers of different flexibility under the same tension are depicted. Since the blob size will be the same the contour length of the polymer in one blob will be lower for the stiffer polymer, (a), than the more flexible polymer, (b). Assuming the knot remains within one blob, indicated by the grey shading, its effect will be as if it were in a shorter, free polymer. (c) For a higher tension the blob size becomes smaller than the persistence length of the polymers of both flexibilities.

its contour entangled, will experience a lower entropic penalty for knotting. So in this regime it is favourable for the knot to be located in a stiffer (section of) polymer.

At high tensions or stiffness, the blob size will become less than the persistence length as depicted in Fig. 9.7(c). In this regime the bending energy will dominate and it will be preferable for the knot to be located in a more flexible (section of) polymer.

The above picture suggests that there are three important lengths: the two persistence lengths and the blob size set by the tension. It might thus be expected that if all are changed by the same factor, similar results will be seen. To test this, we compare results for $N = 400$ with $\kappa_{flex} = 1k_BT$ and $\kappa_{stiff} = 5k_BT$ to results for $N = 800$ with $\kappa_{flex} = 2k_BT$ and $\kappa_{stiff} = 10k_BT$: the persistence length is $\kappa\sigma/k_BT$, see section 3.1. In both cases, the final quarter of the polymer is the rigid section and an x-length of 100σ is used. This gives $\tau = 0.6535 \pm 0.0005k_BT/\sigma$ and $\tau = 0.2959 \pm 0.0005k_BT/\sigma$,

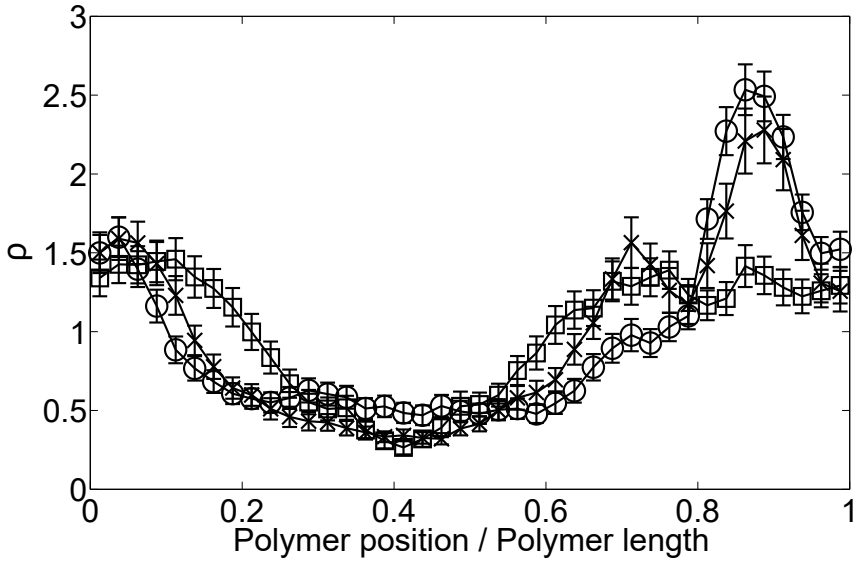


Figure 9.8: Probability density of finding a knot at different positions along a polymer of non-uniform flexibility. Results for polymers of length $N = 800$ found using the knot-finding algorithm with closures ($\times$), see Fig. 9.2, are compared to those found using the algorithm without closures ($\square$) and to those for $N = 400$ again using the algorithm with closures ($\bigcirc$). Further details of the parameters used may be found in the main text. Position along polymer is plotted as a ratio to the total polymer length.

for $N = 400$ and 800 respectively. The blob size $\sim k_B T/\tau$ and so is approximately double for $N = 800$.

Results are plotted in Fig. 9.8. It is seen that, for $N = 800$, there is a significant difference between the two knot-finding algorithms. With a longer polymer the probability of finding points where only one strand crosses the plane may be reduced, making the first method less accurate. The results from the algorithm that introduces closures are, however, seen to be very similar to the equivalent results for $N = 400$. This supports the suggestion that the behaviour is determined by the relative sizes of the three lengths although more investigation is required to properly establish this.

The interpretation suggested above clearly depends on the blob picture still being relevant for knotted polymers. As suggested in Chapter 4, this may not be the case. In order to better understand the the results presented, it is important to develop a

clearer idea of how to incorporate knots into the blob picture.

9.4 Further Work

It is possible that changing the probability with which knots reside in sections of DNA containing sites highly cleaved by topoisomerase II could change the frequency with which the enzyme passes strands. As discussed in section 2.2.2, each strand passage requires the hydrolysis of ATP, costing the cell energy, and so it would be advantageous to avoid it occurring unnecessarily. Our results suggest that it would be interesting to include variable flexibility in a model of a topoisomerase-DNA system to determine if similar effects could play a role.

The work we have performed so far is primarily exploratory. It would be interesting to investigate the various parameters much more thoroughly. It would also be interesting to see if simple scaling arguments may help explain the results. Key to achieving this may be, as suggested in subsection 9.3.5, to describe knotting with the blob picture. Further insight might be gained by applying a method, such as the one introduced by Schilling and Schmid [193], to calculate the free energies of polymers of different flexibility in a knotted state.

As discussed in section 9.2, the no tension case is difficult to analyse because of the relatively large knot size compared to the polymer size. One strategy might be to use much larger polymers such that knots become localised [31]. It might also be interesting to consider two-dimensional knots, for example in polymers absorbed on a surface, because, as discussed in section 2.4.3, in this case knots become strongly localised [31].

Another possibility that might give some insight into the no tension case would be to consider ring polymers of non-uniform flexibility and introduce a small phantom section – some beads that do not have excluded volume interactions with the rest

of the chain. This would allow the topology to change. It could be interesting to investigate how placing the phantom section at different positions compared to the more rigid section of the polymer affects how often the topology changes. As long as the phantom part were relatively small, it should not change the free-energy of the polymer greatly and so, assuming the system is ergodic, the overall rate of knotted configurations should be the same wherever the phantom beads were placed. Nevertheless, the results of this chapter suggest there would be a lower entropic penalty to forming a knot in the stiffer part of a polymer so it is reasonable to expect that the rate of knotting/unknotting might be higher when the phantom beads were there. Some simulations of such a system were run. It was found that there were relatively rare events where the polymer remained knotted for a 'long' time. It thus appeared that to properly sample the system very long simulations would be necessary. One approach to get around this could be to consider confining the polymers, which might increase the rate of the 'rare' events. This would also change the free-energy of the polymer and make the interpretation of the results more difficult: the confinement would introduce an additional length and complicate the system.

Simulations with a phantom section have the advantage that only the overall topology of the polymer need be considered. Similar approaches have been previously applied to the modelling of topoisomerase II [33], so it could be a first step towards a more biologically realistic model.

Chapter 10

Summary

This thesis used coarse-grained simulation models to investigate the dynamics and properties of knotted polymers and filaments. The first three chapters provided background and some details of techniques. The following six each considered a specific problem.

Introduction to, and motivation for, the problems considered was given in Chapter 1, as well as an overview of the remainder of the thesis. Chapter 2 gave background information about knots: previous work was discussed, as well as key concepts for description and understanding. Chapter 3 described the simulation models and methods that were used in later chapters, as well as other alternatives.

Chapter 4, looked at knotted polymers confined in a slit. We found that in relatively wide slits knots decrease the force exerted on the walls, while for narrower slits they increase it. This was linked to the effect of the knot on the ability of the polymer to spread out in the free directions: the constraints of more complex knots reduce the amount of spreading and consequently increase the monomer density at the walls.

Chapter 5 presented results for simulations of knotted polymers migrating through a designed channel with sections of two different widths under an electric field. Remi-

niscent of results from Chapter 4, we found that mobility changes with knot complexity in different ways depending on the narrower width. Generally, bigger differences in mobility were seen for lower fields, although they must be sufficiently high that all knots migrate. The trends seen showed qualitative similarities to knotted DNA gel-electrophoresis results. The possibility that entropic trapping could play a role in such experiments was discussed. We found evidence that the changes in mobility are due to the effect of the knot on the transition probability for an attempt by the polymer to move into a narrower section to be successful. We suggested that such channels could be used for the separation of DNA according to knot type.

In Chapter 6, we employed a new method for putting polymers under tension to investigate the behaviour of knots in them. We focussed on how topology affects the behaviour by considering two knot groups. Evidence to support a reptation picture was found. We found effective friction coefficients that showed a clear difference between the groups. An explanation in terms of topological features was given. The relaxation of the knots was investigated and time-scales that differed between the groups and increased with knot complexity were found. Comparisons to the dependence of relaxation time-scales on knot complexity in previous work on polymers without tension were made. We identified modes of knot deformation. One was found to determine the relaxation. Again, differences between the groups were rationalised in terms of topological features.

Chapter 7 investigated the dynamics of knotted filaments in simple shear, proposing such objects as an interesting new example of deformable objects for study in such flows. Initially, simulations using a relatively simple model were performed. We found rich behaviour, with the filaments of a particular flexibility displaying various different modes of motion. The modes show migration in the vorticity direction. We proposed a dimensionless parameter to determine when the knot will be tightened by the flow as the filament is made more deformable. In later sections, issues with the

model were discussed and a more sophisticated approach was introduced. Results for the new model for knotted filaments were found to be qualitatively similar. In comparison with other models, the results for linear filaments showed reasonably good agreement with experiment.

Chapter 8 considered the effect of knots on the ejection of a polymer from a capsid. This work was motivated by experiments that found high probabilities of knotting for DNA confined within bacteriophage capsids. We considered ejection of flexible and semi-flexible knotted polymers. The polymer ejection rate was found to be primarily controlled by the knot, which moves to the hole in the capsid and then acts as a ratchet. Polymers with more complex knots eject more slowly and, for large knots, the knot type, and not the flexibility of the polymer, determines the rate of ejection.

Chapter 9 looked at knots in polymers of non-uniform flexibility under tension. It was found that changing the flexibility or tension can change whether the knot is found with higher probability in a stiffer or a more flexible section. We proposed that the results might be explained using a blob-type picture and that the behaviour is determined by the relative sizes of three key length-scales.

Many ideas for further study based on specific problems are given in the final sections of the relevant chapters.

Bibliography

[1] M. Doi and S.F. Edwards. *The Theory of Polymer Dynamics*. Oxford University Press, Oxford, 1986.

[2] J.M. Berg, J.L. Tymoczko, and L. Stryer. *Biochemistry, Fifth Edition*. W. H. Freeman and Co., New York, 2002.

[3] P.J. Hagerman. Flexibility of DNA. *Annual Review of Biophysics and Biophysical Chemistry*, **17**(1):265, 1988.

[4] F.B. Fuller. Decomposition of the linking number of a closed ribbon: A problem from molecular biology. *Proceedings of the National Academy of Sciences*, **75**(8):3557, 1978.

[5] A. Stasiak, V. Katritch, J. Bednar, D. Michoud, and J. Dubochet. Electrophoretic mobility of DNA knots. *Nature*, **384**(6605):122, 1996.

[6] S.B. Smith, L. Finzi, and C. Bustamante. Direct mechanical measurements of the elasticity of single DNA molecules by using magnetic beads. *Science*, **258**(5085):1122, 1992.

[7] D.E. Smith, H.P. Babcock, and S. Chu. Single-polymer dynamics in steady shear flow. *Science*, **283**(5408):1724, 1999.

[8] A. Meller, L. Nivon, and D. Branton. Voltage-driven DNA translocations through a nanopore. *Physical Review Letters*, **86**(15):3435, 2001.

[9] D.E. Smith, T.T. Perkins, and S. Chu. Dynamical scaling of DNA diffusion coefficients. *Macromolecules*, **29**(4):1372, 1996.

[10] W.D. Volkmuth and R.H. Austin. DNA electrophoresis in microlithographic arrays. *Nature*, **358**(6387):600, 1992.

[11] O.L. Forgacs and S.G. Mason. Particle motions in sheared suspensions X. Orbits of flexible threadlike particles. *Journal of Colloid Science*, **14**(5):473, 1959.

[12] O.L. Forgacs and S.G. Mason. Particle motions in sheared suspensions IX. Spin and deformation of threadlike particles. *Journal of Colloid Science*, **14**(5):457, 1959.

[13] M.V. D'Angelo, B. Semin, G. Picard, M.E. Poitzsch, J.P. Hulin, and H. Auradou. Single Fiber Transport in a Fracture Slit: Influence of the Wall Roughness and of the Fiber Flexibility. *Transport in Porous Media*, page 1, 2009.

[14] S.L. Biswal and A.P. Gast. Rotational dynamics of semiflexible paramagnetic particle chains. *Physical Review E*, **69**(4):41406, 2004.

[15] B. Herzhaft, É. Guazzelli, M.B. Mackaplow, and E.S.G. Shaqfeh. Experimental investigation of the sedimentation of a dilute fiber suspension. *Physical Review Letters*, **77**(2):290, 1996.

[16] Sir W. Thomson and Baron Kelvin. On Vortex Atoms; On Vortex Motion; Vortex Statics. In *Knots and Applications*, page 111. World Scientific, Singapore, 1995.

[17] P.G. Tait. On Knots, Part II. *Transactions of the Royal Society of Edinburgh*, **32**:327, 1884.

[18] E. Witten. Quantum field theory and the Jones polynomial. *Communications in Mathematical Physics*, **121**(3):351, 1989.

[19] E. Orlandini and S.G. Whittington. Statistical topology of closed curves: Some applications in polymer physics. *Reviews of Modern Physics*, **79**(2):611, 2007.

[20] D.W. Sumners and S.G. Whittington. Knots in self-avoiding walks. *Journal of Physics A: Mathematical and General*, **21**:1689, 1988.

[21] H.E. Kubitschek. Cell volume increase in Escherichia coli after shifts to richer media. *Journal of Bacteriology*, **172**(1):94, 1990.

[22] R. Reyes-Lamothe, C. Possoz, O. Danilova, and D.J. Sherratt. Independent positioning and action of Escherichia coli replisomes in live cells. *Cell*, **133**(1):90, 2008.

[23] J.P.J. Michels and F.W. Wiegel. On the topology of a polymer ring. *Proceedings of the Royal Society of London. A*, **403**:269, 1986.

[24] J.M. Sogo, A. Stasiak, M.L. Martínez-Robles, D.B. Krimer, P. Hernández, and J.B. Schvartzman. Formation of knots in partially replicated DNA molecules. *Journal of Molecular Biology*, **286**(3):637, 1999.

[25] P.M. Watt and I.D. Hickson. Structure and function of type II DNA topoisomerases. *Biochemical Journal*, **303**(Pt 3):681, 1994.

[26] J. Portugal and A. Rodriguez-Campos. T7 RNA polymerase cannot transcribe through a highly knotted DNA template. *Nucleic Acids Research*, **24**(24):4890, 1996.

[27] D.W. Sumners. Lifting the Curtain: Using Topology to Probe the Hidden Action of Enzymes. *Notices of the AMS*, **42**, 1995.

[28] J. Arsuaga, M. Vázquez, S. Trigueros, D.W. Sumners, and J. Roca. Knotting probability of DNA molecules confined in restricted volumes: DNA knotting in phage capsids. *Proceedings of the National Academy of Sciences*, **99**(8):5373, 2002.

[29] S.R. Quake. Topological effects of knots in polymers. *Physical Review Letters*, **73**(24):3317, 1994.

[30] V.V. Rybenkov, N.R. Cozzarelli, and A.V. Vologodskii. Probability of DNA knotting and the effective diameter of the DNA double helix. *Proceedings of the National Academy of Sciences*, **90**(11):5307, 1993.

[31] E. Orlandini, A.L. Stella, and C. Vanderzande. The size of knots in polymers. *Physical Biology*, **6**:025012, 2009.

[32] X.R. Bao, H.J. Lee, and S.R. Quake. Behavior of complex knots in single DNA molecules. *Physical Review Letters*, **91**(26):265506, 2003.

[33] A.V. Vologodskii, W. Zhang, V.V. Rybenkov, A.A. Podtelezhnikov, D. Subramanian, J.D. Griffith, and N.R. Cozzarelli. Mechanism of topology simplification by type II DNA topoisomerases. *Proceedings of the National Academy of Sciences*, **98**(6):3045, 2001.

[34] C. Livingston. *Knot Theory*. The Mathematical Association of America, Washington, 1993.

[35] L.H. Kauffman. *Knots and Physics*. World Scientific, Singapore, 1993.

[36] J.W. Alexander and G.B. Briggs. On types of knotted curves. *Annals of Mathematics*, **28**(1):562, 1926.

[37] D. Rolfsen. *Knots and Links*. Publish or Perish, Houston, 1976.

[38] J. Hoste, M. Thistlethwaite, and J. Weeks. The first 1,701,936 knots. *The Mathematical Intelligencer*, **20**(4):33, 1998.

[39] N.J. Crisona, R.L. Weinberg, B.J. Peter, D.W. Sumners, and N.R. Cozzarelli. The Topological Mechanism of Phage λ Integrase. *Journal of Molecular Biology*, **289**(4):747, 1999.

[40] M. Solymosi, R.J. Low, M. Grayson, and M.P. Neal. A generalized scaling of a chiral index for molecules. *The Journal of Chemical Physics*, **116**:9875, 2002.

[41] J.W. Alexander. Topological invariants of knots and links. *Transactions of the American Mathematical Society*, **30**(2):275, 1928.

[42] A. Stasiak, V. Katritch, and L.H. Kauffman. *Ideal Knots*. World Scientific, Singapore, 1998.

[43] S.A. Wasserman and N.R. Cozzarelli. Biochemical topology: applications to DNA recombination and replication. *Science*, **232**(4753):951, 1986.

[44] J.J. Champoux. DNA Topoisomerases: Structure, Function, and Mechanism. *Annual Review of Biochemistry*, **70**(1):369, 2001.

[45] Y. Pommier. DNA topoisomerase I and II in cancer chemotherapy: update and perspectives. *Cancer chemotherapy and Pharmacology*, **32**(2):103, 1993.

[46] D.A. Burden and N. Osheroff. In vitro evolution of preferred topoisomerase II DNA cleavage sites. *Journal of Biological Chemistry*, **274**(8):5227, 1999.

[47] L. Postow, B.J. Peter, and N.R. Cozzarelli. Knot what we thought before: the twisted story of replication. *Bioessays*, **21**(10):805, 1999.

[48] L. Olavarrieta, M.L. Martinez-Robles, P. Hernandez, D.B. Krimer, and J.B. Schvartzman. Knotting dynamics during DNA replication. *Molecular Microbiology*, **46**(3):699, 2002.

[49] V.V. Rybenkov, C. Ullsperger, A.V. Vologodskii, and N.R. Cozzarelli. Simplification of DNA topology below equilibrium values by type II topoisomerases. *Science*, **277**(5326):690, 1997.

[50] K.C. Dong and J.M. Berger. Structural basis for gate-DNA recognition and bending by type IIA topoisomerases. *Nature*, **450**(7173):1201, 2007.

[51] G. Witz and A. Stasiak. DNA supercoiling and its role in DNA decatenation and unknotting. *Nucleic Acids Research*, **38**(7):2119, 2010.

[52] W.R. Taylor. A deeply knotted protein structure and how it might fold. *Nature*, **406**(6798):916, 2000.

[53] P. Virnau, L.A. Mirny, and M. Kardar. Intricate knots in proteins: function and evolution. *PLoS Comput Biol*, **2**(9):e122, 2006.

[54] A.V. Vologodskii, N.J. Crisona, B. Laurie, P. Pieranski, V. Katritch, J. Dubochet, and A. Stasiak. Sedimentation and electrophoretic migration of DNA knots and catenanes. *Journal of Molecular Biology*, **278**(1):1, 1998.

[55] J.L. Viovy. Electrophoresis of DNA and other polyelectrolytes: Physical mechanisms. *Reviews of Modern Physics*, **72**(3):813, 2000.

[56] G. Buck and E.J. Rawdon. Role of flexibility in entanglement. *Physical Review E*, **70**(1):11803, 2004.

[57] R. Gallotti and O. Pierre-Louis. Stiff knots. *Physical Review E*, **75**(3):31801, 2007.

[58] O. Gonzalez, A.B.A. Graf, and J.H. Maddocks. Dynamics of a rigid body in a Stokes fluid. *Journal of Fluid Mechanics*, **519**:133, 2004.

[59] M. Carlen, P. Caussignac, and J.H. Maddocks. Simulation of the Stokesian sedimentation of ideal knots with a boundary element method. Preprint, 2009.

[60] S.Y. Shaw and J.C. Wang. Knotting of a DNA chain during ring closure. *Science*, **260**(5107):533, 1993.

[61] M.C. Tesi, E.J. Janse van Rensburg, E. Orlandini, and S.G. Whittington. Knot probability for lattice polygons in confined geometries. *Journal of Physics A: Mathematical and General*, **27**:347, 1994.

[62] J. Arsuaga, M. Vázquez, P. McGuirk, S. Trigueros, D.W. Sumners, and J. Roca. DNA knots reveal a chiral organization of DNA in phage capsids. *Proceedings of the National Academy of Sciences*, **102**(26):9165, 2005.

[63] Y. Arai, R. Yasuda, K. Akashi, Y. Harada, H. Miyata, K. Kinosita, and H. Itoh. Tying a molecular knot with optical tweezers. *Nature*, **399**(6735):446, 1999.

[64] P.Y. Lai. Dynamics of polymer knots at equilibrium. *Physical Review E*, **66**(2):21805, 2002.

[65] E. Orlandini, A.L. Stella, C. Vanderzande, and F. Zonta. Slow topological time scale of knotted polymers. *Journal of Physics A: Mathematical and Theoretical*, **41**:122002, 2008.

[66] Y.J. Sheng, P.Y. Lai, and H.K. Tsao. Deformation of a stretched polymer knot. *Physical Review E*, **61**(3):2895, 2000.

[67] P.Y. Lai, Y.J. Sheng, and H.K. Tsao. Nonequilibrium relaxation times in polymer knot groups. *Physical Review Letters*, **87**(17):175503, 2001.

[68] R. Metzler, A. Hanke, P.G. Dommersnes, Y. Kantor, and M. Kardar. Equilibrium shapes of flat knots. *Physical Review Letters*, **88**(18):188101, 2002.

[69] E. Ercolini, F. Valle, J. Adamcik, G. Witz, R. Metzler, P. De Los Rios, J. Roca, and G. Dietler. Fractal dimension and localization of DNA knots. *Physical Review Letters*, **98**(5):58102, 2007.

[70] O. Farago, Y. Kantor, and M. Kardar. Pulling knotted polymers. *Europhysics Letters*, **60**:53, 2002.

[71] B. Marcone, E. Orlandini, A.L. Stella, and F. Zonta. What is the length of a knot in a polymer? *Journal of Physics A: Mathematical and General*, **38**:L15, 2005.

[72] B. Berg and D. Foerster. Random paths and random surfaces on a digital computer. *Physics Letters B*, **106**(4):323, 1981.

[73] M. Tsige, J.G. Curro, G.S. Grest, and J.D. McCoy. Molecular dynamics simulations and integral equation theory of alkane chains: comparison of explicit and united atom models. *Macromolecules*, **36**(6):2158, 2003.

[74] D. Frenkel and B. Smit. *Understanding Molecular Simulation: from Algorithms to Applications*. Academic Press, London, 2002.

[75] D. Lucent, V. Vishal, and V.S. Pande. Protein folding under confinement: A role for solvent. *Proceedings of the National Academy of Sciences*, **104**(25):10430, 2007.

[76] I. Carmesin and K. Kremer. The bond fluctuation method: a new effective algorithm for the dynamics of polymers in all spatial dimensions. *Macromolecules*, **21**(9):2819, 1988.

[77] H.P. Hsu and P. Grassberger. Polymers confined between two parallel plane walls. *The Journal of Chemical Physics*, **120**:2034, 2004.

[78] H.R. Warner Jr. Kinetic theory and rheology of dilute suspensions of finitely extendible dumbbells. *Industrial & Engineering Chemistry Fundamentals*, **11**(3):379, 1972.

[79] G.S. Grest and K. Kremer. Molecular dynamics simulation for polymers in the presence of a heat bath. *Physical Review A*, **33**(5):3628, 1986.

[80] M. Streek, F. Schmid, T.T. Duong, and A. Ros. Mechanisms of DNA separation in entropic trap arrays: a Brownian dynamics simulation. *Journal of Biotechnology*, **112**:79, 2004.

[81] M. Bulacu and E. van der Giessen. Effect of bending and torsion rigidity on self-diffusion in polymer melts: A molecular-dynamics study. *The Journal of Chemical Physics*, **123**:114901, 2005.

[82] G. Chirico and J. Langowski. Kinetics of DNA supercoiling studied by Brownian dynamics simulation. *Biopolymers*, **34**(3):415, 1994.

[83] T.R. Powers. Dynamics of filaments and membranes in a viscous fluid. *Reviews of Modern Physics*, **82**(2):1607, 2010.

[84] K. Kremer and K. Binder. Monte Carlo simulation of lattice models for macromolecules. *Computer Physics Reports*, **7**(6):259, 1988.

[85] J. Rotne and S. Prager. Variational treatment of hydrodynamic interaction in polymers. *The Journal of Chemical Physics*, **50**:4831, 1969.

[86] D.J. Jeffrey and Y. Onishi. Calculation of the resistance and mobility functions for two unequal rigid spheres in low-Reynolds-number flow. *Journal of Fluid Mechanics*, **139**:261, 1984.

[87] L. Durlofsky, J.F. Brady, and G. Bossis. Dynamic simulation of hydrodynamically interacting particles. *Journal of Fluid Mechanics*, **180**:21, 1987.

[88] P. Ahlrichs and B. Dünweg. Simulation of a single polymer chain in solution by combining lattice Boltzmann and molecular dynamics. *The Journal of Chemical Physics*, **111**:8225, 1999.

[89] O.B. Usta, A.J.C. Ladd, and J.E. Butler. Lattice-Boltzmann simulations of the dynamics of polymer solutions in periodic and confined geometries. *The Journal of Chemical Physics*, **122**:094902, 2005.

[90] A. Malevanets and R. Kapral. Mesoscopic model for solvent dynamics. *The Journal of Chemical Physics*, **110**:8605, 1999.

[91] D.S. Lemons and A. Gythiel. Paul Langevin′s 1908 paper On the Theory of Brownian Motion[Sur la théorie du mouvement brownien, C. R. Acad. Sci. (Paris) 146, 530–533 (1908)]. *American Journal of Physics*, **65**:1079, 1997.

[92] D.L. Ermak. A computer simulation of charged particles in solution. I. Technique and equilibrium properties. *The Journal of Chemical Physics*, **62**:4189, 1975.

[93] E. Gauger and H. Stark. Numerical study of a microscopic artificial swimmer. *Physical Review E*, **74**(2):21907, 2006.

[94] D.L. Ermak and J.A. McCammon. Brownian dynamics with hydrodynamic interactions. *The Journal of Chemical Physics*, **69**:1352, 1978.

[95] M. Fixman. Construction of Langevin forces in the simulation of hydrodynamic interaction. *Macromolecules*, **19**:1204, 1986.

[96] M. Ripoll, K. Mussawisade, R.G. Winkler, and G. Gompper. Low-Reynolds-number hydrodynamics of complex fluids by multi-particle-collision dynamics. *Europhysics Letters*, **68**:106, 2004.

[97] H. Noguchi and G. Gerhard. Swinging and Tumbling of Fluid Vesicles in Shear Flow. *Physical Review Letters*, **98**(12):128103, 2007.

[98] D.J. Earl, C.M. Pooley, J.F. Ryder, I. Bredberg, and J.M. Yeomans. Modeling microscopic swimmers at low Reynolds number. *The Journal of Chemical Physics*, **126**:064703, 2007.

[99] T. Ihle and D. M. Kroll. Stochastic rotation dynamics: A galilean-invariant mesoscopic model for fluid flow. *Physical Review E*, **63**(2):020201, 2001.

[100] J.T. Padding and A.A. Louis. Hydrodynamic interactions and Brownian forces in colloidal suspensions: Coarse-graining over time and length scales. *Physical Review E*, **74**(3):31402, 2006.

[101] N. Kikuchi, C.M. Pooley, J.F. Ryder, and J.M. Yeomans. Transport coefficients of a mesoscopic fluid dynamics model. *The Journal of Chemical Physics*, **119**:6388, 2003.

[102] K. Mussawisade, M. Ripoll, R.G. Winkler, and G. Gompper. Dynamics of polymers in a particle-based mesoscopic solvent. *The Journal of Chemical Physics*, **123**:144905, 2005.

[103] W.J. Closs, B.R. Jennings, and H.G. Jerrard. Sedimentation velocity of polymer solutions–I. Concentration dependence of the sedimentation coefficient. *European Polymer Journal*, **4**(6):639, 1968.

[104] M. Daoud and P.G. de Gennes. Statistics of macromolecular solutions trapped in small pores. *Journal de Physique*, **38**(1):85, 1977.

[105] I. Webman, J.L. Lebowitz, and M.H. Kalos. Monte-Carlo studies of a polymer between planes, crossover between dimensionalities. *Journal de Physique*, **41**(6):579, 1980.

[106] E. Eisenriegler. Universal density-force relations for polymers near a repulsive wall. *Physical Review E*, **55**(3):3116, 1997.

[107] D.I. Dimitrov, A. Milchev, K. Binder, L.I. Klushin, and A.M. Skvortsov. Universal properties of a single polymer chain in slit: Scaling versus molecular dynamics simulations. *The Journal of Chemical Physics*, **128**:234902, 2008.

[108] R. Brak, A.L. Owczarek, A. Rechnitzer, and S.G. Whittington. A directed walk model of a long chain polymer in a slit with attractive walls. *Journal of Physics A: Mathematical and General*, **38**:4309, 2005.

[109] E.J. Janse van Rensburg. Squeezing knots. *Journal of Statistical Mechanics: Theory and Experiment*, **3**:1, 2007.

[110] E.J. Rawdon, J.C. Kern, M. Piatek, P. Plunkett, A. Stasiak, and K.C. Millett. Effect of Knotting on the Shape of Polymers. *Macromolecules*, **41**(21):8281, 2008.

[111] K.C. Millett, P. Plunkett, M. Piatek, E.J. Rawdon, and A. Stasiak. Effect of knotting on polymer shapes and their enveloping ellipsoids. *The Journal of Chemical Physics*, **130**:165104, 2009.

[112] E. Arvanitidou and D. Hoagland. Chain-length dependence of the electrophoretic mobility in random gels. *Physical Review Letters*, **67**(11):1464, 1991.

[113] S. Trigueros, J. Arsuaga, M.E. Vazquez, D.W. Sumners, and J. Roca. Novel display of knotted DNA molecules by two-dimensional gel electrophoresis. *Nucleic Acids Research*, **29**(13):e67, 2001.

[114] C. Weber, A. Stasiak, P. De Los Rios, and G. Dietler. Numerical simulation of gel electrophoresis of DNA knots in weak and strong electric fields. *Biophysical Journal*, **90**(9):3100, 2006.

[115] U. Alon and D. Mukamel. Gel electrophoresis and diffusion of ring-shaped DNA. *Physical Review E*, **55**(2):1783, 1997.

[116] J. Han, S.W. Turner, and H.G. Craighead. Entropic trapping and escape of long DNA molecules at submicron size constriction. *Physical Review Letters*, **83**(8):1688, 1999.

[117] J. Han and H.G. Craighead. Separation of long DNA molecules in a microfabricated entropic trap array. *Science*, **288**(5468):1026, 2000.

[118] T. Sakaue. DNA electrophoresis in designed channels. *The European Physical Journal E: Soft Matter and Biological Physics*, **19**(4):477, 2006.

[119] F. Tessier, J. Labrie, and G.W. Slater. Electrophoretic separation of long polyelectrolytes in submolecular-size constrictions: a Monte Carlo study. *Macromolecules*, **35**(12):4791, 2002.

[120] M. Streek, F. Schmid, T.T. Duong, D. Anselmetti, and A. Ros. Two-state migration of DNA in a structured microchannel. *Physical Review E*, **71**(1):11905, 2005.

[121] E.B. Cummings, S.K. Griffiths, R.H. Nilson, and P.H. Paul. Conditions for similitude between the fluid velocity and electric field in electroosmotic flow. *Analytical Chemistry*, **72**(11):2526, 2000.

[122] J. Smiatek and F. Schmid. Polyelectrolyte electrophoresis in nanochannels: a dissipative particle dynamics simulation. *The Journal of Physical Chemistry B*, **114**(19):6266, 2010.

[123] K.F. Riley, M.P. Hobson, and S.J. Bence. *Mathematical Methods for Physics and Engineering*. Cambridge University Press, Cambridge, 1998.

[124] L.F. Liu, R.E. Depew, and J.C. Wang. Knotted single-stranded DNA rings: A novel topological isomer of circular single-stranded DNA formed by treatment with *Escherichia coli* ω protein. *Journal of Molecular Biology*, **106**(2):439, 1976.

[125] L. Huang and D.E. Makarov. Langevin dynamics simulations of the diffusion of molecular knots in tensioned polymer chains. *The Journal of Physical Chemistry. A*, **111**(41):10338, 2007.

[126] A. Vologodskii. Brownian dynamics simulation of knot diffusion along a stretched DNA molecule. *Biophysical Journal*, **90**(5):1594, 2006.

[127] A.Y. Grosberg, A. Feigel, and Y. Rabin. Flory-type theory of a knotted ring polymer. *Physical Review E*, **54**(6):6618, 1996.

[128] A. Malevanets and J.M. Yeomans. Dynamics of short polymer chains in solution. *Europhysics Letters*, **52**:231, 2000.

[129] Z. Liu, R.W. Deibler, H.S. Chan, and L. Zechiedrich. The why and how of DNA unlinking. *Nucleic Acids Research*, **37**(3):661, 2009.

[130] R. Metzler, W. Reisner, R. Riehn, R. Austin, J.O. Tegenfeldt, and I.M. Sokolov. Diffusion mechanisms of localised knots along a polymer. *Europhysics Letters*, **76**:696, 2006.

[131] W. Möbius, E. Frey, and U. Gerland. Spontaneous unknotting of a polymer confined in a nanochannel. *Nano Letters*, **8**(12):4518, 2008.

[132] G.B. Jeffrey. The Motion of Ellipsoidal Particles Immersed in a Viscous Fluid. *Proceedings of the The Royal Society of London. A*, **102**:161, 1922.

[133] J.M. Rallison. The deformation of small viscous drops and bubbles in shear flows. *Annual Review of Fluid Mechanics*, **16**(1):45, 1984.

[134] H. Schmid-Schönbein and R. Wells. Fluid drop-like transition of erythrocytes under shear. *Science*, **165**(3890):288, 1969.

[135] M. Ripoll, R. G. Winkler, and G. Gompper. Star Polymers in Shear Flow. *Physical Review Letters*, **96**(18):188302, 2006.

[136] E.S.G. Shaqfeh. The dynamics of single-molecule DNA in flow. *Journal of Non-Newtonian Fluid Mechanics*, **130**(1):1, 2005.

[137] S.B. Lindström and T. Uesaka. Simulation of the motion of flexible fibers in viscous fluid flow. *Physics of Fluids*, **19**:113307, 2007.

[138] H. Kobayashi and R. Yamamoto. Tumbling motion of a single chain in shear flow: a crossover from Brownian to non-Brownian behavior. *Physical Review E*, **81**(4):41807, 2010.

[139] N. Watari and R.G. Larson. Shear-Induced Chiral Migration of Particles with Anisotropic Rigidity. *Physical Review Letters*, **102**(24):246001, 2009.

[140] Y.J. Kim and W.J. Rae. Separation of screw-sensed particles in a homogeneous shear field. *International Journal of Multiphase Flow*, **17**(6):717, 1991.

[141] Marcos, H.C. Fu, T.R. Powers, and R. Stocker. Separation of microscale chiral objects by shear flow. *Physical Review Letters*, **102**(15):158103, 2009.

[142] R.G. Cox. The motion of long slender bodies in a viscous fluid part 1. General theory. *Journal of Fluid Mechanics*, **44**(04):791, 1970.

[143] C.P. Lowe. Dynamics of filaments: modelling the dynamics of driven microfilaments. *Philosophical Transactions of the Royal Society of London. Series B: Biological Sciences*, **358**(1437):1543, 2003.

[144] S. Yamamoto and T. Matsuoka. A method for dynamic simulation of rigid and flexible fibers in a flow field. *The Journal of Chemical Physics*, **98**:644, 1993.

[145] C. Grebogi, E. Ott, and J.A. Yorke. Chaotic attractors in crisis. *Physical Review Letters*, **48**(22):1507, 1982.

[146] Animations are available with the online version of the paper, R. Matthews, A.A. Louis and J.M. Yeomans. Complex dynamics of knotted filaments in shear flow, *EPL,* **92**: 34003, 2010. The paper is available via the website `http://iopscience.iop.org/0295-5075`. The animations were created using VMD: W. Humphrey, A. Dalke and K. Schulten, VMD - Visual Molecular Dynamics, *Journal of Molecular Graphics*, **14**(1):33, 1996.

[147] A.J. Lichtenberg and M.A. Lieberman. *Regular and Stochastic Motion*. Springer-Verlag, Berlin, 1983.

[148] M.J. Feigenbaum. Quantitative universality for a class of nonlinear transformations. *Journal of Statistical Physics*, **19**(1):25, 1978.

[149] Y. Pomeau and P. Manneville. Intermittent transition to turbulence in dissipative dynamical systems. *Communications in Mathematical Physics*, **74**(2):189, 1980.

[150] A.M. Stuart and A.R. Humphries. *Dynamical Systems and Numerical Analysis*. Cambridge University Press, Cambridge, 1998.

[151] C. Grebogi, E. Ott, and J.A. Yorke. Fractal basin boundaries, long-lived chaotic transients, and unstable-unstable pair bifurcation. *Physical Review Letters*, **50**(13):935, 1983.

[152] B. Carrasco and J.G. de la Torre. Improved hydrodynamic interaction in macromolecular bead models. *The Journal of Chemical Physics*, **111**:4817, 1999.

[153] R.F. Goldstein. Macromolecular diffusion constants: A calculational strategy. *The Journal of Chemical Physics*, **83**:2390, 1985.

[154] G. D'Avino, M.A. Hulsen, F. Snijkers, J. Vermant, F. Greco, and P.L. Maffettone. Rotation of a sphere in a viscoelastic liquid subjected to shear flow. Part I: Simulation results. *Journal of Rheology*, **52**:1331, 2008.

[155] K. Klenin and J. Langowski. Computation of writhe in modeling of supercoiled DNA. *Biopolymers*, **54**(5):307, 2000.

[156] P. Skjetne, R.F. Ross, and D.J. Klingenberg. Simulation of single fiber dynamics. *The Journal of Chemical Physics*, **107**(6):2108, 1997.

[157] L.E. Becker and M.J. Shelley. Instability of elastic filaments in shear flow yields first-normal-stress differences. *Physical Review Letters*, **87**(19):198301, 2001.

[158] I.O. Götze, H. Noguchi, and G. Gompper. Relevance of angular momentum conservation in mesoscale hydrodynamics simulations. *Physical Review E*, **76**(4):046705, 2007.

[159] J. Böhm, O. Lambert, A.S. Frangakis, L. Letellier, W. Baumeister, and J.L. Rigaud. FhuA-mediated phage genome transfer into liposomes: A cryo-electron tomography study. *Current Biology*, **11**(15):1168, 2001.

[160] S. Mangenot, M. Hochrein, J. Rädler, and L. Letellier. Real-time imaging of DNA ejection from single phage particles. *Current Biology*, **15**(5):430, 2005.

[161] P. Grayson, L. Han, T. Winther, and R. Phillips. Real-time observations of single bacteriophage λ DNA ejections *in vitro*. *Proceedings of the National Academy of Sciences*, **104**(37):14652, 2007.

[162] M. de Frutos, L. Letellier, and E. Raspaud. DNA ejection from bacteriophage T5: Analysis of the kinetics and energetics. *Biophysical Journal*, **88**(2):1364, 2005.

[163] M. de Frutos, S. Brasiles, P. Tavares, and E. Raspaud. Effect of spermine and DNase on DNA release from bacteriophage T5. *The European Physical Journal E: Soft Matter and Biological Physics*, **17**(4):429, 2005.

[164] D. Löf, K. Schillén, B. Jönsson, and A. Evilevitch. Forces Controlling the Rate of DNA Ejection from Phage λ. *Journal of Molecular Biology*, **368**(1):55, 2007.

[165] D. Löf, K. Schillén, B. Jönsson, and A. Evilevitch. Dynamic and static light scattering analysis of DNA ejection from the phage λ. *Physical Review E*, **76**(1):11914, 2007.

[166] E. Raspaud, T. Forth, C. São-José, P. Tavares, and M. De Frutos. A kinetic analysis of DNA ejection from tailed phages revealing the prerequisite activation energy. *Biophysical Journal*, **93**(11):3999, 2007.

[167] A. Evilevitch, L. Lavelle, C.M. Knobler, E. Raspaud, and W.M. Gelbart. Osmotic pressure inhibition of DNA ejection from phage. *Proceedings of the National Academy of Sciences*, **100**(16):9292, 2003.

[168] A. Evilevitch, J.W. Gober, M. Phillips, C.M. Knobler, and W.M. Gelbart. Measurements of DNA lengths remaining in a viral capsid after osmotically suppressed partial ejection. *Biophysical Journal*, **88**(1):751, 2005.

[169] M. Castelnovo and A. Evilevitch. DNA ejection from bacteriophage: Towards a general behavior for osmotic-suppression experiments. *The European Physical Journal E*, **24**(1):9, 2007.

[170] C. São-José, M. de Frutos, E. Raspaud, M.A. Santos, and P. Tavares. Pressure built by DNA packing inside virions: enough to drive DNA ejection in vitro, largely insufficient for delivery into the bacterial cytoplasm. *Journal of Molecular Biology*, **374**(2):346, 2007.

[171] J. Kindt, S. Tzlil, A. Ben-Shaul, and W.M. Gelbart. DNA packaging and ejection forces in bacteriophage. *Proceedings of the National Academy of Sciences*, **98**(24):13671, 2001.

[172] S. Tzlil, J.T. Kindt, W.M. Gelbart, and A. Ben-Shaul. Forces and pressures in DNA packaging and release from viral capsids. *Biophysical Journal*, **84**(3):1616, 2003.

[173] M.M. Inamdar, W.M. Gelbart, and R. Phillips. Dynamics of DNA ejection from bacteriophage. *Biophysical Journal*, **91**(2):411, 2006.

[174] I. Ali, D. Marenduzzo, and J.M. Yeomans. Polymer packaging and ejection in viral capsids: shape matters. *Physical Review Letters*, **96**(20):208102, 2006.

[175] I. Ali, D. Marenduzzo, and J.M. Yeomans. Ejection dynamics of polymeric chains from viral capsids: effect of solvent quality. *Biophysical Journal*, **94**(11):4159, 2008.

[176] C. Micheletti, D. Marenduzzo, E. Orlandini, and D.W. Sumners. Knotting of random ring polymers in confined spaces. *The Journal of Chemical Physics*, **124**:064903, 2006.

[177] J. Kochan, J.L. Carrascosa, and H. Murialdo. Bacteriophage lambda preconnectors: Purification and structure. *Journal of Molecular Biology*, **174**(3):433, 1984.

[178] D.J. Müller, A. Engel, J.L. Carrascosa, and M. Vélez. The bacteriophage $\phi 29$ head–tail connector imaged at high resolution with the atomic force microscope in buffer solution. *The EMBO Journal*, **16**(10):2547–2553, 1997.

[179] M.E. Cerritelli, N. Cheng, A.H. Rosenberg, C.E. McPherson, F.P. Booy, and A.C. Steven. Encapsidated conformation of bacteriophage T7 DNA. *Cell*, **91**(2):271, 1997.

[180] N.V. Hud and K.H. Downing. Cryoelectron microscopy of λ phage DNA condensates in vitreous ice: The fine structure of DNA toroids. *Proceedings of the National Academy of Sciences*, **98**(26):14925, 2001.

[181] I. Ali, D. Marenduzzo, and J.M. Yeomans. Dynamics of polymer packaging. *The Journal of Chemical Physics*, **121**:8635, 2004.

[182] C. Dekker. Solid-state nanopores. *Nature Nanotechnology*, **2**(4):209, 2007.

[183] D.E. Smith, S.J. Tans, S.B. Smith, S. Grimes, D.L. Anderson, and C. Bustamante. The bacteriophage $\phi 29$ portal motor can package DNA against a large internal force. *Nature*, **413**(6857):748, 2001.

[184] D. Marenduzzo, E. Orlandini, A. Stasiak, D.W. Sumners, L. Tubiana, and C. Micheletti. DNA–DNA interactions in bacteriophage capsids are responsible for the observed DNA knotting. *Proceedings of the National Academy of Sciences*, **106**(52):22269, 2009.

[185] Y. Adachi, E. Käs, and U.K. Laemmli. Preferential, cooperative binding of DNA topoisomerase II to scaffold-associated regions. *The EMBO Journal*, **8**(13):3997, 1989.

[186] S.V. Razin, Y.S. Vassetzky, and R. Hancock. Nuclear matrix attachment regions and topoisomerase II binding and reaction sites in the vicinity of a chicken DNA replication origin. *Biochemical and Biophysical Research Communications*, **177**(1):265, 1991.

[187] G. Masliah, B. René, L. Zargarian, S. Fermandjian, and O. Mauffret. Identification of intrinsic dynamics in a DNA sequence preferentially cleaved by topoisomerase II enzyme. *Journal of Molecular Biology*, **381**(3):692, 2008.

[188] M. Hogan, J. Legrange, and B. Austin. Dependence of DNA helix flexibility on base composition. *Nature*, **304**:752, 1983.

[189] T.M. Okonogi, S.C. Alley, A.W. Reese, P.B. Hopkins, and B.H. Robinson. Sequence-dependent dynamics of duplex DNA: The applicability of a dinucleotide model. *Biophysical Journal*, **83**(6):3446, 2002.

[190] A. Scipioni, C. Anselmi, G. Zuccheri, B. Samori, and P. De Santis. Sequence-dependent DNA curvature and flexibility from scanning force microscopy images. *Biophysical Journal*, **83**(5):2408, 2002.

[191] J. Ramstein and R. Lavery. Energetic coupling between DNA bending and base pair opening. *Proceedings of the National Academy of Sciences*, **85**(19):7231, 1988.

[192] P.G. de Gennes. *Scaling Concepts in Polymer Physics*. Cornell University Press, New York, 1979.

[193] T. Schilling and F. Schmid. Computing absolute free energies of disordered structures by molecular simulation. *The Journal of Chemical Physics*, **131**:231102, 2009.

[194] J.A. Aronovitz and D.R. Nelson. Universal features of polymer shapes. *Journal de Physique*, **47**(9):1445, 1986.

[195] J.W. Cannon, J.A. Aronovitz, and P. Goldbart. Equilibrium distribution of shapes for linear and star macromolecules. *Journal de Physique I*, **1**(5):629, 1991.

[196] K. Alim and E. Frey. Shapes of semiflexible polymer rings. *Physical Review Letters*, **99**(19):198102, 2007.

[197] J.P. Wittmer, H. Meyer, J. Baschnagel, A. Johner, S. Obukhov, L. Mattioni, M. Müller, and A.N. Semenov. Long range bond-bond correlations in dense polymer solutions. *Physical Review Letters*, **93**(14):147801, 2004.

[198] L. Schäfer, A. Ostendorf, and J. Hager. Scaling of the correlations among segment directions of a self-repelling polymer chain. *Journal of Physics A: Mathematical and General*, **32**:7875, 1999.

[199] J.D. Moroz and P. Nelson. Torsional directed walks, entropic elasticity, and DNA twist stiffness. *Proceedings of the National Academy of Sciences*, **94**(26):14418, 1997.

[200] R.D. Kamien. The geometry of soft materials: a primer. *Reviews of Modern Physics*, **74**(4):953, 2002.

[201] S. Medalion, S.M. Rappaport, and Y. Rabin. Coupling of twist and writhe in short DNA loops. *The Journal of Chemical Physics*, **132**:045101, 2010.

[202] T. Sakaue and E. Raphael. Polymer Chains in Confined Spaces and Flow-Injection Problems: Some Remarks. *Macromolecules*, **39**:2621, 2006.

[203] J. Happel and H. Brenner. *Low Reynolds Number Hydrodynamics: with Special Applications to Particulate Media*. Martinus Nijhoff Publishers, The Hague, 1991.

[204] J.G. Kirkwood and J. Riseman. The intrinsic viscosities and diffusion constants of flexible macromolecules in solution. *The Journal of Chemical Physics*, **16**:565, 1948.

[205] P.G. de Gennes. Reptation of a Polymer Chain in the Presence of Fixed Obstacles. *The Journal of Chemical Physics*, **55**:572, 1971.

[206] B. Ewing and K.C. Millett. A load balanced algorithm for the calculation of the polynomial knot and link invariants. In *The Mathematical Heritage of C.F. Gauss*, page 225. World Scientific, Singapore, 1991.

[207] V. Katritch, W.K. Olson, A. Vologodskii, J. Dubochet, and A. Stasiak. Tightness of random knotting. *Physical Review E*, **61**(5):5545, 2000.

[208] I.A. Dynnikov. Recognition algorithms in knot theory. *Russian Mathematical Surveys*, **58**(6):1093, 2003.

Appendix A

Background – Polymers and Filaments

In this appendix, we present some key concepts and models that are referred to in various chapters. We focus on polymers since they are the main topic of this thesis. For filaments, in the non-Brownian regime, concepts such as bending stiffness (section A.1.3), linking number (section A.1.4), and hydrodynamic interactions (section A.2.2) still apply. Without fluctuations, however, models to describe thermally-averaged quantities like the (average) radius of gyration (section A.1.1), the persistence length (section A.1.3), thermal relaxation and diffusion (sections A.2.1 and A.2.3), and concepts based on entropy like the blob picture (section A.1.5) are no longer relevant.

We begin by discussing some static properties before moving to dynamics.

A.1 Statics

Polymers are of sufficiently small size that thermal effects must be taken into account when describing them. In this section, we introduce some static properties. Their values are typically averaged over the different configurations explored due to the

fluctuations.

A.1.1 Polymer Size

An important question is how the typical size of a polymer chain scales with the number of segments, N - the value of ν in $R \sim N^{\nu}$. The length, R, may be taken as the end-to-end distance or the *radius of gyration*,

$$R_g^2 = \frac{1}{N} \sum \left\langle (\mathbf{r_i} - \mathbf{r_{cm}})^2 \right\rangle , \tag{A.1}$$

where $\mathbf{r_i}$ is the position of the ith monomer and $\mathbf{r_{cm}}$ is the position of the centre of mass. The brackets indicate a thermal average. R_g, unlike end-to-end distance, is also applicable to ring polymers.

Perhaps the simplest model of a (flexible) polymer is the freely jointed chain [1]. The polymer is represented as a set of N vectors of a certain length joined such that the end of the i^{th} vector coincides with the start of the $i + 1^{th}$. The direction of each vector is independent of all others. Such a chain, with no interactions between monomers that are not close to each other along the contour (the curve formed by moving from monomer to monomer along bonds), is often called ideal. It is a random walk and the typical size (length) of the chain scales as, $R \sim N^{\frac{1}{2}}$.

In real polymers, there are interactions between monomers that are separated along the contour, particularly when they become spatially close. At least at short range, they will be repulsive and this effect is known as *excluded volume*. The value of ν is affected by the strength of the interactions between the different polymer segments compared to the temperature. These interactions typically depend on the ions in the solvent in which the polymer is immersed – higher concentrations or valencies, or lower temperatures, make the solvent poorer: the behaviour may be split into three regimes called *bad*, *theta*, and *good* solvent respectively.

In a bad solvent, there is an attraction between different monomers which dominates over entropy and the polymer collapses. Due to excluded volume, it may not collapse to an arbitrarily small size and its volume increases linearly with N, which gives $\nu = 1/3$ in three dimensions.

In a theta solvent, the attractions and entropy balance and the chain behaves as if it would have no excluded volume, like a random walk without self-avoidance. This gives $\nu = 1/2$ in three dimensions.

Flory proposed a simple mean field approach to estimating ν in a good solvent, where entropy dominates and the effective interactions are repulsive. By finding the minimum of a free energy composed of a repulsion term, estimated by assuming that all monomers interact with each other, and an entropic term, taken as the elastic energy for an ideal chain, the exponent in d dimensions is determined as

$$\nu = \frac{3}{d+2}. \tag{A.2}$$

For $d = 2$ and $d = 3$ this turns out to be very accurate although this is probably due to a fortuitous cancellation of errors [192].

A.1.2 Polymer Shape

The ensemble-averaged shape of a polymer not subject to an external potential will be spherically symmetric. However, the same is not generally true of a single polymer configuration. In fact, it is found that the typical instantaneous shape of a polymer is rather anisotropic.

This interesting feature was characterised using two measures, Δ and $\mathcal{S}$, by Aronovitz and Nelson [194]. The calculation begins with a generalisation of the (instantaneous) radius of gyration for a continuous random walk (a simple polymer

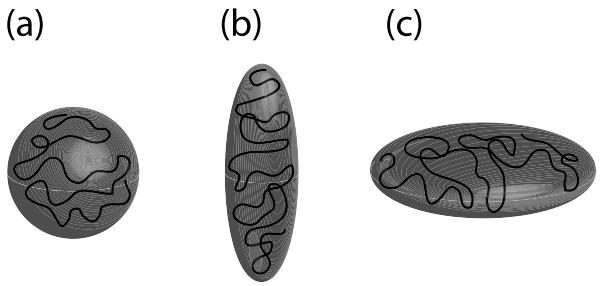


Figure A.1: Illustrations of polymer configurations with different types of shapes. The black lines represent the polymers and the grey objects emphasise their 'smoothed-out' forms. (a) Spherical. (b) Aspherical, prolate. (c) Aspherical, oblate.

model, see section A.1.1), $\mathbf{r}(s)$, where $0 \leq s \leq S$, to a 3×3 tensor defined as,

$$Q_{ij} = \frac{1}{S}\int_0^S ds\, r_i r_j - \frac{1}{S^2}\int_0^S ds\, r_i \int_0^S ds\, r_j. \tag{A.3}$$

The eigenvalues, λ_i, of $\mathbf{Q}$ are the squares of the extension of the polymer along its principal axes. The definitions of Δ and $\mathcal{S}$ are then as follows:

$\Delta = \frac{3}{2}\langle \mathrm{tr}\,\hat{\mathbf{Q}}^2\rangle / \langle (\mathrm{tr}\,\mathbf{Q})^2\rangle$ $(0 \leq \Delta \leq 1)$ shows the *degree* of asphericity with $\Delta = 0$ indicating spherical symmetry: for a spherically symmetric object $\lambda_1 = \lambda_2 = \lambda_3$ so their variance, $\mathrm{tr}\,\hat{\mathbf{Q}}^2$, will be zero ($\hat{\mathbf{Q}}$ is a traceless version of $\mathbf{Q}$.)

$\mathcal{S} = 27\langle \det \hat{\mathbf{Q}}\rangle / \langle (\mathrm{tr}\,\mathbf{Q})^3\rangle$ $(-\frac{1}{4} \leq \mathcal{S} \leq 2)$ indicates the *nature* of the asphericity: $\mathcal{S} = -\frac{1}{4}$ implies an oblate shape and $\mathcal{S} = 2$ a prolate shape. These different kinds of shapes are depicted in Fig. A.1. The numerator, $\det \hat{\mathbf{Q}} = (\lambda_1 - \bar{\lambda})(\lambda_2 - \bar{\lambda})(\lambda_3 - \bar{\lambda})$, where $\bar{\lambda}$ is the average eigenvalue of $\mathbf{Q}$. If the configuration is oblate, then two eigenvalues will be larger than $\bar{\lambda}$ and one less and $\det \hat{\mathbf{Q}}$ will be negative. For a prolate configuration, on the other hand, only one eigenvalue will be greater and $\det \hat{\mathbf{Q}}$ will thus be positive.

In their original paper, using Δ and $\mathcal{S}$, Aronovitz and Nelson [194] found that both random walks (a model of a polymer in a theta solvent, see section A.1.1) and self-avoiding random walks (a model of a polymer in a good solvent, see section A.1.1)

are aspherical and prolate.

Δ and $\mathcal{S}$ were chosen partially for computational ease; using analytical method of ref. [194] the ratios of averages are much easier to calculate than the averages of ratios. As discussed in a later paper [195], Δ and $\mathcal{S}$ suffer from the problem that larger configurations have higher weighting. For numerical work, better measures are the averages of $\Delta_0 = \frac{3}{2}\mathrm{tr}\,\hat{\mathbf{Q}}^2/(\mathrm{tr}\,\mathbf{Q})^2$ and $\Sigma_0 = 4\det\hat{\mathbf{Q}}/(\frac{2}{3}\mathrm{tr}\,\hat{\mathbf{Q}}^2)^{\frac{3}{2}}$ – which obey the inequalities $0 \leq \Delta_0 \leq 1$ and $-1 \leq \Sigma_0 \leq 1$. Σ_0 has the added advantage that, unlike $\mathcal{S}$, it is not sensitive to the extent of the asphericity, only its nature (prolateness/oblateness). These measures have been used in later work, such as in ref. [196], where the shapes of polymer rings as a function of their stiffness are considered.

A.1.3 Persistence Length

In models such as the freely jointed chain described in section A.1.1, the orientations of consecutive bonds are independent. For real polymers, this is often not the case: the chains have a finite bending stiffness such that there is an energetic penalty for neighbouring sections not being aligned. Such chains are generally called *semi-flexible*. A simple model, the Kratky-Porod model [1], captures this by describing a polymer as a continuous contour with a local bending energy that is quadratic in the rate of change of the unit tangent vector, $\mathbf{u}(s)$, where s is displacement along the chain. By solving this model it is found that the bond correlation function, $\langle \mathbf{u}(s)\cdot\mathbf{u}(0)\rangle = e^{-s/l_p}$, where l_p is known as the *persistence length*. This form of the bond correlation function is more generally applicable to models with bending stiffness. If such chains are sufficiently long then they may be described as flexible, with segments of size $\sim l_p$.

Although the Kratky-Porod model ignores excluded volume, it was previously believed that an exponential decay will always be seen due to screening of the excluded volume effect [197]. It has been realised relatively recently, however, that in fact

excluded volume leads to long-range interactions that result in a power-law decay of the bond correlation function in the scaling limit, $\langle \mathbf{u}(s) \cdot \mathbf{u}(0) \rangle \sim s^{-(2-2\nu)} \mathcal{F}$ [198, 197], where $\mathcal{F}$ is a scaling function that depends on the position along the contour. A value for the persistence length may be found by considering sufficiently short chains for which the exponential form does apply.

A.1.4 Linking Number

Some polymers, for example DNA, have the property of torsional stiffness as well as bending stiffness. To specify the configuration of such objects one must give not only the contour but also the twist around it [199].

Mathematically, these polymers may be represented by two vectors, $\mathbf{r}(s)$ and $\mathbf{p}(s)$, where s is a parameter, $\mathbf{r}(s)$ is a non-self-intersecting space curve and $\mathbf{p}(s)$ are unit vectors, perpendicular to $\mathbf{r}(s)$ pointing to chosen reference points on the polymer [4]. If $\omega(s)$ is the rate at which $\mathbf{p}(s)$ rotates around $\mathbf{r}(s)$ then the *twist*, Tw, is given by

$$Tw = \frac{1}{2\pi} \int \omega(s) ds. \tag{A.4}$$

Modelling of polymers with torsional stiffness is typically achieved by including an energy term that is locally proportional to $\omega(s)^2$.

The *writhe*, Wr, is a property that depends only on $\mathbf{r}(s)$. In rough terms, it measures how much the contour curves around itself in space. It is given by [200]:

$$Wr = \frac{1}{4\pi} \int ds \int ds' \, \mathbf{u}(s) \times \mathbf{u}(s') \cdot \frac{\mathbf{r}(s) - \mathbf{r}(s')}{|\mathbf{r}(s) - \mathbf{r}(s')|^3}, \tag{A.5}$$

where $\mathbf{u}(s)$ are unit tangent vectors to $\mathbf{r}(s)$. Useful descriptions of four different methods for calculating the writhe for curves consisting of straight sections, as are typically used in polymer simulations, are given in ref. [155].

For a closed curve, $\mathbf{r}(s)$ must be a periodic function of s, as must $\mathbf{p}(s)$. In this

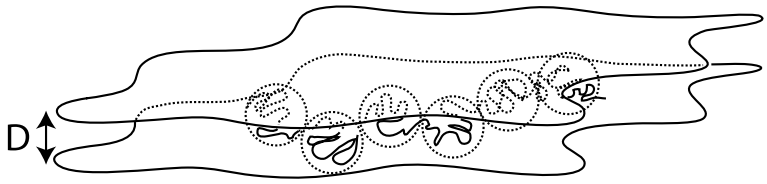


Figure A.2: A polymer confined within a slit – there are two parallel walls of infinite extent which confine it in the 'vertical' direction but it is free in the other two. The polymer may be pictured as forming a two-dimensional self-avoiding random walk of blobs whose size is determined by the slit width, D.

case the sum of the twist and the writhe is an integer and a topological invariant known as the *linking number* [4]:

$$Lk = Tw + Wr. \tag{A.6}$$

The importance of linking number is shown by experiments with DNA. For example, the typical extension of DNA as a function of applied force depends on Lk [199]. Simulation work suggests that for short DNA rings, the coupling between twist and writhe introduced by the closure constraints changes the distribution of writhes from that which would be expected for a ring with only bending stiffness [201].

A.1.5 Blob Picture

For confined polymers, the scaling of quantities such as the average end-to-end distance may be found using simple arguments based on the idea of *blobs* [192]. For example, consider the situation of a polymer confined within a slit, as depicted in Fig. A.2. The polymer forms a self-avoiding random walk of blobs of size D, the slit width. Within each blob, the effect of confinement is negligible and the chain behaves as if free. So the number of monomers in each blob, $g \sim D^{1/\nu}$. The free energy

(entropic) penalty for confining the polymer will scale with the number of blobs thus,

$$F_{conf} \sim k_B T \frac{N}{D^{1/\nu}}, \tag{A.7}$$

where N is the number of monomers in the chain. This and other such scaling relations are valid in the limit $R \gg D$, where R is the size of the unconfined chain. They have been verified by Monte-Carlo simulations [77].

A similar argument may be applied to other confinement geometries. For a polymer in a tube (two-dimensional confinement) the same scaling of the free energy is found [192]. For three-dimensional confinement, for example in a sphere, there are different results [202] since there is no free dimension in which the chain may expand: the exponents for N and $1/D$ are larger.

The blob picture may also be used for polymers under tension [192]. In this case, the tension sets the blob length $\sim k_B T/\tau$, τ being the applied force.

A.2 Dynamics

Thermal fluctuations cause polymers to perform Brownian motion. In this section, we introduce some concepts used to understand this dynamics. The fluctuations generally arise from the fluid in which the polymer is immersed. This solvent produces a local drag force on monomers and, crucially for dynamical properties (but not for statics), transfers momentum between those that are spatially separated (*hydrodynamic interactions*.)

The simplest model to describe the dynamics of a polymer undergoing Brownian motion, the Rouse model, neglects hydrodynamic interactions between monomers. Some of its predictions are described briefly in section A.2.1. In section A.2.2, the equations to describe a solvent and their application to polymers is discussed. In section A.2.3, some of the predictions of the Zimm model of polymers, which does in-

clude hydrodynamic interactions between monomers, are given. Finally, section A.2.4 describes a model that applies to the diffusive dynamics of entangled polymers.

A.2.1 Rouse Model

The simplest approach to modelling polymers is to only consider the effects of thermal fluctuations and local drag due to the solvent and ignore hydrodynamic interactions between monomers. Such models show general features that correspond to a model due to Rouse [1].

In the Rouse model, excluded volume and hydrodynamic interactions are neglected and the polymer is modelled as a chain of beads connected by harmonic springs. The beads are subject to a local drag force and random forces. There are no correlations between the random forces acting on different beads or those that act on a particular bead at different times. After taking the continuous limit, it is found that the equation describing the chain may be rewritten in terms of independent normal modes. The time correlation functions of these have an exponential form allowing relaxation times to be extracted [1].

Many properties of the Rouse model may be calculated analytically. For example, the diffusion coefficient, $D \sim N^{-1}$, where N is the number of monomers in the chain and the longest relaxation time, $\tau_R \sim N^{1+2\nu}$. These predictions do not agree with experiments for polymers in dilute solution [1] and this is because hydrodynamics is neglected.

A.2.2 Hydrodynamic Interactions

The motion of the solvent may typically be described by the Navier-Stokes equation [203]:

$$\rho\left(\frac{\partial \mathbf{v}}{\partial t} + \mathbf{v}\cdot\nabla\mathbf{v}\right) = -\nabla p + \eta\nabla^2\mathbf{v} + \mathbf{F}, \tag{A.8}$$

where $\mathbf{v}$ is the local velocity of the fluid, p is pressure, ρ is density, η the shear viscosity (often referred to simply as viscosity) and $\mathbf{F}$ is a body force applied to the fluid. This form of the equation describes a homogenous, isothermal, Newtonian fluid that is incompressible ($\nabla \cdot \mathbf{v} = 0$).

To characterise the type of flow that will arise in a given problem, various dimensionless numbers may be introduced. Perhaps the most important of these is the *Reynolds number*,

$$Re = \frac{UL\rho}{\eta}, \tag{A.9}$$

where U is a typical velocity for the problem and L a typical length scale. It is a ratio of the typical inertial forces to the typical viscous forces. If the Reynolds number is small ($\lesssim 0.2$), then a reasonable approximation is to completely neglect the inertial forces. In this case Eq (A.8) reduces to:

$$\eta \nabla^2 \mathbf{v} = \nabla p - \mathbf{F}, \tag{A.10}$$

which, along with the continuity equation ($\nabla \cdot \mathbf{v} = 0$), comprises the Stokes or creeping motion equations. These have the huge advantage that they are, unlike the Navier-Stokes equation, linear.

According to these equations, the drag on a single sphere of radius a moving at steady velocity U through an unbounded fluid is

$$F = 6\pi\eta a U. \tag{A.11}$$

Typically, polymers and filaments are modelled as a chain of segments which are subject to forces, possibly external or possibly arising from intra-chain interactions. Motion of one segment due to a force will transfer momentum to the surrounding fluid which will propagate it to other segments. According to the Stokes equations,

this will occur instantaneously. If the Stokes equations are valid and the fluid is unbounded, then, at time t, a particular segment will move with a velocity which is entirely determined by the forces on it and on all other segments, as well as their relative positions, all determined at t. In this situation, the effect of hydrodynamic interactions may be represented by a *mobility tensor* which depends on the positions of all the segments.

The segments may be approximated as point particles. In this case the force in Eq (A.10) may be expressed as $\sum_i \mathbf{F_i}\delta(\mathbf{r}-\mathbf{r_i})$, where $\mathbf{F_i}$ is the force applied to the ith particle located at $\mathbf{r_i}$. Assuming the particles move with the fluid, the resulting equation may be solved using Fourier transforms [1] giving,

$$\mathbf{v}(\mathbf{r_i}) = \sum_j \mathbf{H}(\mathbf{r_i}-\mathbf{r_j})\cdot\mathbf{F_j}, \tag{A.12}$$

where $\mathbf{v}(\mathbf{r_i})$ is the velocity of the ith particle located at $\mathbf{r_i}$, $\mathbf{F_j}$ is the force applied to particle j and $\mathbf{H}(\mathbf{r})$ is the Oseen tensor:

$$\mathbf{H}(\mathbf{r}) = \frac{1}{8\pi\eta r}(\mathbf{I}+\hat{\mathbf{r}}\hat{\mathbf{r}}), \tag{A.13}$$

where $\hat{\mathbf{r}}$ is a unit vector in the direction of $\mathbf{r}$. According to this equation, the contribution to the velocity of a particle due to the force applied to itself will be infinite. A simple, commonly used, resolution is to define the Oseen tensor in this case to be $\mathbf{I}/\zeta$, where ζ is a drag constant. The Oseen approach was first applied to polymers by Kirkwood and Riseman [204].

The next simplest approximation is to consider the segments as spheres. As well as translating, spheres may rotate. Jeffrey and Onishi [86] found solutions for the problem of the interaction of two unequal spheres in an unbounded viscous fluid. They obtained expressions for a mobility tensor, which relates the forces and torques on both spheres to their resulting linear and angular velocities, in terms of power

series.

The approach using the Oseen tensor is equivalent to taking Jeffrey and Onishi's results for the case of equal spheres, ignoring rotation, and truncating the series after the first term (using $\zeta = 6\pi\eta a$, where a is the sphere radius). If the next term ($\sim r^{-3}$) in the series is included, still neglecting rotation, then the Rotne-Prager mobility tensor is found [85]. In their original derivation, Rotne and Prager found this tensor by considering the minimisation of the rate at which energy is dissipated by fluid motion. They also extended the mobility tensor to the case that spheres overlap in such a way that it is positive definite for all configurations.

Treatments of the hydrodynamics of multiple spheres with the Oseen and Rotne-Prager mobility tensors only include two-body interactions, neglecting many-body terms. Actually, since according to the Stokes equations propagation is instantaneous, momentum will be reflected an infinite number of times between all the different spheres. So the response of sphere i to a force on sphere j will depend on the positions of *all* the spheres in the system, not just i and j, as in the two-body approximation.

More sophisticated approaches using mobility tensors may include sphere rotation, higher-order terms and multi-body terms [152].

A.2.3 Zimm Model

The Zimm model is similar to the Rouse model but instead of beads being subject only to local drag forces, hydrodynamics interactions are included using the Oseen tensor [1]. For modelling polymers in a good solvent, excluded volume interactions may also be included with a potential that penalises self intersections of the chain. Both of these additions result in a non-linear equations. A linear equation of the same form as the Rouse model is regained by approximating the interactions as pre-averaged over equilibrium distributions and then neglecting off-diagional terms in the tensor that is found [1].

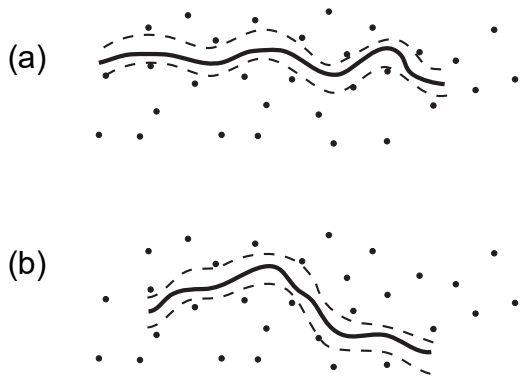


Figure A.3: (a) Solid line represents a polymer lying within obstacles, which are shown by dots. The obstacles are pictured as forming a reptation tube, depicted with dashed lines. (b) The ends of the polymer are able to explore regions outside the initial tube. In this way the tube will change.

In the Zimm model, the diffusion coefficient, $D \sim N^{-\nu}$, where N is the number of monomers in the chain, and the longest relaxation time, $\tau_r \sim N^{3\nu}$. These values are in much better agreement with experimental observations than the Rouse model [1].

A.2.4 Reptation

Reptation is a term that was coined by de Gennes [205] to describe the motion of polymer in between fixed obstacles, as depicted in Fig. A.3. In the original work the obstacles correspond to a gel but it is also relevant to situations where polymers are highly entangled such as melts [1].

The polymer is taken to be much longer than the typical separation of the obstacles, which it is not able to cross. The obstacles are pictured as forming a relatively thin reptation tube as shown in Fig. A.3. The polymer may move relatively freely along the contour of this tube but not perpendicular to it.

Two different time-scales are identified. In the notation of Doi and Edwards [1], the first time-scale, τ_R, is associated with the relaxation of the polymer within the initial tube. For a finite length polymer, the reptation tube does not remain unchanged indefinitely. At longer times, the ends of the polymer are able to move out of the

initial tube and explore new regions. The second time scale, τ_d is associated with the renewal of the reptation tube.

The mean squared displacement of a polymer segment increases with time with different exponents in the different regimes. For time $t \lesssim \tau_R$, the motion is sub-diffusive, with an exponent of $\frac{1}{4}$. Between τ_R and τ_d, the motion *along the tube contour* is diffusive which results in sub-diffusive motion in three-dimensional space, with an exponent of $\frac{1}{2}$. At long times, greater than τ_d, diffusive motion is seen in three-dimensional space.

Appendix B

Knot Methods

When simulating knotted polymers and filaments it is important to be able to calculate a knot invariant to verify the type of knot present. Due to its relative ease of calculation, the Alexander polynomial, $A_K(t)$, at specific values of t, is a common choice [65]. More sophisticated methods, based on the skein relations discussed in section 2.1.4, may be used to calculate more general knot polynomials [206]. For example, the *standard ascender algorithm* reduces a knot diagram recursively by using the skein relations to convert knots towards the *standard ascending position* in which, starting from an arbitrary point, the contour always passes *over* earlier points on the contour at crossings. Such algorithms, however, require a computation time that is an exponential function of the number of crossings of the original diagram, since each crossing change creates two new diagrams [206]. In order to make such algorithms practicable, rather involved methods to choose judicious crossing changes are necessary.

In some simulations, it is necessary to locate a knot, to determine which section of a polymer or filament it is in. This is not generally a simple task. Consider a ring polymer. Any section of the polymer that is not the whole will be open and so technically unknotted. One approach, first used by Katritch *et al.* [207], is to take

sections and convert them into closed rings by adding a additional piece joining the two end points. The smallest section having the correct value for some knot invariant is then identified as containing the knot. One problem is that the closure procedure may introduce additional crossings that change the topology of a section.

In the remainder of this appendix, we describe the methods that we use to verify knot type and locate knots. They are based on those described above. We also describe our approach to creating knotted configurations.

B.1 Checking Knot Type

To check knot type, we calculate the Alexander polynomial, $A_K(t)$, at $t = -1$ and $t = -2$. Whilst this cannot distinguish all knots, it can discriminate between all prime knots with up to 8 essential crossings. Our method of calculation is the matrix approach described in section 2.1.4.

A projection of the knot is taken and all crossings are found. It may be necessary to rotate the knot to avoid, for example, more than two parts projecting to the same point. The knot diagram is numbered such that arc i ends at crossing i. For each arc, the following information is recorded: the handedness of the corresponding crossing; the distance along the contour, from an arbitrary starting point, of the upper and lower parts of the crossing. Using this information, the numbers of the over-crossing arcs are determined.

In principle, the matrix could be constructed, and the Alexander polynomial for the required value of t calculated, immediately. To reduce the time required to compute the matrix determinant, the knot diagram, as encoded in the information about the arcs, is first simplified. A description of how this is achieved is given in section B.2.

This approach is, in practice, sufficient for our purpose and so, for simplicity, more sophisticated methods [206] are not considered.

B.2 Diagram Simplification

In this section, we discuss how the knot diagram is simplified before the Alexander polynomial is calculated to improve efficiency. Simplification is performed by removing and changing crossings using Reidemeister moves. All three types of Reidemeister moves are used but type I and type II moves are only made in the direction which removes crossings. Moves are made until either a limit on their number is reached or the number of crossings remaining is less than a specified minimum.

This approach will not succeed in simplifying all diagrams. For example, there are diagrams of the unknot that may not be simplified unless moves which first increase the number of crossings are made [208]. To ensure reasonable running times, the determinant is only calculated for diagrams with a number of crossings below a chosen upper bound. For a given choice, there are diagrams for which the Alexander polynomial cannot be found. For the simulations here, these are found to occur sufficiently rarely that the algorithm is useful.

Identification of potential moves is achieved by checking if certain conditions on the arcs are fulfilled. For example, if $o(i)$ is the number of the upper arc at the crossing at which arc i ends then if $i = o(i)$ a type I move may be made.

To elucidate the process further, the identification of type III moves is discussed in a little more detail. In a type III move, a strand is shifted from one side of a crossing to the other as described in section 2.1.1. For a right-handed crossing, there are eight different initial diagrams. These may be grouped into four pairs according to the condition that is used to identify them, as shown in Fig. B.1. The same conditions are valid for left-handed crossings. Further checks must be made to ensure there are no additional strands which may block the move. When the move is made, appropriate new positions on the arcs for the crossings must be found and it must be verified if the handedness of crossings should change, so that the correct Alexander polynomial will be found.

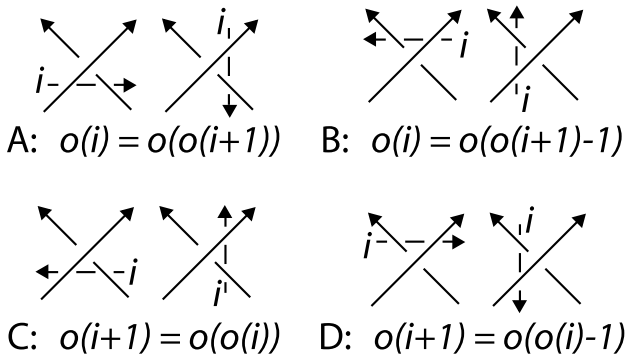


Figure B.1: Initial diagrams on which a type III move may be performed. In the move the strand that passes under both other strands is moved to the opposite side of the crossing it is not involved in. The pairs labelled A-D may be identified by different conditions, shown below the diagrams.

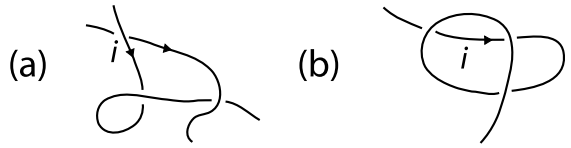


Figure B.2: (a) An example of a diagram which would be falsely identified as having a potential type III move using condition C in Fig. B.1 because a type I move has not been made. (b) False identification of type III by condition B or D in Fig. B.1 because a type II move has not been made.

Whilst the conditions in Fig. B.1 will identify all potential type III moves, they may also produce false positives. These may occur when crossings that could be removed through type I or type II moves are still present. Fig. B.2 depicts two diagrams for which false positives would occur in this way. To avoid such errors, all possible type I and II moves are made before identifying all potential type III moves. A randomly picked type III move is made, before again performing all possible type I and II moves.

Care must be taken to deal correctly with diagrams such as those shown in Fig. B.3(a) and Fig. B.3(b). For diagrams such as these, type III moves are, in principle, possible (technically they would have to be made as a series of moves including type I and type II moves as well). However, the changing of crossing handedness is

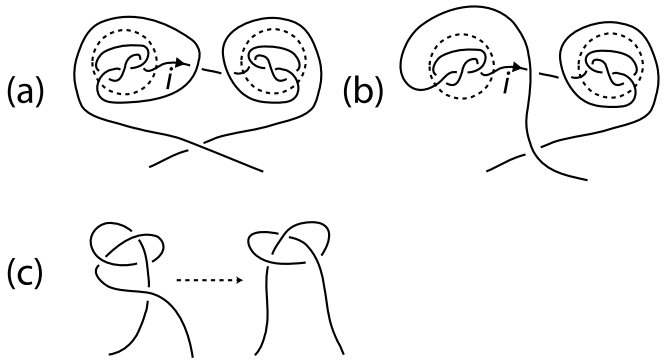


Figure B.3: (a) An example of a diagram which would indicate a possible type III move using condition A in Fig. B.1. The changes of handedness required are different to those that would be expected for a 'standard' type III move. (b) Another example. In both (a) and (b) if the crossings in the circled sections were removed then performing type I moves first would avoid such diagrams. They could also be avoided by allowing moves like that shown in (c).

different to that for 'standard' type III moves like those depicted in Fig. B.1. Diagrams like Fig. B.3(a) can be distinguished by testing whether the handedness of two of the crossings is the same and those like Fig. B.3(b) by testing the order in which different arcs are crossed. Diagrams like these could be avoided by allowing moves such as that shown in Fig. B.3(c).

The procedure outlined was tested on diagrams with known topology to check that it preserves knot type.

B.3 Knot Locating

To locate knots within a polymer, we use an approach that considers sections and calculates a knot invariant for them, similar to that first introduced by Katritch *et al*. [207]. However, instead of closing sections, we choose a particular, arbitrary projection of the polymer. We find all crossings in the projection. By rotating lines starting from the vertices on either side of both the upper and lower strands at each crossing, we determine which sections may be closed without introducing

any additional crossings. We then calculate the Alexander polynomial, generally at $t = -2$, for each of these sections. We identify the smallest section with the correct value as containing the knot. The method is depicted in Fig. B.4. It has the advantage that, unlike previous methods, no additional crossings are added that might change the topology of a section. A disadvantage is that the result for a particular configuration will depend on the projection chosen. We checked the algorithm by visually inspecting the configurations of sections identified as containing a given knot.

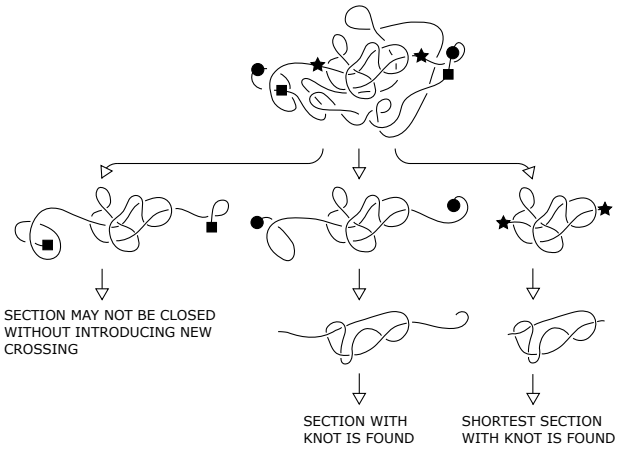


Figure B.4: Diagram representing the knot-finding algorithm. In the first step crossings in the knot diagram found by taking a projection of the polymer in a plane are identified. Pairs of points, each member of which is adjacent to a crossing, are found. All such pairs are considered. It is checked that a given section may be closed without introducing new crossings. If it may the Alexander polynomial, generally at $t = -2$, is calculated. The shortest section with the correct Alexander polynomial is identified as containing the knot.

Although the approach described does not add additional crossings it may still incorrectly identify a section as containing a certain knot. As depicted in Fig. B.5, in principle, a configuration of an unknotted ring may be found such that any knot would be identified in a subsection of it. This is an unavoidable problem for any method that attempts to locate a knot by considering subsections of a ring. For thermal systems, constricted configurations such as that depicted in Fig. B.5 will be entropically unfavourable, however, and so unlikely to occur.

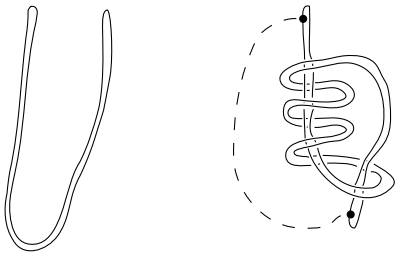


Figure B.5: In principle any knot type may be spuriously found in an unknotted polymer by algorithms that consider sections of it. If an unknotted polymer is taken and doubled up as on the left then it may be used to tie a knot as on the right. The knot could then be identified in the unknotted polymer by taking a section such as that indicated by the circles and closing it.

B.4 Creation of Knot Configurations

In order to ease initialisation of knotted configurations, we created a database of compact knots. The number of beads and length of each was recorded so they could be inserted into the co-ordinates describing a simulated polymer or filament.

Using a table of prime knots as a reference [34], relatively loose configurations, like that shown in Fig. B.6(a), can be quickly created by specifying the lengths and directions of the straight sections. These were then inserted into a linear polymer simulated using a model with FENE springs, Eq. (3.2), and evolved for $10^4 t_0$ with a force of $15 k_B T/\sigma$ applied to the end beads to provide tension and tighten the knot. The compact knot configuration was extracted using the knot-finding algorithm described in section B.3. An example of such a configuration is given in Fig. B.6(b).

Configurations for all knots with up to and including 8 essential crossings were created in addition to some more complex knots.



(a) (b)

Figure B.6: Configurations for the 8_{19} knot. (a) Initial configuration input by hand. (b) Tightened configuration.